# Low Cost Zinc Oxide Films for High Performance Rigid and Flexible Optoelectronic Devices

by

Mourad Benlamri

A thesis submitted in partial fulfillment of the requirements for the degree of

Doctor of Philosophy

in

Microsystems and Nanodevices

Department of Electrical and Computer Engineering
University of Alberta

# Abstract

From the fabrication perspective, zinc oxide (ZnO) offers the possibility of thin film growth through the use of low-cost solution techniques. The solution-processed ZnO films, usually of polycrystalline formation, are suitable for use in field-effect transistors and in such applications as electronic displays, transparent conductive electrodes, light-emitting diodes, radio frequency identification tags, and power inverters. Chemical bath deposition, spray pyrolysis, and sol-gel are some of the most commonly used solution techniques to synthesize ZnO thin films. Another solution technique, rarely utilized for optoelectronic devices fabrication, is the electrodeposition technique. My works utilized the sol-gel and electrodeposition techniques to grow high-quality ZnO thin films that provide the required electrical properties to produce highly performant optoelectronic devices in general and high-power devices in particular.

I present a fundamental study of the growth, and hence the resulting electrical properties, of ZnO films formed by the sol-gel process on two different high-quality substrates: silicon nitride ($Si_3N_4$) and silicon oxide ($SiO_2$). A high effective electron mobility of 33 $cm^2V^{-1}s^{-1}$ was achieved in the undoped ZnO thin films grown on $Si_3N_4$. The introduction of $Si_3N_4$ as growth substrate thus resulted in a mobility improvement by a factor of 2.5 with respect to the commonly used $SiO_2$. The ZnO films grown on $Si_3N_4$, prepared by low-pressure chemical vapor deposition, revealed bigger grain sizes and better crystalline quality in comparison to the films grown on thermal $SiO_2$. These results show that the nucleation and growth mechanisms of sol-gel films are substrate dependent.

Interface trap densities measured in high-κ hafnium oxide ($HfO_2$)/ZnO MOSCAPs were about ten times lower in those fabricated on $Si_3N_4$ substrates.

Although the sol-gel ZnO films have achieved a relatively high electron mobility, they still suffer from high, uncontrollable doping densities in the general range of $10^{17}$-$10^{20}$ $cm^{-3}$. I present low-doped and highly textured ZnO films, synthesized by an optimized low-cost and low-temperature electrodeposition technique on copper substrates, which possess an equilibrium free electron concentration of ~$2.8 \times 10^{14}$ $cm^{-3}$ and a minimum electron mobility as high as 80 $cm^2V^{-1}s^{-1}$. These electrical parameters tend toward those obtained in hydrothermally-grown single crystals of bulk ZnO. The resulting Schottky diodes made, for the first time to our best knowledge, by electrodeposited ZnO on copper films, demonstrate rectification ratios of ~$10^6$, low on-state resistance, and ideality factors as low as 2. These results show a route forward for the growth of solution-processed ZnO of high electronic quality.

A flexible Kapton substrate was employed to grow a high-quality ZnO thin film optimized for optoelectronic performance by the electrodeposition technique, which allows process temperatures of less than 100 °C. Schottky diodes made of the electrodeposited ZnO film and underlying copper contact on flexible Kapton substrate exhibited high rectification ratios (~$10^6$) and low ideality factors (~2 to 3) that surpass the current state-of-the-art for reported solution-processed ZnO films. The diodes withstood reverse voltages in excess of -3 V with no breakdown. By performing bending tests, we

demonstrated that the diodes have potential capabilities to retain device operationality under mechanical deformations.

Because of the capabilities that the electrodeposition process provides in terms of moderate doping and high film thicknesses, its suitability for fabrication of power devices was explored by investigating its electrical breakdown strength. To our knowledge, this is the first investigation of breakdown field strength in electrodeposited ZnO material. Test vehicles in the form of Schottky diodes were made through a simple fabrication process with no passivation, no edge effect reduction and no dry etch. The devices exhibited high electrical performance with an ideality factor of 1.10, a carrier concentration of $2.5 \times 10^{15}$ $cm^{-3}$ and a critical electric field at breakdown of 800 kV $cm^{-1}$, which attest to the suitable quality of the ZnO film. The obtained value for the critical electric field surpasses the best reported value by one order of magnitude. Drastic changes in carrier concentration were observed for different growth conditions.

Planar microwave resonators employing ZnO films directly electrodeposited on copper strip lines were fabricated to study the photosensing capabilities and charge carrier lifetimes in these films as well as the effects of humidity on them. The film characterization parameters were extracted by analyzing the S-parameters of the resonator device in the microwave frequency region.

# Preface

This dissertation is submitted for the degree of Doctor of Philosophy at the University of Alberta. This Ph.D. thesis contains the result of research undertaken at the department of Electrical and Computer Engineering, University of Alberta, between September 2011 and August 2019, under the supervision of Professor Douglas W. Barlage and Professor Karthik Shankar. I am very grateful for the expert help and support of my supervisors and fellow students. The main contents of the dissertation are taken directly from previously published articles and articles being currently prepared or submitted for publication.

The main content presented in chapter 2 has been adapted from the published article [Benlamri, M., Bothe, K. M., Ma, A. M., Shoute, G., Afshar, A., Sharma, H., Mohammadpour, A., Gupta, M., Cadien, K. C., Tsui, Y. Y., Shankar, K., and Barlage, D. W., 2014, "High-mobility solution-processed zinc oxide thin films on silicon nitride," Physica Status Solidi-Rapid Research Letters, 8(10), pp. 871-875]. K. M. Bothe has assisted with the implementation of the mobility extraction model. This chapter is adapted with permission from © 2014 John Wiley and Sons.

The main content presented in chapter 3 has been adapted from the published article [Benlamri, M., Farsinezhad, S., Barlage, D. W., and Shankar, K., 2016, "Low residual donor concentration and enhanced charge transport in low-cost electrodeposited ZnO," Journal of Materials Chemistry C, 4(12), pp. 2279-2283]. S. Farsinezhad has assisted me

with the FESEM imaging. This chapter is adapted with permission from © 2016 The Royal Society of Chemistry.

The main content presented in chapter 4 has been adapted from the published article [Benlamri, M., Farsinezhad, S., Barlage, D. W., and Shankar, K., 2016, "Communication-High Performance Schottky Diodes on Flexible Substrates Using ZnO Electrodeposited on Cu," ECS Journal of Solid State Science and Technology, 5(6), pp. 324-326]. TEM technician Kai Cui at NRC-NINT took the TEM images and S. Farsinezhad assisted me with the FESEM imaging. This chapter is adapted with permission from © 2016 Electrochemical Society, Inc.

The main content presented in chapter 5 has been adapted from the published article [Benlamri, M., Wiltshire, B. D., Zhang, Y., Mahdi, N., Shankar, K., and Barlage, D. W., 2019, "High breakdown strength Schottky diodes made from electrodeposited ZnO for power electronics applications," ACS Applied Electronic Materials, 1(1), pp. 13-17]. B. D. Wilshire has performed some of the electron-beam evaporations and N. Mahdi assisted me with the XRD profiling. This chapter is adapted with permission from © 2019 American Chemical Society.

The content presented in chapter 6 is taken from a manuscript that is currently being submitted for publication. The microwave simulations and measurements have been performed by S. Deif and Dr. M. Zarifi. Dr M. Zarifi edited the initial text pertaining to the microwave part of the manuscript which I later re-edited and developed. N. Mahdi assisted me with the XRD profiling.

# Dedication

To Rebiha Benlamri and Mouloud Benlamri, my mother and father. Forever yours.

To my little daughters, the lights of my life, Dina, Sara, Aya, and Nada.

To my supporting wife Serine.

To those who I always carry in my heart, Ta Zohra, Rachid, my sisters and brothers.

# Acknowledgments

I am very grateful to all those who have supported me and helped me when I most needed it. My deepest gratitude goes to my supervisors Dr Douglas Barlage and Dr Karthik Shankar. I would also like to thank many of the professors at University of Alberta who have given me help whenever I have needed it. I will cherish all the memories I have nurtured with my fellow students who have enriched my life.

I thank the University of Alberta for this wonderful opportunity.

# Table of Contents

# List of Figures

# List of Tables

# List of Abbreviations

| | |
|---|---|
| **AFM** | Atomic force microscopy |
| **Ag** | Silver |
| **AgCl** | Silver chloride |
| **ALD** | Atomic layer deposition |
| **a-Si** | Amorphous silicon |
| **BFOM** | Baliga's figure of merit |
| **CMOS** | Complementary metal-oxide-semiconductor |
| **$CO_2$** | Carbon dioxide |
| **Cu** | Copper |
| **DC** | Direct current |
| **EMI** | Electromagnetic interference |
| **FESEM** | Field-emission scanning electron microscopy |
| **FWHM** | Full-width-at-half-maximum |
| **GaN** | Gallium nitride |
| **HfO2** | Hafnium oxide |
| **HFSS** | High-frequency structure simulator |
| **ITO** | Indium tin oxide |
| **JCPDS** | Joint Committee on Powder Diffraction Standards. |
| **LPCVD** | Low pressure chemical vapor deposition |
| **MEMS** | Microelectromechanical systems |
| **MFC** | Mass flow controller |

| | |
|---|---|
| **MilliQ** | Trademark created by Millipore Corporation to describe 'ultrapure' water |
| **MOSCAP** | Metal-oxide-semiconductor capacitor |
| **MOSFET** | Metal-oxide-semiconductor field-effect transistor |
| **MOV** | Metal-oxide varistor |
| **$NH_3$** | Ammonia |
| **$O_2$** | Molecular oxygen |
| **PCB** | Printed circuit board |
| **PDF** | Powder diffraction file |
| **pH** | Potential hydrogen |
| **PL** | Photoluminescence |
| **PPC** | Persistent photoconductivity |
| **Pt** | Platinum |
| **RFI** | Radio frequency interference |
| **RH** | Relative humidity |
| **R-Square** | Coefficient of determination |
| **SAW** | Surface acoustic wave |
| **SBH** | Schottky barrier height |
| **SHE** | Standard hydrogen electrode |
| **Si** | Silicon |
| **$Si_3N_4$** | Silicon nitride |
| **SiC** | Silicon carbide |
| **$SiH_2Cl_2$** | Dichlorosilane |
| **$SiO_2$** | Silicon dioxide |

| | |
|---|---|
| **SP** | Solution-processed |
| **TEM** | Transmission electron microscopy |
| **TFT** | Thin-film transistor |
| **Ti** | Titanium |
| **TiW** | Titanium tungsten |
| **TRMC** | Time-resolved microwave conductivity |
| **UV** | Ultra-violet |
| **XRD** | X-ray diffraction |
| **$Zn(NO_3)_2$** | Zinc nitrate |
| **ZnO** | Zinc oxide |

# List of Symbols

| | |
|---|---|
| $I_{DS}$ | Output current in the saturation regime |
| $f_t$ | Unity-gain frequency in the saturation regime |
| $W$ | Gate width |
| $L$ | Gate length |
| $C_{ox}$ | Gate capacitance density |
| $\mu_n$ | Electron mobility |
| $V_{GS}$ | Gate voltage |
| $V_{TH}$ | Threshold voltage |
| $e$ | Electronic charge |
| $\tau_{\mathrm{n}}$ | Momentum relaxation time |
| $m_{\mathrm{n}}^{*}$ | Effective electron mass |
| $\vec{v}_{\mathrm{n}}$ | Local drift velocity |
| $\vec{E}$ | Electric field |
| $I$ | Electric current |
| $V$ | Voltage |
| $C$ | Capacitance |
| $\Phi_{\mathrm{B}}$ | Schottky barrier height |
| $\Phi_{\mathrm{M}}$ | Metal work function |
| $\chi_{\mathrm{SC}}$ | Semiconductor electron affinity |
| $E_{\mathrm{F}}$ | Fermi level |
| $A$ | Area |

| | |
|---|---|
| $T$ | Absolute temperature |
| $R_S$ | Series resistance |
| $\eta$ | Ideality factor |
| $A^*$ | Richardson's constant |
| $m^*$ | Electron effective mass |
| $m_0$ | Electron rest mass |
| $n$ | Refractive index |
| $k$ | Extinction coefficient |
| $\tan \delta$ | Loss tangent |

# Chapter 1

## 1 Introduction

### 1.1 Brief history of zinc oxide

Zinc oxide (ZnO) is a very old material; it was used in the Bronze Age for healing wounds. ZnO medicinal uses were mentioned by the Greek physician Dioscorides in the first century [1] and the Persian scholar Ibn Sina (aka Avicenna) presented it in 1025 AD [2] as a preferred treatment for a variety of skin conditions. It was used in the production of brass for many centuries and then went on to become a key ingredient in white paints, porcelain enamels, and rubber manufacture [3]. In the early 1900s, white ZnO powder was extensively used in the cosmetics and pharmaceutical industries [4]. In the 1930s, ZnO lattice parameter studies [5, 6] and some research work pertaining to the photoluminescence and electroluminescence properties of ZnO [3, 7] were published. After the invention of the semiconductor transistor in 1947, systematic studies on ZnO as a compound semiconductor were also undertaken [8]. In 1957, the New Jersey Zinc Company published a book entitled "Zinc Oxide Rediscovered" [9] to promote ZnO as a promising material for semiconducting, photoconductive, luminescent, ferrite and catalytic applications [10]. In 1960, the good piezoelectric properties of ZnO were demonstrated, which resulted in the use of ZnO thin layers in surface acoustic wave (SAW) devices [11]. During the 1960s, sustained efforts were deployed to achieve the growth of ZnO substrates of excellent structural quality. Many ZnO fundamental

properties were then studied and included energy band structures, exciton spectra, electron and hole effective masses, charge carrier transport in intrinsic ZnO (i-ZnO), and phonon properties by Raman scattering [4, 8, 12, 13]. In terms of devices, gold (Au) Schottky barriers were built in 1965 [14] and light-emitting diodes (LEDs) employing p-type $Cu_2O$ were reported in 1968 [15]. In the 1970s, due to the absence of ZnO p-n homojunctions, metal-insulator-semiconductor (MIS) structures and ZnO/ZnTe n-p heterojunctions were presented as alternatives in 1973 [16] and 1975 [17] respectively. Aluminum (Al)/Au ohmic contacts were reported in 1978 [18]. Doping and impurities implantation studies were carried out until the 1970s where the main findings revealed that as-grown ZnO is naturally a highly n-type semiconductor due to high concentrations of unidentified electrically active stoichiometric native point defects formed during growth. In contrast, p-type doping was found to be challenging as it is a general trend to encounter this doping asymmetry in wide band gap semiconductors such as gallium nitride (GaN) and silicon carbide (SiC) [4]. Due to these doping and stoichiometric difficulties and the revolution of the III-V semiconductors for high speed devices in the late 1970s/early 1980s [19-21], research on ZnO took a back step as interest faded away [22].

Many of ZnO ancient applications are still in existence and few applications have been added lately. In optoelectronics, the most established areas of application are [23]: 1) anti-static, electromagnetic interference (EMI)/radio frequency interference (RFI) shielding, and optical coatings [24], which exploit the combined conductive and transparent properties of ZnO; 2) metal-oxide varistors (MOVs), which utilize semiconducting

polycrystalline ZnO [25]; and 3) SAW devices, which benefit from ZnO piezoelectric properties [11].

In the past fifteen to twenty years, a revival and rapid expansion in the research on ZnO as a semiconductor took place. Initially dubbed as a substrate for GaN and related alloys, ZnO became a contending semiconductor for optoelectronic devices in its own right. Some of the reasons behind this growing interest are the availability of large bulk single crystals [26], the strong luminescence generated in optically pumped lasers [27], and the founded expectations to better control the electrical conductivity. In this context, controlling the electrical conductivity of ZnO has traditionally proved to be a major challenge. P-type conductivity presents an even bigger challenge and has not been achieved yet as issues with p-type doping reproducibility and stability are not satisfactorily resolved yet. More so, the reasons behind the unintentional n-type conductivity in as-grown ZnO are still not fully agreed upon at this time. Our approach, outlined in this document, to address these issues consists of growing ZnO thin films in which the concentrations of unintentionally incorporated impurities and intrinsic defects are controlled. Our task is made even more difficult by the fact that our ZnO films are formed by low-cost solution-based growth techniques that usually yield polycrystalline crystals as opposed to the bulk or epitaxial monocrystalline crystals.

## 1.2 Incentives and applications

The material properties of ZnO make it one of the most promising semiconductors for a wide variety of new and emerging applications. The production of electronic devices using solution-based deposition technologies has some decisive technical and commercial advantages compared to competing approaches like vacuum based manufacturing. In particular, the possibilities to scale up production processes to large areas and high volumes by introducing continuous roll-to-roll methods on flexible substrates have been intensely studied and commercially applied [28]. The nonvacuum, solution-based electrodeposition process has the potential to produce large-area uniform precursor films through use of low-cost source materials and low capital equipment expenditures [29]. The following table gives an insight into some commercialization incentives and possible applications:

Table 1.1 Main incentives and applications of zinc oxide.

| Salient properties | Incentives | Applications |
|---|---|---|
| **Safety and low cost** | - ZnO is an abundant, well-known, and low-cost material [9].<br>- It is biosafe, non-toxic, and biocompatible. It possesses antibacterial and antimicrobial properties. | - In most of its applications, ZnO is one of the safest products for the environment and the less costly.<br>- It is notably used in biosensing and other medical applications. |

| | | |
|---|---|---|
| **Semiconducting properties with wide and direct band gap** | - Good semiconducting properties for diodes, transistors, photodetectors, LEDs, and suitable for high-temperature, high-power devices [30]. | - Thin-film transistors (TFTs), power transistors, metal-semiconductor field-effect transistors (MESFETs), Schottky and power diodes, ultra-violet (UV)/blue LEDs, laser diodes, sensors, and photodetectors.<br><br>- Expected to compete favorably with amorphous silicon (a-Si) and organic TFTs and LEDs (OTFTs and OLEDs respectively).<br>- Power electronics. |
| **Availability of large bulk single crystals** | - Growth of active channel layers of better quality than on foreign lattice-mismatched substrates.<br>- Closely lattice-matched to GaN and can act as a substrate for GaN epitaxial growth.<br>- High scalability [30]. | - Minimal lattice mismatch in developing lasers and LEDs.<br>- Enhanced performance of ZnO-based optoelectronic devices in general. |

| | | |
|---|---|---|
| **High transparency in the visible and infra-red spectral ranges.** | - Possibility to fabricate transparent transistors (e.g. transparent TFTs) [31] and transparent conducting contacts/electrodes.<br>- Possibility to replace the less abundant and more costly tin-doped indium oxide (ITO) for transparent electrodes production. | Displays, "see-through" displays, transparent sensors, solar cell electrodes, energy-saving coatings for windows, etc. According to a market forecast by DisplayBank [32], the future of transparent electronics appears to be promising with sharp growth to create a $87.2 billion market by year 2025. |
| **Ultra-violet properties** | Due to UV absorption or emission and its lower cost, ZnO is promising to develop lower cost and more performant UV detectors and devices. | - UV/blue LEDs,<br>- UV detectors,<br>- Solid-state UV devices can be of major utility in water purification, medicine and other environmental applications. |
| **Large exciton binding energy (~ 60 meV) [13]** | Higher thermal stability of the ZnO free exciton. | Important for optical devices based on excitonic effects. |
| **Low-temperature processing** | Huge advantage leading to lower costs and use of plastic, flexible, and | Low-temperature manufacturing, with solution processing or printing, of flexible |

| | | |
|---|---|---|
| | biodegradable substrates [33]. | displays, biosensors, TTFTs, etc. |
| **Wide range of nanostructures** | High surface area to volume ratios [34] | Especially important for sensor and biomedical applications. |
| **Harsh environments material** | Handles high power and high temperature and exhibits high radiation hardness, even greater than GaN [35]. | Suitable for power electronics as well as medical and space applications. |
| **Large piezoelectric constants** | ZnO has high piezoelectric constants with electromechanical coupling larger than that in GaN and AlN [36] | SAW devices, piezoelectric transducers, etc. |
| **Manufacturing aided by the established silicon processing technology** | Large-area processing available currently with magnetron sputtering in particular [37]. | Very important for display and solar cell technology sectors. Solution-processing techniques such as sol-gel and electrochemical deposition are also applicable with the prospects of lowering the costs. |

## 1.3 Fundamental properties of zinc oxide

Although the first semiconductor transistor was constructed in 1947 with germanium (Ge), silicon (Si) replaced it, to a large extent, later on because of the low band gap of Ge and the lack of native germanium oxide. Due to its mature fabrication technology, silicon continues to strongly dominate the commercial market in discrete devices and integrated circuits for computing, power switching, data storage and communication. In terms of high-speed and optoelectronic devices, gallium arsenide (GaAs) is the material of choice because of its higher carrier mobility and higher effective carrier velocity, as compared to Si, as well as its direct band gap versus the indirect band gap of Si. However, neither Si nor GaAs are good candidates for high power and high temperature electronics. Moreover, they cannot achieve emission of wavelengths in the blue to ultra-violet range. For such applications, wide bandgap semiconductors such as SiC, GaN, and ZnO are the most suitable.

ZnO is inexpensive, relatively easy to prepare, abundantly available, chemically stable, environmentally friendly, and most importantly nontoxic. It is a II-VI semiconductor that crystallizes most stably in the hexagonal wurtzite structure $P6_3mc$ at ambient conditions [38], as shown in figure 1.1.

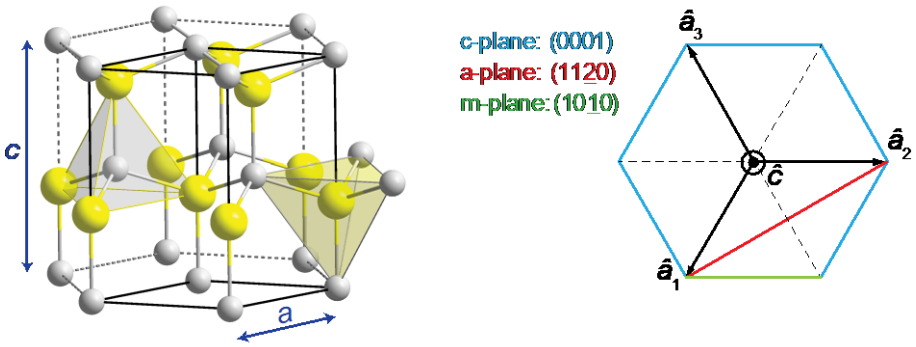


Figure 1.1 The ZnO hexagonal wurtzite unit cell (Source:File:Wurtzite_polyhedra.png - *https://en.wikipedia.org/wiki/Zinc_oxide#/media/File:Wurtzite_polyhedra.png*) with the extended base vectors $\hat{a}_1$, $\hat{a}_2$, $\hat{a}_3$ in the hexagonal base plane and vector $\hat{c}$ in the main symmetry direction.

Zinc has the electron configuration $[Ar](3d)^{10}(4s)^2$; the oxygen configuration is $(1s)^2(2s)^2(2p)^4$. Miller-Bravais planes of special importance are the (0001) c-plane, the (11$\bar{2}$0) a-plane and the (10$\bar{1}$0) m-plane. The hexagonal unit cell has two lattice parameters $a$ and $c$ estimated at $a$ = 0.32495 nm and $c$ = 0.52069 nm [39]. Each anion is surrounded by four next neighboring cations in a tetrahedral arrangement, and vice versa, as a consequence of covalent $sp^3$ bonding. The character of the Zn-O bonds is not purely covalent but has a considerable degree of polarity. The non-central symmetric structure with polar symmetry along the (001) hexagonal c-axis is responsible for the characteristic piezoelectricity and spontaneous polarization. Moreover, it has tremendous effects on epitaxial growth properties, etching behavior, and defects generation in ZnO.

ZnO has a direct and wide bandgap of 3.37 eV at room temperature [40], which corresponds to emission in the ultraviolet spectral range. It exhibits relatively high electron mobility, high transparency in the optical wavelength spectral range, and a

particularly large exciton binding energy [13] that allows for efficient excitonic emission at room temperature. ZnO is a material of interest for high temperature and high power electronics due to its wide band gap, high voltage breakdown strength and good thermal conductivity [41]. Sustained research efforts have been deployed to find the optimum material for power devices that can perform properly under severe electrical and environmental conditions [42]. However, until now, the focus has only been on a few selected compound semiconductors like GaN, SiC, and diamond. ZnO is very resistant to radiation damage [35, 43] and amenable to low-temperature wet and dry chemical etching.

In spite of all the above-stated beneficial features of ZnO, progress has been hampered by the difficulties to accurately control the electrical conductivity as ZnO crystals are unintentionally and intrinsically n-type in general, a topic that has been and is still being vigorously debated and researched [10, 41, 44, 45]. Indeed, controlling the unintentional n-type doping and achieving the p-type conductivity are the goals being presently pursued by researchers worldwide. Our own aim in the present works is to contribute to the improvement of the electrical properties of ZnO grown by very low-cost growth techniques. Hence, our work is highly interdisciplinary as it should in such a widespread scientific topic.

It has become clear that the accurate control of the conductivity in ZnO cannot be achieved without the full understanding of the mechanisms by which electrically active native point defects (i.e., vacancies, interstitials, and antisites) and incorporated impurities affect the electrical parameters of the ZnO film. Traditionally, the unintentional doping has been attributed to the presence of oxygen vacancies ($V_O$) or zinc interstitials ($Zn_i$) [46,

47]. However, some reported density functional calculations and optically detected electron paramagnetic resonance measurements on high-quality ZnO crystals contest the native defects argument [48] on the basis that oxygen vacancies $V_O$ are allegedly deep donors and cannot be responsible for n-type doping. It was also suggested that Zn interstitials $Zn_i$ and Zn antisites $Zn_O$ are unlikely causes of unintentional doping [30, 49]. Research is actively going on to identify the different contributions to the unintentional n-type doping made by native defects, their complexes, substitutional donors (e.g., Al, Ga, In), and hydrogen [4]. Table 1.2 shows that, as a consequence of this unintentional doping, the carrier concentration remains higher than $10^{16}$ $cm^{-3}$ in the highest quality ZnO crystals, mostly grown by advanced vapor-phase techniques. It should be noted that the $8 \times 10^{13}$ $cm^{-3}$ carrier concentration obtained by hydrothermal growth is due to lithium (Li) compensation.

Table 1.2 Best reported carrier concentrations and mobilities in intrinsic ZnO synthesized by different growth methods [50].

| Sample | Dominant orientation | Carrier concentration ($cm^{-3}$) | Electron mobility ($cm^2$ $V^{-1}$ $s^{-1}$) |
|---|---|---|---|
| Monte Carlo calculation | -- | -- | 300 |
| Bulk ZnO grown by vapor-phase transport method | -- | $6.0 \times 10^{16}$ | 205 |
| Bulk ZnO grown by pressurized melt method | (002) | $5.05 \times 10^{17}$ | 131 |
| Bulk ZnO grown by hydrothermal method | (002) | $8 \times 10^{13}$ | 200 |
| ZnO thin films grown on c-plane sapphire by PLD | (002) | $2.0 \times 10^{16}$ | 155 |
| ZnO thin films grown on c-plane sapphire by MBE | (002) | $1.2 \times 10^{17}$ | 130 |

| | | | |
|---|---|---|---|
| ZnO thin films grown on a-plane sapphire by MBE | (002) | $7.0 \times 10^{16}$ | 120 |

Mobility is a measure of the efficiency of electron movement in a solid under the application of an electric field. A high mobility results in a high current and high frequency response. In a device, a high current allows capacitive loads to be quickly charged and discharged and therefore results in high operating speeds. Practically, a higher mobility translates into a wider range of application possibilities. For instance, in a TFT, the output current and the unity-gain frequency, in the saturation regime, are given by [51]:

$$I_{DS} = \frac{W}{2L} C_{ox} \mu_n (V_{GS} - V_{TH})^2 \tag{1.1}$$

and

$$f_t = \frac{\mu_n (V_{GS} - V_{TH})}{2\pi L^2} \tag{1.2}$$

where $W$ is the gate width, $L$ the gate length, $C_{ox}$ the gate capacitance density, $V_{TH}$ the threshold voltage, and $V_{GS}$ the applied gate voltage. We see that both the output current and the unity-gain frequency are directly related to the electron mobility $\mu_n$.

Based on the Drude model and under steady-state conditions, the local electron drift mobility is expressed as [52]:

$$\mu_{\mathrm{n}}(\vec{r}) = \frac{e\tau_{\mathrm{n}}(\vec{r})}{m_{\mathrm{n}}^{*}} \tag{1.3}$$

where $\tau_{\mathrm{n}}(\vec{r})$ is the momentum relaxation time, $m_{\mathrm{n}}^{*}$ the effective electron mass, and $e$ the electronic charge. The mobility $\mu_{\mathrm{n}}(\vec{r})$ relates the local drift velocity $\vec{v}_{\mathrm{n}}(\vec{r})$ to the applied electric field $\vec{E}(\vec{r})$ by

$$\vec{v}_n(\vec{r}) = -\mu_n(\vec{r})\vec{E}(\vec{r}) \tag{1.4}$$

Equation (1.4) is the well-known Drude model equation of charge conduction and is the defining equation for drift mobility at low electric field strengths when Drude's assumption holds (that is, the scattering forces acting like frictional forces are proportional to a moving body velocity: $\vec{F}_{\mathrm{scat}}(\vec{r}) = -m_{\mathrm{n}}^{*}\vec{v}_{\mathrm{n}}(\vec{r})/\tau_{\mathrm{n}}$. At high electric fields, Drude's assumption breaks down as $\tau_{\mathrm{n}}(\vec{r})$, which is determined by the various scattering mechanisms, becomes dependent on $\vec{E}(\vec{r})$; it follows that $\vec{v}_{\mathrm{n}}(\vec{r})$ becomes a nonlinear function of $\vec{E}(\vec{r})$ as clearly shown in figure 1.2. In this case, the electron mobility $\mu_{\mathrm{n}}(\vec{r})$ is strongly dependent on $\vec{E}(\vec{r})$. The theoretical results pertaining to GaN and ZnO in figure 1.2 [53] indicate that, although GaN exhibits higher mobility at low fields, ZnO is expected to have greater saturated drift velocity at high fields.

In single crystalline ZnO, the main scattering mechanisms are due to lattice scattering, impurity scattering, and piezoelectric scattering. Figure 1.3 shows reported Hall mobility of undoped ZnO single crystals at room temperature as a function of the carrier

concentration. In polycrystalline ZnO, grain boundaries constitute crystallographically disturbed regions that result in electronic defects in the band gap.

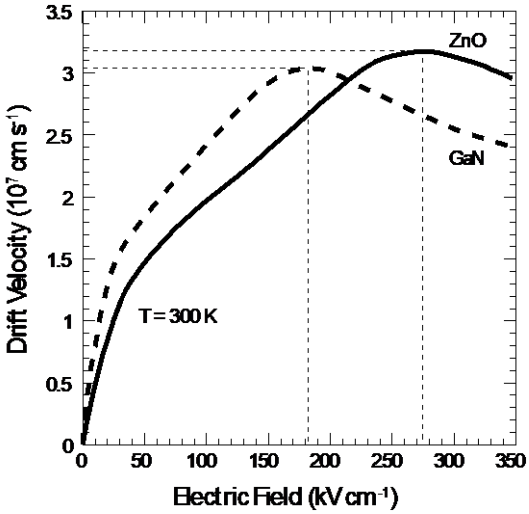


Figure 1.2 Comparison of calculated electron drift velocity vs electric field for wurtzite structure GaN (dashed) and ZnO (solid) at 300 K. Reproduced/adapted with permission from Ref. [53]; Copyright 1999 AIP Publishing.

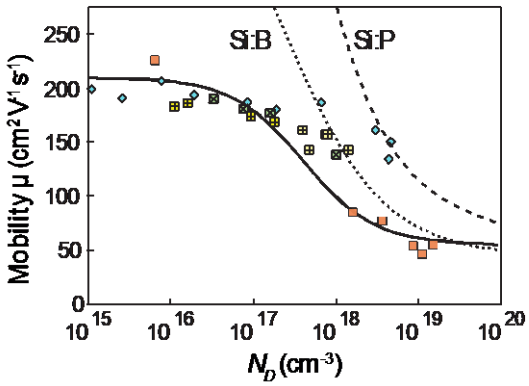


Figure 1.3 Hall mobility of undoped ZnO single crystals at room temperature as a function of the carrier concentrations, adapted from [11] and from different sources: (×) Hutson (1957) [54], (□) Baer (1967) [55], (+) Hagemark and Chacka (1975) [56], (◊) Utsch and Hausmann (1975) [57]. The full lines are semi-empirical fits according to Masetti et al. [58]. For comparison, the dotted and dashed lines for the mobilities of boron- and phosphorous-doped silicon are displayed

respectively. Reproduced/adapted with permission from Ref. [11]; Copyright 2008 Springer Nature.

These defects are charged by carriers from the interior of the grains. Charge balance then creates depletion or accumulation regions around the grain boundary barrier. In n-ZnO films, a depletion zone is generated on both sides of a grain barrier, due to the electron trap character of the defects, with barrier height $\Phi_B$ for electrons. Seto gave the first comprehensive treatment of the carrier transport in polycrystalline silicon [59]. It was later improved by Baccarani et al. [60]. In Seto's model, the carrier transport across the grain barriers is described by the classical thermionic emission (TE). At very high carrier concentrations in the grain, the depletion region becomes narrow enough to enable quantum-mechanical tunneling of the electrons through the barriers (figure 1.4).

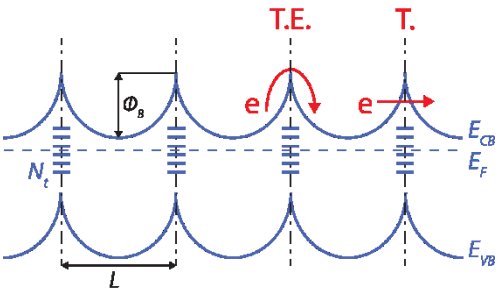


Figure 1.4 Linear row of grains having same length $L$, same doping $N$, and grains barrier height $\Phi_B$ generated by a continuously distributed density $N_t$ of electron trap states [59]. Thermionic emission (TE) and tunneling (T) are the two transport mechanisms for electrons.

Considering the case of dominant thermionic emission across the grain barriers, the effective mobility can be expressed as [59]:

$$\mu_{eff} = \mu_0 \exp\left(-\frac{\Phi_B}{k_B T}\right) \tag{1.5}$$

where $k_B$ is the Boltzmann constant and $T$ the sample temperature. The factor $\mu_0$ can be seen as the mobility inside a grain.

$$\mu_0 = \frac{eL}{\sqrt{2\pi m_n^* k_B T}} \tag{1.6}$$

The barrier height $\Phi_B$ expression is derived for two cases of doping concentration inside the grains:

$$\begin{aligned} \Phi_B &= \frac{e^2 N_t^2}{8\varepsilon_s \varepsilon_0 N} \qquad \text{for} \qquad LN > N_t \\ \Phi_B &= \frac{e^2 L^2 N}{8\varepsilon_s \varepsilon_0} \qquad \text{for} \qquad LN < N_t \end{aligned} \tag{1.7}$$

where $\varepsilon_s\varepsilon_0$ is the static dielectric constant, $N$ the carrier density in the bulk of the grain, $N_t$ the charge carrier trap density at the boundary, and $L$ the grain size. In the case $LN < N_t$, the traps are partially filled and the grains are completely depleted of carriers. For the second case $LN > N_t$, the traps are completely filled and the grains are only partially depleted of carriers.

Polycrystalline ZnO grown by the metal-organic chemical vapor deposition (MOCVD), pulsed-laser deposition (PLD), and sputtering techniques seem to exhibit maximum mobilities in the 50 to 60 $cm^2 V^{-1} s^{-1}$ range [61]. Solution-processed (SP) ZnO, which will be described later in the text, usually exhibits lower electron mobilities; the

available data from the literature provides channel field-effect mobilities (generally lower than bulk Hall mobilities due to additional scattering effects), listed in table 1.3, for such deposition techniques as chemical bath, spin-coating, and spray pyrolysis [62].

Table 1.3 Yearly evolution of the channel field-effect mobilities in ZnO material synthesized by various solution growth processes [62].

| Process | Temperature (°C) | Field-effect mobility ($cm^2 V^{-1} s^{-1}$) | Year |
|---|---|---|---|
| **Spin coating** | 700 | 0.2 | 2003 |
| **Chemical bath** | 100 | 0.25 | 2006 |
| **Spin coating** | 500 | 5.25 | 2007 |
| **Chemical bath** | 700 | 3.5 | 2007 |
| **Spin coating** | 70 | 0.56 | 2007 |
| **Spin coating** | 400 | 1.63 | 2008 |
| **Spray pyrolysis** | 400 | 15 | 2009 |
| **Spin coating** | 500 | 5.26 | 2009 |
| **Spin coating** | 200 | 1.1 | 2009 |
| **Spin coating** | 200 | 0.39 | 2010 |
| **Spin coating** | 500 | 1.29 | 2010 |
| **Spin coating** | 90 | 7.53 | 2010 |
| **Spray pyrolysis** | 370 | 24 | 2011 |
| **Spray pyrolysis** | 400 | 32 | 2011 |

It should be noted that the high mobility of 32 $cm^2 V^{-1} s^{-1}$ reported in 2011 [63] in a TFT was made possible by the use of spray pyrolysis growth and a high-κ gate dielectric, zirconium oxide ($ZrO_2$).

## 1.4 Solution-processing growth techniques

### 1.4.1 Overview

From the fabrication perspective, ZnO offers the possibility of thin film growth through the use of low-cost solution techniques [64, 65]. The solution-processed ZnO films, which usually exhibit polycrystalline structures, are suitable for use as active layers in field-effect transistors (FETs) and for such applications as photodetectors, low-cost electronic displays, transparent conductive electrodes, light-emitting diodes, Schottky diodes, radio frequency identification tags, power inverters, and power devices [66-76]. In conjunction with p-type organic semiconducting films, unintentionally-doped n-ZnO has been used to build circuits that implement complementary logic [77, 78]. A variety of solution techniques have been used to synthesize thin films of ZnO. Chemical bath deposition [64], spray pyrolysis [79], and sol-gel [65, 80, 81] techniques are among the most commonly used. Another solution technique, rarely utilized for electronic devices fabrication, is the electrochemical deposition technique [82, 83]. The solution processes are well adapted to the deposition of solid films on large-area surfaces in a simple and cost-effective way. They enable the synthesis of solid ZnO thin films directly from

solution [84]. Our works involved the sol-gel and electrochemical deposition techniques that are briefly introduced in this chapter.

### 1.4.2 Sol-gel technique

Sol-gel synthesis is a simple and inexpensive solution process to grow high-performance ZnO thin films directly from solution [84]. The integral process basically involves three principal steps as detailed in figure 1.5: preparation of the precursor solution, coating of the substrate, and heat treatment of the gel film.

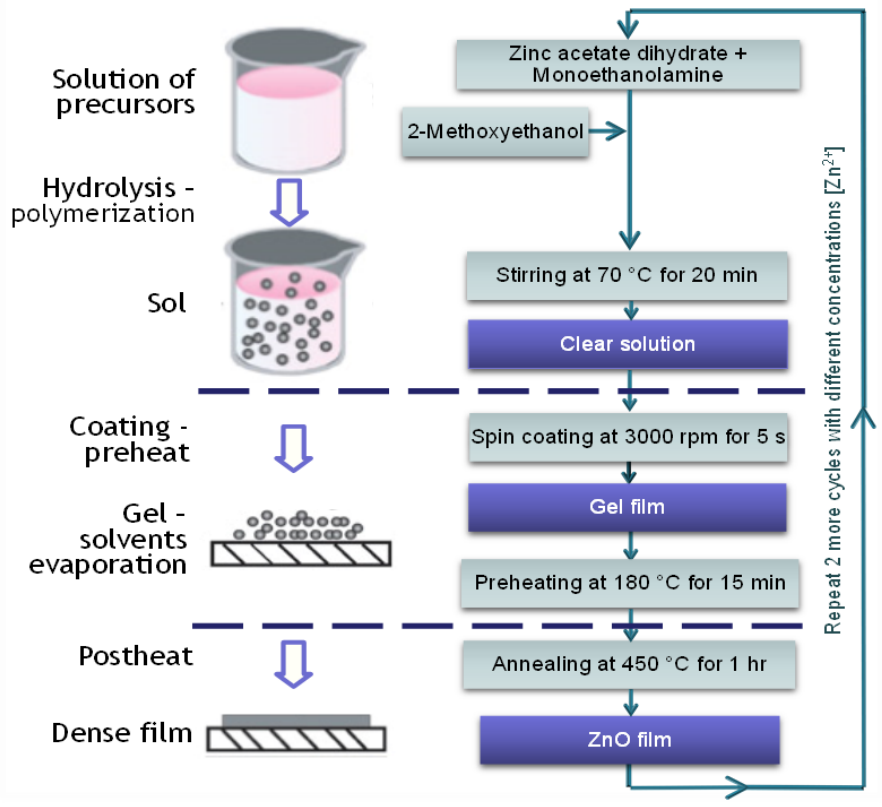


Figure 1.5 A case of integral sol-gel synthesis process.

The crystallization behavior of the grown films is influenced by multiple growth conditions, including the nature of the substrate, the solution chemistry, and thermal treatment conditions. In the sol-gel process, a molecular precursor in a homogeneous solution undergoes a succession of transformations: 1) hydrolysis; 2) polymerization; 3) condensation by dehydration; 4) nucleation; and 5) growth [84, 85]. In sol-gel chemistry, the liquid phase is made up of solid particles suspended in a liquid. Basically, the solution undergoes a series of hydrolysis and polymerization reactions that cause the formation of a colloidal suspension. The subsequent condensation on a substrate, after spin-coating it, and pre-heat treatment serve to remove the liquid phase from the gel and evaporate organic solvents. The ensuing post-heat treatment achieves the final ZnO crystallization phase. As illustrated in figure 1.5, more deposition cycles with varying [$Zn^{2+}$] may be necessary in order to achieve a higher density of nucleation sites, a reduction of pores and pinholes, and a higher film thickness [65].

Our own sol-gel route consists of the dissolution of an organic salt, zinc acetate dehydrate [ZAD: $Zn(CH_3COO)_2{\cdot}2H_2O$], in an alcohol of high molecular weight as solvent, 2-methoxyethanol [2-ME: $CH_3O(CH_2)_2OH$], in addition to the use of a complexing agent of $Zn^{2+}$, monoethanolamine [MEA: $(HOCH_2CH_2)NH_2$], to achieve a stable colloidal solution of high [$Zn^{2+}$] concentration. Figure 1.5 shows a brief summary of our applied process flow. It is noteworthy that preferential orientation for this precursor system, (002) for instance, necessitates pre-heat and post-heat treatments exceeding 300 ºC and 500 ºC respectively [65].

### 1.4.3 Electrochemical deposition technique

Electrochemical deposition (usually shortened to "electrodeposition") is a simple method with potential to achieve high quality ZnO films at low temperatures and low production cost. In a standard electrodeposition process, ions are moved through a solution by an applied electric field to coat an electrode. The electrochemical cell usually has a two-electrode or three-electrode configuration. The latter is required when the electrochemical reactions are not occurring under equilibrium conditions. The third electrode is known as the reference electrode and can have different reduction potentials versus the standard hydrogen electrode (SHE). For instance, the reference electrode used in our electrodeposition process was standard Ag/AgCl electrode (+200 mV vs. SHE). A simplified electrochemical cell configuration is illustrated in figure 1.6.

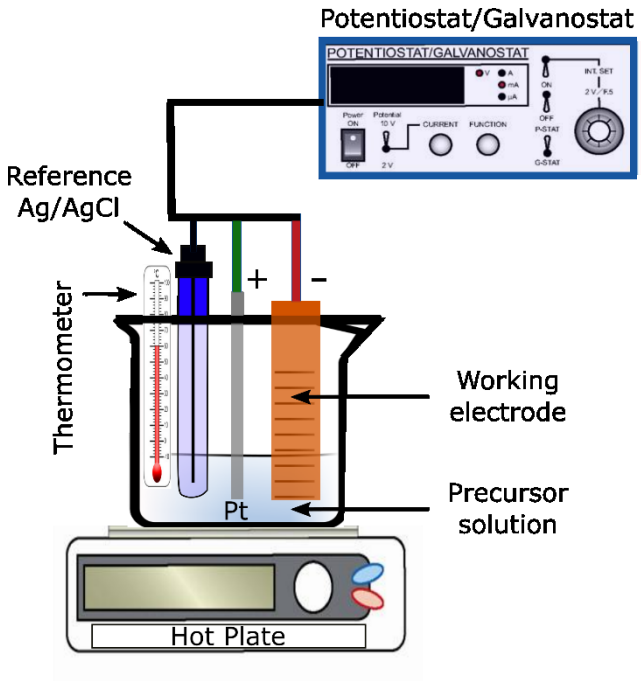


Figure 1.6 A schematic three-electrode electrochemical cell configuration.

The electrodeposition of ZnO has been usually performed from either an aqueous zinc nitrate ($Zn(NO_3)_2$) solution [82] or an oxygenated zinc chloride ($ZnCl_2$) solution [83]. We have opted for the use of the zinc nitrate route because of its lower cost and lower risk of doping the electrodeposited ZnO film. The deposition mechanism of ZnO film from the zinc nitrate $Zn(NO_3)_2$ precursor in aqueous solution is not clear. However, according to the oxide deposition mechanism suggested by Switzer [86], it might be speculated that primary deposition reactions of the ZnO film on a cathode substrate are described by the following scheme:

When the zinc nitrate as a precursor is dissolved in the water, two anionic groups $NO_2^-$ and $OH^-$ are formed in the solution:

$$Zn(NO_3)_2 \rightarrow Zn^{2+} + 2NO_3^-$$

$$NO_3^- + H_2O + 2e^- \rightarrow NO_2^- + 2OH^-$$

Then, the $Zn^{2+}$ ions combine with the $OH^-$ ions to form zinc hydroxide:

$$Zn^{2+} + 2OH^- \rightarrow Zn(OH)_2$$

Zinc hydroxide is usually decomposed into ZnO and water at temperatures above 50 ºC:

$$Zn(OH)_2 \rightarrow ZnO + H_2O$$

The advantages of using zinc nitrate is that it is highly soluble in water, inexpensive, and easy to handle. Compared to the zinc chloride precursor route, ZnO growth from zinc nitrate solutions is reported to be faster and less anisotropic, thereby allowing easier synthesis of larger grains and planar films [87]. Moreover, it does not seem to dope the electrodeposited film, as opposed to the zinc chloride precursor case.

## 1.5 Schottky contacts to undoped zinc oxide

Schottky contacts to ZnO have been studied since Mead's pioneering work in 1965 [14]. To this day, the understanding and control of ZnO Schottky barriers still represents a formidable challenge as wide and variable barrier heights are measured from the same metal on the same ZnO sample by the same person on the same day. For example, the barrier height of gold on ZnO diodes can range from 0 to 1.2 V depending on the crystal structure and quality, the surface pretreatment, and the contact processing conditions [88]. The experimental results often deviate enormously from the idealized Schottky-Mott model:

$$\Phi_B = \Phi_M - \chi_{SC} \tag{1.8}$$

where $\Phi_B$ is Schottky barrier height, $\Phi_M$ is the metal work function, and $\chi_{SC}$ is the semiconductor electron affinity. Experimental $\Phi_B$ usually ranges between 0.6 and 0.8 eV as better predicted by the "Fermi level pinning" behavior assumed in the Bardeen model [89]. The latter model explains that localized semiconductor surface states tend to stabilize the Fermi level $E_F$ in a narrow range of bandgap energies at a metal-semiconductor interface, regardless of metal work function. Indeed, surveying the literature, some trends are clearly established [88, 90-92]: 1) most reported barrier heights are in the 0.6 – 0.8 eV range, independently of the work function of the employed metal, 2) the high-quality Schottky contacts with ideality factors close to unity are very rarely achieved, 3) prior to

contact formation, pretreatment with oxidizing conditions can improve the Schottky barrier height at the ZnO surface but the ideality factors remain high, 4) experimental results of the Schottky barrier height are difficult to reproduce even under the same processing, environmental, and infrastructural conditions, 5) there is no known consistent technology to fabricate Schottky barrier contacts with good reproducibility, 6) Schottky barrier contacts formed to solution-processed ZnO have, in general, much lower quality than those made with vapor-deposited ZnO under vacuum conditions with much higher ideality factors and leakier contacts.

Diode current-voltage (*I-V*) and capacitance-voltage (*C-V*) measurements provide methods of measuring the Schottky barrier height $\Phi_B$. The *C-V* measurement further allows the determination of the depth profile of the effective donor concentration of the semiconductor [93]. According to thermionic emission theory, the *I-V* relation is given by [93]

$$I = I_S[\exp\left(\frac{e(V - IR_S)}{\eta k_B T}\right) - 1] \tag{1.9}$$

$I_S$, the reverse saturation current, is

$$I_S = AA^*T^2 \exp\left(\frac{-\Phi_B}{k_B T}\right) \tag{1.10}$$

where $A$ is the diode area, $T$ the absolute temperature, $V$ the applied voltage, $\Phi_B$ the Schottky barrier height (SBH), $R_S$ the series resistance, and $\eta$ the ideality factor. The theoretical value of 32 A cm$^{-2}$ K$^{-2}$ is usually used for the Richardson's constant $A^*$ in ZnO

by assuming an electron effective mass $m^* \sim 0.27m_0$ [94]. The extraction of the ideality factor from the measured ln($I$)-$V$ data can be conducted by adopting, for instance, Cheung's method [95] which obtains the ideality factor from the linear fit of the d$V$/dln($I$) vs $I$ plot. The deviation from ideality could be due to many factors [88, 91], some of which are illustrated in figure 1.7, including but not limited to image force lowering, thermionic field emission, defect-mediated tunneling, recombination, nonuniform doping, and parasitic capacitances.

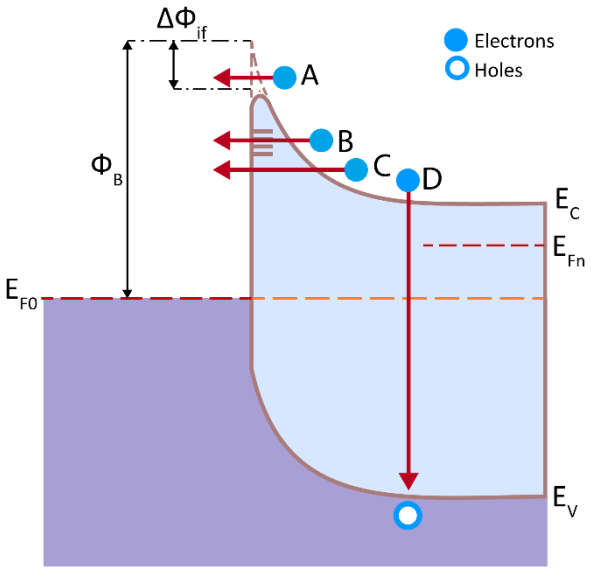


Figure 1.7 Non-ideal carrier transport mechanisms across a Schottky barrier under the forward bias regime: A) image force lowering, B) defect-mediated tunneling, C) thermionic field emission, and D) recombination.

Furthermore, omnipresent shallow interfacial oxide layers on some metals such as silver (Ag) and copper (Cu) contribute to the nonideality of the Schottky barrier by deviating from the parabolic nature of the Mott-Schottky barrier. In most of these nonideal

conditions, the ideality factor is degraded by the dependence of the barrier height on the applied voltage $V$.

The series resistance $R_s$ used in equation (1.9) can be estimated from the high voltage region of the forward $I$-$V$ characteristics through the relation $\Delta V = R_s \Delta I$ [93] in case of ohmic conduction within the $\Delta V$ bias range.

Capacitance-voltage measurements can also determine the free carrier concentration. At a detection signal frequency, parallel diode capacitance density $C_P$ is measured versus voltage $V$ and a plot of $1/C_P^2$ versus $V$ data is then obtained. The fitting of the linearly varying portion of the plot, according to Mott-Schottky analysis, allows extraction of the built-in potential $V_{bi}$ and free carrier concentration from the following expression [93]:

$$N = -\frac{2}{e\varepsilon_S \varepsilon_0}\left[\frac{d}{dV}\left(\frac{1}{C_P^2}\right)\right]^{-1} \tag{1.11}$$

where it is emphasized that $C_P$ is the measured diode capacitance density (per unit area). For the inhomogeneous contact, the $C$-$V$ technique gives the average $V_{bi}$.

# Chapter 2

# 2 High-mobility solution-processed zinc oxide thin films on silicon nitride

## 2.1 Introduction

A brief description of the sol-gel technique is presented in subsection 1.4.2. As discussed, the crystallization behavior of the ZnO films grown by this technique is influenced by multiple growth conditions, including the nature of the substrate that plays an important role in nucleation and in the first growth stage [84]. After studying SP ZnO thin films on glass substrates, Fujihara et al. [96] asserted that the crystallographic orientation is essentially the matter of nucleation and crystal growth and should be explained by influence of the substrates regardless of epitaxial or non-epitaxial growth. SP ZnO thin films have been deposited on several substrate types such as pyrex [97], glass [81], quartz [98], silicon [99], $SiO_2$/Si [100], sapphire [101], and GaN [102]. Yet, silicon nitride ($Si_3N_4$) substrates have been rarely considered as underlayers on which SP ZnO films can be grown; they have been mostly used for comparative studies. The material system comprised of sol-gel ZnO grown on $Si_3N_4$ has not yet been apparently considered for electronic device applications such as thin film transistors. Thus, there exists no significant data in the literature pertaining to the electronic properties, e.g. electron

mobility, of SP ZnO thin films grown on $Si_3N_4$. Films of $Si_3N_4$ are ubiquitously used in semiconductor device and microelectromechanical systems (MEMS) technologies and, in particular, as gate dielectrics for amorphous silicon (a-Si) thin film transistors (TFTs) that are used as switching devices in backbone display technologies.

In this chapter, we report a high effective electron mobility of ~ 33 $cm^2 V^{-1} s^{-1}$ achieved in semiconducting active layers composed of sol-gel-derived undoped ZnO thin films deposited on $Si_3N_4$/p-Si substrates. The ZnO thin films were deposited by the sol-gel spin coating technique on stoichiometric $Si_3N_4$ underlayer films grown on p-type Si substrates by low pressure chemical vapor deposition (LPCVD). For comparison purposes, the same sol-gel chemistry and processing were used to deposit ZnO thin films on thermal $SiO_2$ acquired from a commercial supplier. Of importance is the fact that the process temperatures were intentionally kept below moderate levels of about 450 °C. Indeed, a major challenge in the sol-gel synthesis of ZnO thin films is to lower the process temperatures so as to make the whole growth process adapted to the low cost and low temperature process requirements. Temperatures in excess of 500 °C are required in most ZnO solution processes to achieve larger grain sizes and preferential crystal orientation along the c-axis [84].

The electron mobility $\mu_n$ is a critical material parameter for electronic applications and remains generally low in SP zinc oxide. Achievement of a preferred texture, increase of grain size, use of a high-quality gate dielectric interface, and use of high-κ dielectrics are some of the routes employed to improve the electrical properties of SP ZnO films. In

bottom-gated TFTs used to evaluate $\mu_n$, the insulator below the ZnO film functions as both the growth substrate and the gate dielectric. Consequently, the electrical properties of the gate dielectric-ZnO interface are conjoined with the effects of the substrate on the nucleation and growth of ZnO, complicating analysis and understanding. To separate out these two effects, we used an alternative device configuration consisting of the ZnO film sandwiched between two insulators, the growth substrate at the bottom and a high-κ $HfO_2$ gate dielectric formed by atomic layer deposition (ALD) at the top. This configuration, in conjunction with a recently developed metal-oxide-semiconductor capacitor (MOSCAP)-based mobility extraction technique [103], yielded the effective electron mobilities $\mu_{eff}$ of 33 $cm^2 V^{-1} s^{-1}$ on $Si_3N_4$ substrates and 13 $cm^2 V^{-1} s^{-1}$ on $SiO_2$ substrates. Since the accumulation channel probed in both cases was present at the $HfO_2$/ZnO interface, our measurements demonstrate that $Si_3N_4$ is a superior substrate compared to $SiO_2$ for the growth of high mobility ZnO, a conclusion also supported by structural and morphological characterizations.

When radio-frequency sputtered ZnO films grown on high-κ $HfO_2$ dielectrics were used in TFTs, field-effect saturation mobilities as high as 31 $cm^2 V^{-1} s^{-1}$ have been observed concurrent with threshold voltage instability and high subthreshold slope due to dielectric charge trapping [104, 105]. ALD-deposited $HfO_2$ gate dielectrics have been demonstrated to efficiently suppress charge trapping with an interface trap density at least ten times lower than thermally grown $SiO_2$, when used as substrates for the growth of ZnO films for TFTs, concomitant with subthreshold slopes as low as 0.5 V/decade [106].

Our primary goal was to investigate the electronic mobility of the SP ZnO films grown at moderate temperatures as a function of the growth substrate, i.e. $Si_3N_4$ and $SiO_2$ substrates. For this purpose, a planar MOSCAP structure, illustrated in figures 2.1 and 2.9(a), was used. It consisted of a very thin (10 nm) $HfO_2$ dielectric layer grown by ALD on top of the ZnO thin films. Frequency-dependent capacitance-voltage (*C-V*) characteristics were measured and the effective electron mobility extracted through a mobility extraction model reported by Bothe et al. [103]. This model is more suitable for planar MOSCAP structures that utilize high-κ dielectrics for wide-bandgap semiconductors such as ZnO.

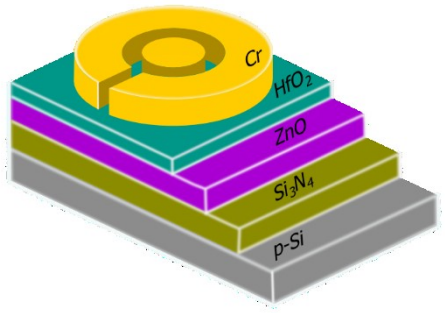


Figure 2.1 Illustration of the multi-layer stacked structure of the fabricated MOSCAP. Reproduced/adapted with permission from Ref. [121]; Copyright 2014 John Wiley and Sons.

## 2.2 Experimental procedures

ZnO thin films were synthesized by the pyrolytic decomposition of spin-coated zinc acetate dihydrate films complexed with monoethanolamine from a solution in methoxyethanol. The gel films were preheated at 180 °C for 15 min and annealed in air

for 1 h at 450 °C, a temperature chosen to ensure compatibility with technologically important glass and indium tin oxide (ITO)-coated glass substrates. The procedures from coating to annealing were performed in three successive cycles whereas solution concentrations of 0.05 M, 0.1 M, and 0.25 M were respectively used at each cycle [107]. The substrate consisted of a 50 nm thick stoichiometric $Si_3N_4$ layer grown on a <100> p-type Si wafer by LPCVD under the following conditions: temperature = 770°C; pressure = 250 mTorr; ammonia ($NH_3$) flow rate = 75 sccm; dichlorosilane ($SiH_2Cl_2$) flow rate = 25 sccm; and deposition rate = 3.25 nm/min. A second type of substrate used for comparison consisted of commercially obtained 200 nm thick thermal silicon oxide on $n^+$-Si.

Atomic force microscopy (AFM) in contact mode and field-emission scanning electron microscopy (FESEM) were used to study the morphology of the films grown on the $Si_3N_4$ and $SiO_2$ substrates. The film thicknesses were obtained from spectroscopic ellipsometry studies. The crystallinity of the ZnO films was examined by X-ray diffraction (XRD) using a Cu-Kα radiation line of 1.54059 Å at glancing incidence in a Rigaku Ultima IV X-ray diffractometer. Residual strains in the ZnO films were investigated using Raman spectroscopy.

To extract the effective channel mobilities, each of the two ZnO films was employed as the semiconductor layer of a MOSCAP. The dielectric layer consisted of a 10 nm thick ALD-deposited high-κ $HfO_2$ film. A 100 nm chromium layer was subsequently sputtered

on top to form the metal contacts. The capacitance measurements were performed on a Signatone probe station using a Keithley 4200-SCS semiconductor parameter analyzer.

## 2.3 Structural properties

### 2.3.1 Ellipsometric measurements

For both substrates, the ZnO films thicknesses were measured by means of a high-precision variable angle spectroscopic ellipsometer (VASE). The ellipsometric angles Ψ and Δ were measured for a wide range of wavelengths at an incidence angle of 75 degrees. The experimental data was then compared to a fit model calculated by assuming highest quality ZnO. We found that our experimental data and the calculated model exhibit a near perfect fit as demonstrated by the following graphical data in figure 2.2:

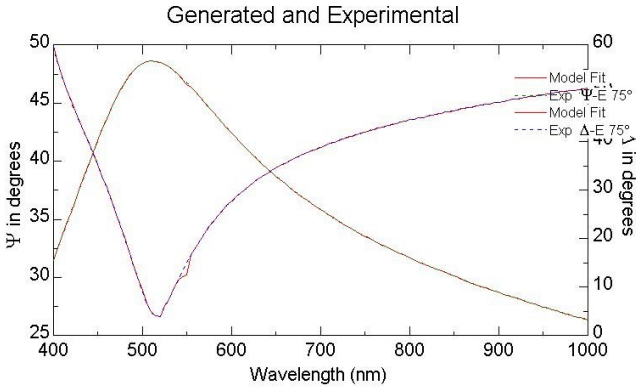


Figure 2.2 For the ZnO/$Si_3N_4$/p-Si stacked structure, the ellipsometric angles Ψ and Δ were measured for a wide range of wavelengths at an incidence angle of 75 degrees. The experimental data (in dashed lines) and the calculated models show near perfect fits. Reproduced/adapted with permission from Ref. [121]; Copyright 2014 John Wiley and Sons.

The measured thicknesses of the multilayer structure ZnO/$Si_3N_4$/p-Si from the fit model are as follows:

Table 2.1 Measured thicknesses of the multilayer stack by ellipsometry:

| | | |
|---|---|---|
| 2 | ZnO | 42.1 nm |
| 1 | $Si_3N_4$ | 49.7 nm |
| 0 | Si | 1 mm (fixed) |

The associated refractive index *n* and extinction coefficient *k* obtained from the fit model are given in figure 2.3:

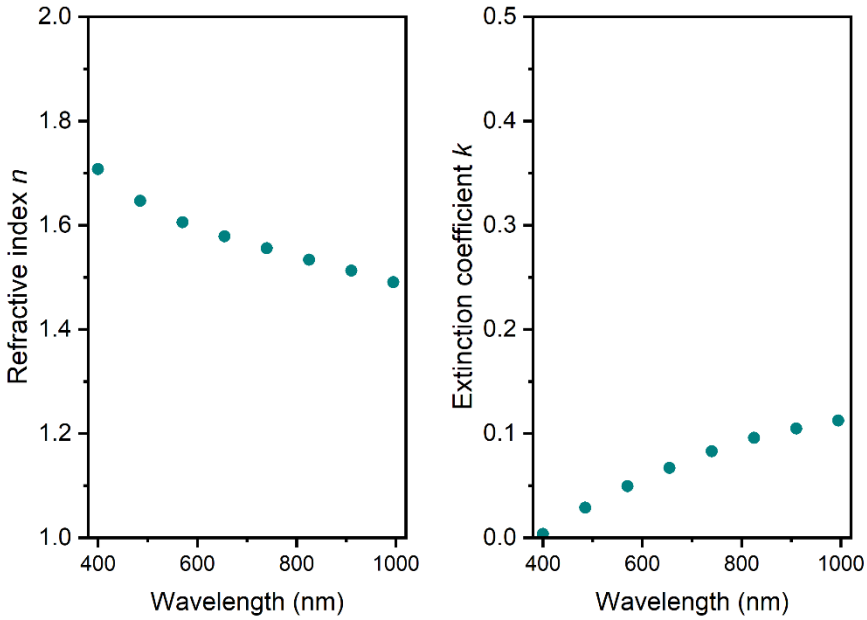


Figure 2.3 The refractive index *n* and extinction coefficient *k* extracted from the ellipsometry data.

## 2.3.2 AFM and SEM characterizations

The AFM images displayed in figures 2.4(a) and 2.4(b) show that the films are continuous with no pores or cracks. The film grown on $Si_3N_4$ clearly reveals larger grain sizes (also confirmed by FESEM images shown in figure 2.5). The respective surface root-mean-squared roughness values were 2.4 nm and 0.9 nm.

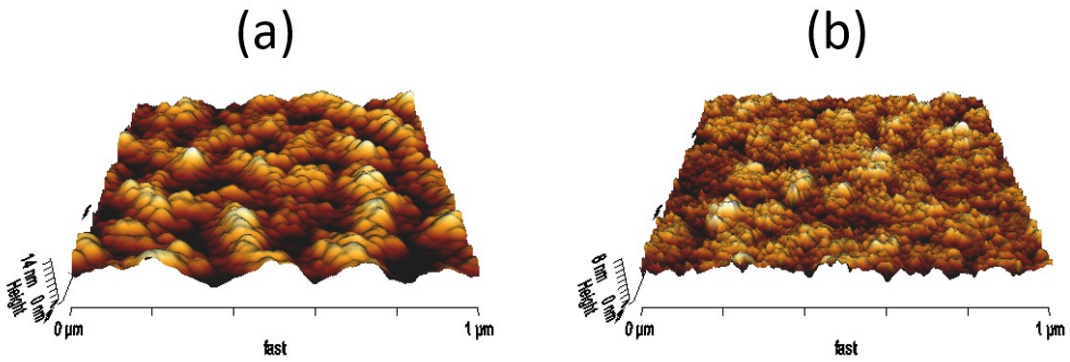


Figure 2.4 Three-dimensional AFM images of the surface morphology of ZnO films grown on (a) $Si_3N_4$/p-Si and (b) $SiO_2/n^+$-Si substrates. Reproduced/adapted with permission from Ref. [121]; Copyright 2014 John Wiley and Sons.

The surface morphologies of the ZnO thin films were also imaged by means of a Hitachi S4800 field emission scanning electron microscope (FESEM). These images are displayed in the following. They clearly agree with the AFM images in terms of the larger grain sizes in the ZnO film grown on $Si_3N_4$.

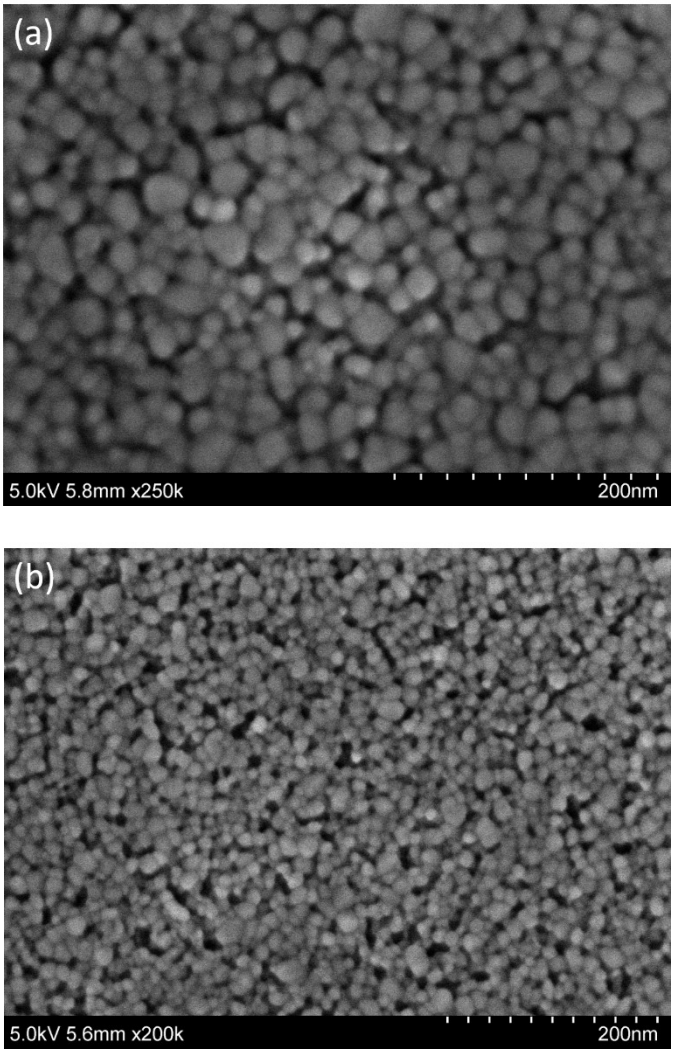


Figure 2.5 FESEM images of the surface morphology of ZnO films grown on (a) $Si_3N_4$/p-Si and (b) $SiO_2/n^+$-Si substrates. Reproduced/adapted with permission from Ref. [121]; Copyright 2014 John Wiley and Sons.

### 2.3.3 XRD characterization

The obtained XRD spectra are shown in figure 2.6 and indicate the presence of the three major diffraction peaks (100), (002), and (101) of polycrystalline wurtzite ZnO (JCPDS 36-1451) even at the relatively moderate preheating and annealing temperatures of 180 °C and 450 °C

respectively. The (002) orientation is sought because

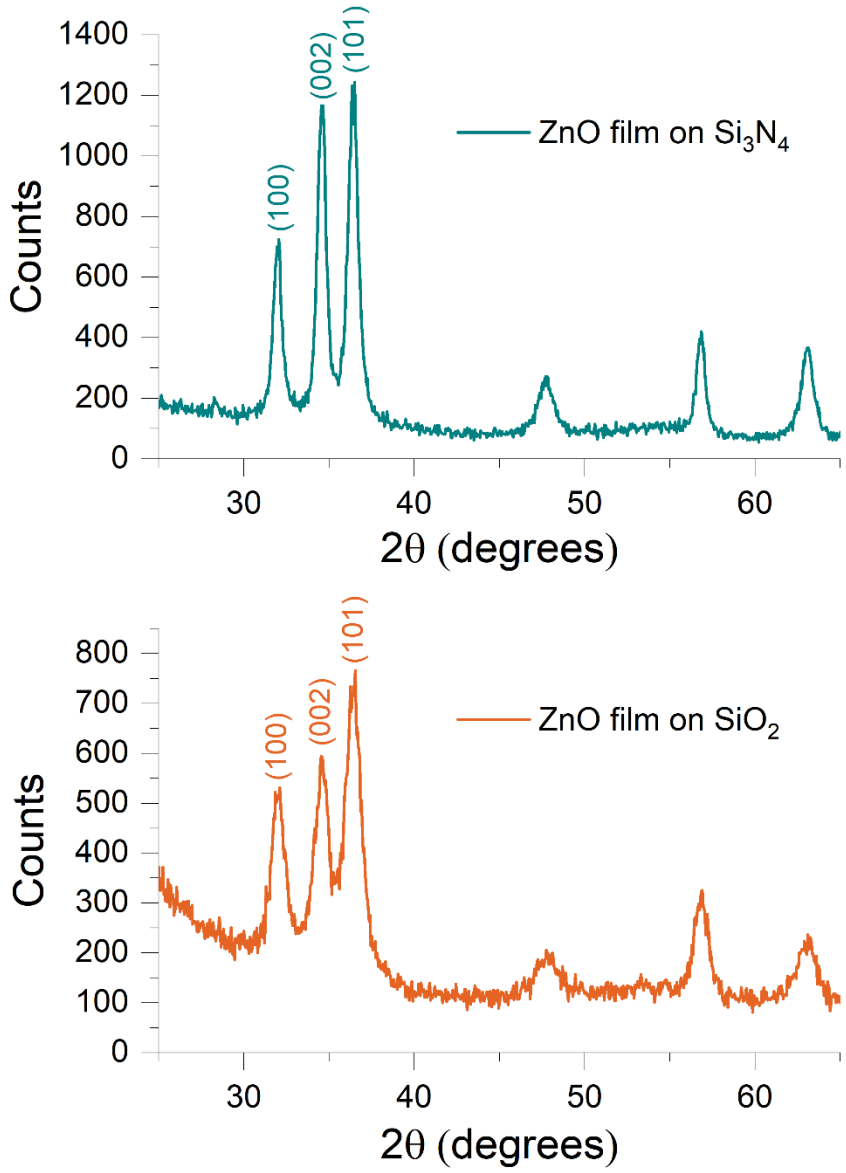


Figure 2.6 X-ray diffractograms of thin ZnO films solution-processed at moderately low temperatures. Diffractograms (a) and (b) pertain to ZnO films grown on $Si_3N_4$/p-Si and $SiO_2/n^+$-Si substrates, respectively. Reproduced/adapted with permission from Ref. [121]; Copyright 2014 John Wiley and Sons.

it is believed that ZnO films with preferential orientation along the (002) plane exhibit the most efficient charge transport in the active channel layer of TFTs [108, 109]. Besides the effect of heat treatment [110], it has been observed that the (002) orientation increases with increasing thickness up to a critical limit [111]. We conclude that our choices of relatively low temperatures and thin films explain the relative major XRD peak intensities. Of interest to us is the comparative study of the XRD patterns corresponding to the films on $Si_3N_4$ and on $SiO_2$; the (002) peaks obtained from the film on $Si_3N_4$ are relatively more intense and exhibit narrower full-width-half-maximum (FWHM) and thus attest to its better (002) orientation.

### 2.3.4 Raman spectroscopy

Figure 2.7 shows the Raman scattering data from ZnO films grown on $Si_3N_4$ and $SiO_2$ substrates collected using a Nicolet Almega XR Raman microscope (ThermoFisher).

There are various Raman active phonon modes for ZnO as predicted by group theory. The presence of $E_2$(high) phonon mode at 437 $cm^{-1}$ is characteristic of the wurtzite phase of ZnO, which is confirmed by Raman spectroscopy [112]. However, stresses induced in the structure lead to a shift in $E_2$(high) mode. A decrease in the wave number of the phonon mode from 437 $cm^{-1}$ is ascribed to stresses in ZnO structures. In the present results, it is found that ZnO films grown on $Si_3N_4$ and $SiO_2$ exhibit downshifts of the $E_2$(high) phonon mode with respect to the wavenumbers. However, the downshifts are too small to be confidently ascertained. Several prior studies report tensile stresses in ZnO films on glass

substrates [102, 113, 114]. A shift towards lower wave number of the $E_2$(high) mode would correspond to some residual stresses in the ZnO films. Residual stresses can be generated in ZnO films due to lattice mismatch and difference in thermal expansion coefficients between films and substrates used. It is reported that under biaxial stresses, $E_2$ mode of ZnO shifts by $\Delta\omega$ ($cm^{-1}$) = 4.4 $\sigma$ (GPa) [115]. By using this relation in the presence of clear shifting, residual stresses and hence disorder in both ZnO films could be assessed and compared [102].

Furthermore, it is observed from FESEM and XRD studies that the average grain size in ZnO/$SiN_x$ films is bigger than that of ZnO/$SiO_2$ films. In polycrystalline thin films, grain size and hence grain boundary scattering play an important role with regard to their structural and electronic properties. The grain boundaries in small grain sized ZnO/$SiO_2$ films may limit the mobility of electrons and affect their electronic properties.

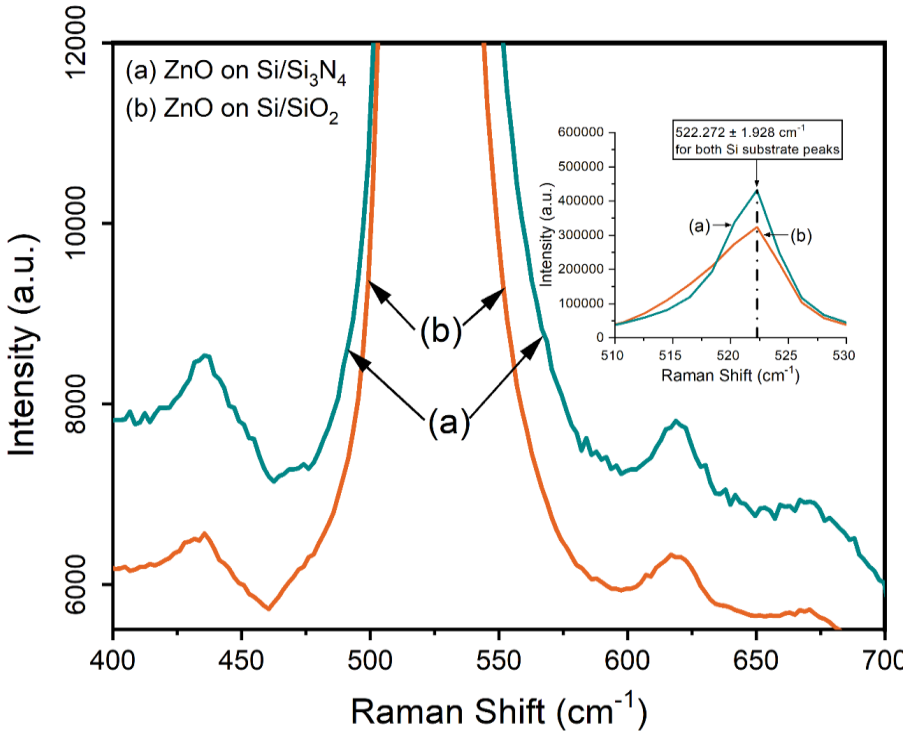


Figure 2.7 Micro-Raman scattering spectra from ZnO films grown on $Si/Si_3N_4$ and $Si/SiO_2$ substrates. Reproduced/adapted with permission from Ref. [121]; Copyright 2014 John Wiley and Sons.

## 2.4 Optical properties

### 2.4.1 Photoluminescence spectra

Figure 2.8 reveals the time integrated photoluminescence (PL) spectra obtained with nanosecond pulsed-laser excitation at 266 nm. Both plots show the near-band-edge ultraviolet emission band characteristic of ZnO PL spectrum. Both peaks occur at 381 nm, which is associated to the free exciton emission in ZnO.

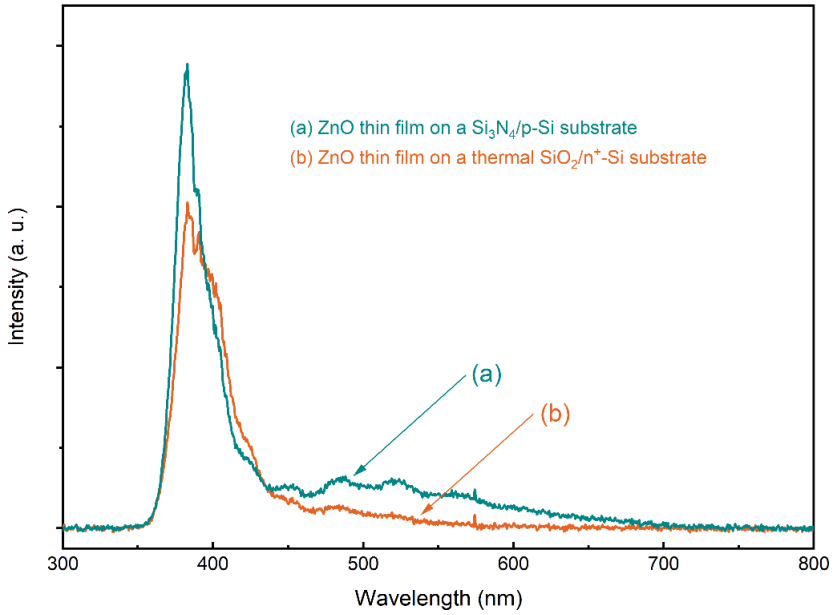


Figure 2.8 Time integrated photoluminescence spectra obtained with nanosecond pulsed-laser excitation at 266 nm. Plots (a) and (b) refer to the ZnO films grown on top of the $Si_3N_4$ layer and the $SiO_2$ layer, respectively. Reproduced/adapted with permission from Ref. [121]; Copyright 2014 John Wiley and Sons.

## 2.5 Electrical properties

### 2.5.1 Electron mobility extraction

A planar MOSCAP architecture and the equivalent circuit model are illustrated in figure 2.9. The MOSCAP equivalent circuit has been designed by modeling it to an equivalent lumped-element circuit model of a transmission line [103]. The low leakage oxide was modeled using a capacitance $C_P$ in parallel with shunt conductance $G_P$. The accumulation layer was treated as a series resistor $R_s$, which is commonly used to describe channel resistance in semiconductors [116]. The

experimental

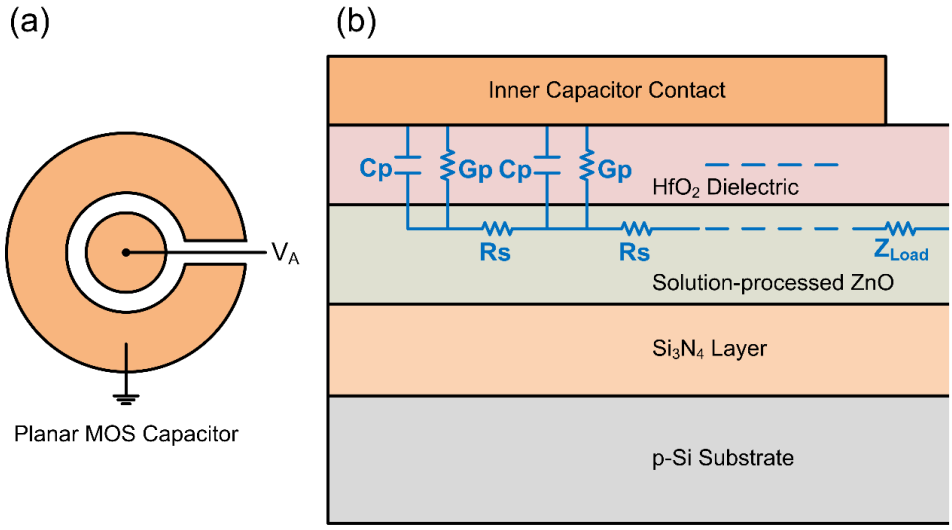


Figure 2.9 Configuration used for MOSCAP mobility extraction and data obtained. (a) Schematic of the modeled planar MOSCAP structure; (b) equivalent lumped-element circuit model under the inner contact of the MOSCAP [103]. Reproduced/adapted with permission from Ref. [121]; Copyright 2014 John Wiley and Sons.

capacitance-frequency ($C_P$-$f$) measurements were first performed. In figures 2.10(a) and 2.10(b), the plotted data points illustrate the experimental $C_P$-$f$ curves of the MOSCAPs employing the ZnO films on $Si_3N_4$ and $SiO_2$ respectively at fixed voltages $V_A$ of 1 V, 2 V, and 3 V. The model parameters $C_P$ and $R_s$ were then extracted for a given applied voltage $V_A$ after accounting for all distributed effects [103]. By using the obtained $C_P$-$V$ and $R_S$-$V$ data sets, shown in figure 2.11, and applying the Schroder mobility extraction method [93] through equations (2.1) and (2.2), we derive the effective electron mobility of the accumulation layer in ZnO film as function of the applied voltage $V_A$.

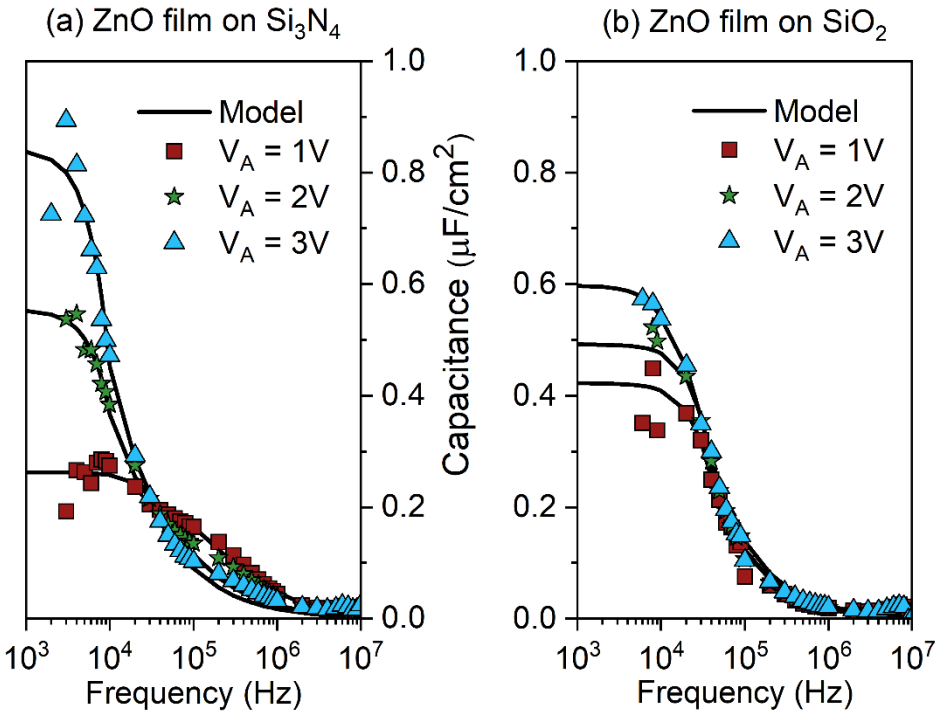


Figure 2.10 Capacitance versus frequency plots from experimental measurements (data points) and applied model (solid lines) for MOSCAPs employing ZnO films on $Si_3N_4$ (a) and $SiO_2$ (b), respectively. Reproduced/adapted with permission from Ref. [121]; Copyright 2014 John Wiley and Sons.

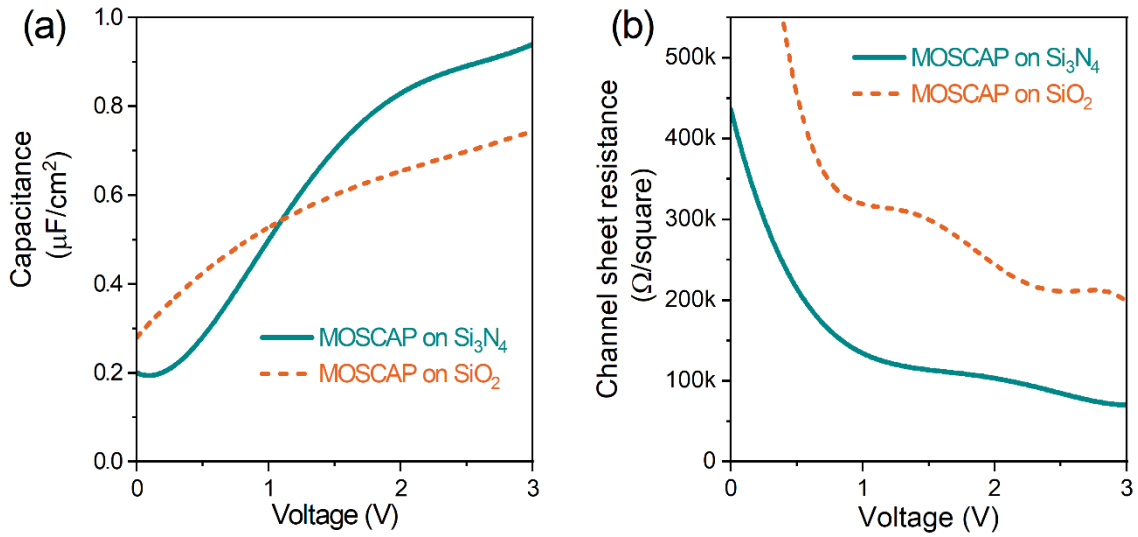


Figure 2.11 The extracted $C_P$-$V$ (a) and $R_s$-$V$ (b) data sets. Reproduced/adapted with permission from Ref. [121]; Copyright 2014 John Wiley and Sons.

$$\mu_{\text{eff}} = \frac{1}{R_S \times Q_n(C_P, V_A)} \tag{2.1}$$

$$Q_n(C_P, V_A) = \int_{V_{FB}}^{V_A} C_P(V)\, dV \tag{2.2}$$

The plots of the derived effective electron mobility versus transverse electric field and charge carrier concentration for both MOSCAPs are shown in figure 2.12. It is readily observed that the ZnO film on $Si_3N_4$ provides the higher effective electron mobilities with a peak mobility as high as 33 $cm^2 V^{-1} s^{-1}$; the peak mobility achieved with the ZnO film on $SiO_2$ on the other hand has a lower value of 13 $cm^2 V^{-1} s^{-1}$. These results not only reveal a very high electron mobility in solution-processed ZnO but are also in line with the XRD,

FESEM and AFM results that assert the more favorable grain morphology and crystalline orientation of the ZnO film grown on the $Si_3N_4$/p-Si substrate. The larger average grain size in ZnO/$Si_3N_4$ films results in fewer grain boundaries. In polycrystalline thin films, grain size and hence grain boundary scattering play an important role in determining the optoelectronic properties. We attribute the lower electron mobility in ZnO/$SiO_2$ films to the higher density of grain boundaries.

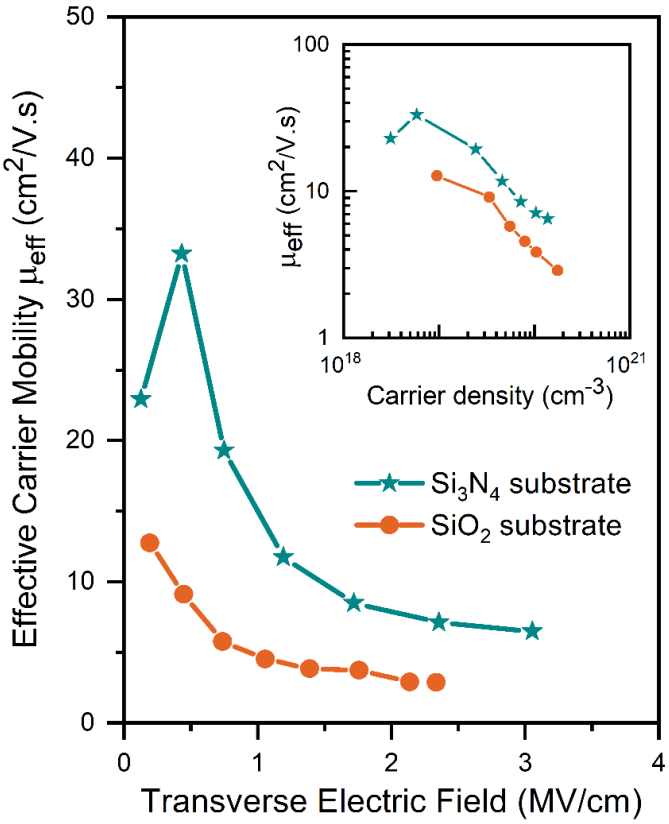


Figure 2.12 Effective electron mobilities in ZnO thin films grown on $Si_3N_4$ and $SiO_2$ as a function of transverse electric field and (inset) carrier density. Reproduced/adapted with permission from Ref. [121]; Copyright 2014 John Wiley and Sons.

The electrical characterization of the MOSCAPs built on the $Si_3N_4$ and $SiO_2$ platforms is summarized in table 2.2. The dopant density $N_D$ and the flat-band voltage $V_{FB}$ were determined by using the $1/C^2$ versus $V$ plot.

Using high-κ dielectrics as growth substrates, improved mobility TFTs have recently been demonstrated in ZnO [63], zinc tin oxide (ZTO) [117], and indium zinc oxide (IZO) [118]. However, there is little clarity on whether the high mobilities resulted merely from the higher accumulation layer carrier densities populating traps or from an improved ZnO film. Secondly, when the growth substrate is also used as the gate dielectric of the TFT, the size and connectivity of the ZnO crystallites in the first few atomic layers of the deposited film may exercise a determinative influence on the electrical properties of the eventual device. In this context, our choice of this mobility extraction model achieves a higher accuracy as a result of the following factors: 1) the present method does not use the MOSFET architecture and hence the simple long-channel MOSFET model applied in the extraction of the so-called field-effect mobility and saturation mobility; 2) the MOSCAP, being a two-terminal device, presents less contact resistance and less parasitic series resistance than a TFT; 3) the ALD technique allows the deposition of low defect density $HfO_2$ dielectric with accurately controllable thickness [119]; and 4) the employed configuration permits decoupling of substrate-dependent nucleation and growth phenomena from the effect of interface traps. Moreover, the ALD deposition of $HfO_2$ on top of the ZnO thin film is expected to result in a good quality interface [119].

Table 2.2 Electrical characterization results of the two MOSCAPs under test. Reproduced/adapted with permission from Ref. [121]; Copyright 2014 John Wiley and Sons.

| Device | $C_{max}$ ($\mu F\ cm^{-2}$) | $N_D$ ($cm^{-3}$) | $V_{FB}$ (V) | $\mu_{eff}$ ($cm^2\ V^{-1}\ s^{-1}$) | $D_{it}$ ($eV^{-1}\ cm^{-2}$) |
|---|---|---|---|---|---|
| MOSCAP on $Si_3N_4$ | 0.94 | $3 \times 10^{18}$ | 0.2 | 33 | $1.3 \times 10^{12}$ |
| MOSCAP on $SiO_2$ | 0.74 | $9 \times 10^{18}$ | 0.1 | 13 | $1.4 \times 10^{13}$ |

### 2.5.2 Interface trap density measurements

To further investigate the $HfO_2$/ZnO interface quality, we carried out interface trap density ($D_{it}$) measurements using our fabricated MOSCAPs. Applying the conductance-frequency method [120] and using our experimental data already available from the MOSCAP mobility extraction technique, we first obtained the equivalent parallel conductance $G_P(\omega)/\omega$ versus frequency at a gate bias of 0.5 V. From the peak $G_P(\omega)/\omega$ values, we found the respective $D_{it}$ values to be $1.3 \times 10^{12}\ eV^{-1}\ cm^{-2}$ and $1.4 \times 10^{13}\ eV^{-1}\ cm^{-2}$ for the MOSCAPs formed on $Si_3N_4$ and $SiO_2$.

## 2.6 Conclusion

We report a high effective electron mobility of 33 $cm^2\ V^{-1}\ s^{-1}$ in undoped ZnO grown by the low-cost solution processing technique. The use of silicon nitride as growth substrate resulted in a significant electron mobility enhancement with respect to silicon

oxide substrates. Lower density of grain boundaries, lower strain, better (002) crystal orientation, and lower interface traps density were exhibited by the ZnO thin films grown on LPCVD $Si_3N_4$ compared to thermal $SiO_2$. These results indicate that the specific properties of the growth substrate affect, through nucleation and growth, the crystalline quality and defect chemistry of the solution-processed ZnO thin film and ultimately its electrical properties.

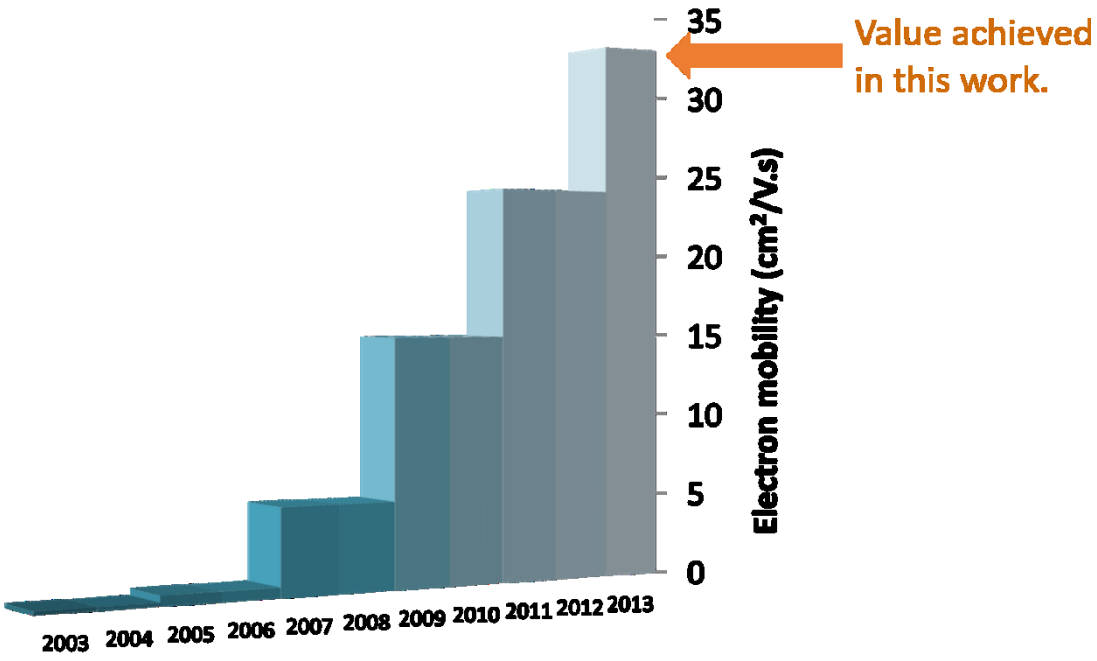


Figure 2.13 Evolution of the electron mobility in solution-processed ZnO grown on low-κ substrates, namely $SiO_2$, glass, and sapphire [62].

# Chapter 3

# 3 Low doped ZnO films for electronic devices by cathodic electrodeposition

## 3.1 Introduction

As previously discussed in section 1.4, sol-gel growth techniques such as spin-coating, doctor blading, and spray pyrolysis attempt to leverage the solution processability of ZnO in the service of low-cost mass-producible, roll-to-roll manufacturing-compatible optoelectronic devices. In chapter 2 and in our published work [121], we have reported the achievement of a markedly high electron mobility of ~ 33 $cm^2 V^{-1} s^{-1}$ in sol-gel grown ZnO thin films. Despite this and other impressive improvements in the electron mobility of these solution-processed films [63, 121], the carrier concentration and interface trap density have still proven difficult to control reproducibly, resulting in low breakdown fields, high sub-threshold slope and inconsistent threshold voltages. Moreover, the majority of growth techniques produce ZnO that exhibits high n-type doping (> $10^{17}$ $cm^{-3}$) and low electron mobilities. While these properties are useful for some applications, such as transparent electrodes and hole blocking layers, it is clear that a better control over the n-type doping and enhancement of the electron mobility are required for more general semiconductor device applications, such as high performance Schottky diodes and thin

film transistors. Another problem with conventional solution-based growth processes for ZnO is their requirement for a high temperature (400–600 °C) precursor pyrolysis step that limits the use of flexible polymeric substrates, complicates the process flow, and increases the thermal budget. Although there exist now a number of available methods to convert a precursor to a stable ZnO film via low-temperature processes, the trade-off is that device performance is generally poorer due to the lower quality of the resulting films [66].

In this work, we use a distinctly simple, low-cost, low-temperature electrodeposition process, carried out in an ambient atmosphere, to synthesize highly-textured ZnO films optimized for electronic performance with low carrier concentration and high electron mobility. From the material side, it was important to achieve a strong preferential texture and large-sized monocrystalline columnar grains. No alloying, doping, annealing, stirring, or vacuum conditions were applied. Electrodeposition of crystalline ZnO thin films from aqueous solutions has been reported independently by Izaki et al. [82] and Peulon et al. [83] in 1996, using nitrate ions and dissolved oxygen as the oxygen precursor, respectively. Pauporté et al. [122] later demonstrated heteroepitaxial film growth on a single crystalline GaN substrate. Electrical characterization of our ZnO films electrodeposited on copper substrates, described in the forthcoming text, revealed a remarkably low carrier concentration of $\sim 2.8 \times 10^{14}$ $cm^{-3}$ and a minimum electron mobility as high as 80 $cm^2 V^{-1} s^{-1}$. These combined results of carrier concentration and charge transport are close to those obtained in hydrothermally grown single crystals of bulk ZnO [26] and are far superior to those obtained in sol–gel ZnO films [109, 123, 124].

Electrodeposition performed at or near the Nernst potential is closer to equilibrium than the highly non-equilibrium kinetically limited sol-gel process (involving spin-coating and pyrolysis steps) [107, 125], and we believe this to be at least partly responsible for the superior structure and composition in electrodeposited ZnO films. Using our electrodeposited ZnO on a copper substrate, we were able to produce high performance Schottky diodes, meant for extracting carrier concentration and carrier mobility, where the copper growth substrate acts as the barrier metal. These diodes exhibited high rectification ratios of $\sim 10^6$, low resistance in the on-state, reverse saturation current densities as low as $8 \times 10^{-10}$ A cm$^{-2}$, and ideality factors as low as 2, in spite of non-optimized ohmic contacts. This set of performance parameters compares very favorably with the current state-of-the-art performance specifications for Schottky diodes utilizing solution-processed ZnO thin films [126].

## 3.2 Electrodeposition of ZnO thin films

By employing the cathodic electrodeposition method, ZnO films were grown on Cu thin films deposited by the DC magnetron sputtering technique. Commercial fluorine-doped tin oxide (FTO) coatings on a glass were also utilized as growth substrates for comparison. The electrolytic solution consisted of 100 mM zinc nitrate hexahydrate (99%, Sigma-Aldrich) dissolved in deionized water. The initial solution pH was 5.2 ± 0.2. The sputtered copper film forming the growth substrate was deposited in one step on a sputtered thin film of titanium tungsten (TiW), which acts as an adhesion and an etch-stop

layer for diode device processing. The underlying substrate consists of commercially supplied wafers of thick silicon oxide on n-type silicon (n-Si).

The deposition mechanism of ZnO films from the zinc nitrate $Zn(NO_3)_2$ precursor in aqueous solution is believed to occur as follows [127]:

$$Zn(NO_3)_2 \rightarrow Zn^{2+} + 2NO_3^-$$

$$NO_3^- + H_2O + 2e^- \rightarrow NO_2^- + 2OH^-$$

$$Zn^{2+} + 2OH^- \rightarrow Zn(OH)_2$$

$$Zn(OH)_2 \rightarrow ZnO + H_2O$$

Linear sweep voltammetry (LSV) was applied to determine the potential window for ZnO deposition. At a temperature = 85 ± 2 °C and a concentration $[Zn^{2+}]$ = 100 mM, the following cathodic current evolution vs potential was recorded:

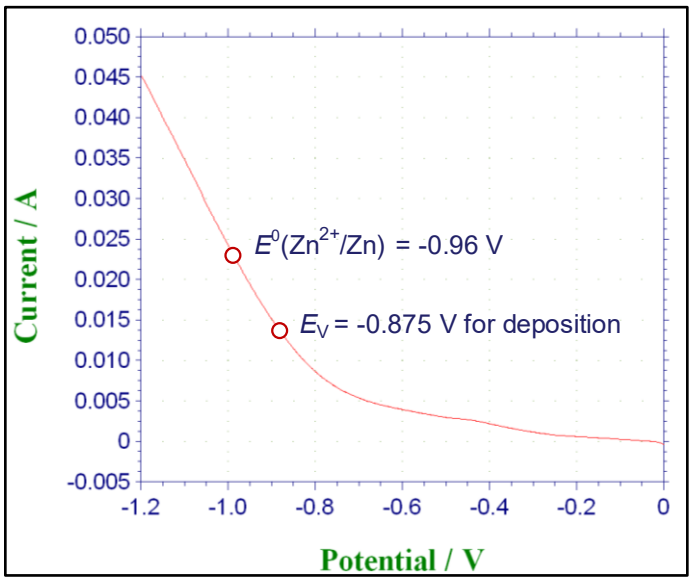


Figure 3.1 Linear sweep voltammetry on ZnO-coated Cu, Temp.= 85 ± 2 ºC, $[Zn^{2+}]$ = 100 mM.

We observe that the emergence of cathodic current (reduction of $NO_3^-$) occurs below -0.6 V. The potential window to deposit ZnO corresponds to a range between -0.6 V and -1 V. The recorded current-time and charge-time evolutions during ZnO electrodeposition at a selected potential of $E_V$ = -0.875 V is:

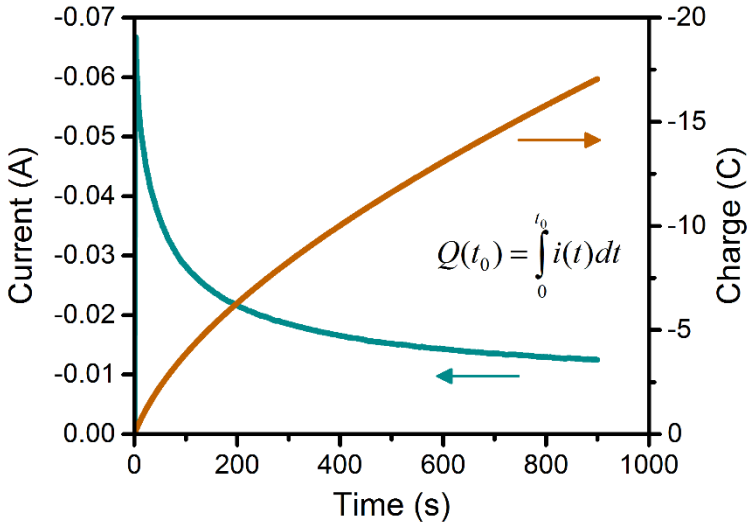


Figure 3.2 Chronoamperometry at $E_V$ = -0.875 V, Temp. = 85 ± 2 ºC, and [$Zn^{2+}$] =100 mM.

The total charge $Q$ applied during electrodeposition is ≈ -17.06 C, corresponding to a thickness of 5700 ± 20 nm as measured by cross-sectional FESEM. Because of the simplified nature of our growth set-up, the electrodeposited area cannot be determined with good accuracy and all of our previous efforts in this regard have ended with errors in the estimation of the electrodeposited charge density by largely overestimating the area in question. To give an example experimentally, we used a larger deposition area (roughly ~ 3 $cm^2$ in figure 3.3) than the area utilized for figure 3.2. A higher applied charge of ≈ -30.01 C is recorded with the same deposition time of 900 s, as expected.

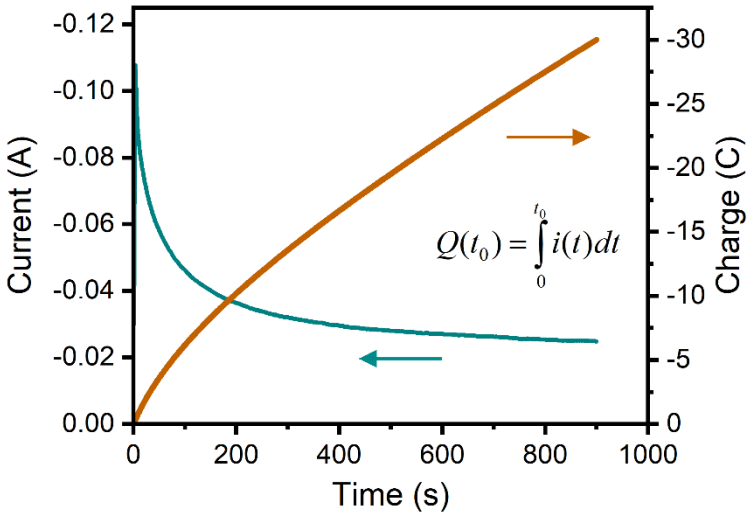


Figure 3.3 An illustrative case of an electrodeposition of ZnO on Cu performed under the same conditions as in figure 3.2 but with a larger deposition area.

In this work, the electrodeposition potential and temperature conditions were set so as to achieve the highest current rectification ratios of the fabricated Schottky diodes. It was found that the most optimal values for the potential ranged between -0.85 V and -0.9 V for temperatures fixed at values between 80 °C and 85 °C. Under these applied electrodeposition conditions, the surface activation of the copper film was necessary to achieve good adhesion at the Cu/ZnO interface. To that effect, we submitted the copper surface to a soft oxygen plasma treatment for a 5 s duration prior to electrodeposition. As a result of contamination removal and surface activation, good interface adhesion was achieved for all applied electrodeposition conditions.

ZnO film electrodeposition on the pretreated copper surface was carried out potentiostatically using a standard three-electrode cell configuration in a glass beaker. The

reference electrode consisted of a standard Ag/AgCl electrode (+200 mV vs the standard hydrogen electrode) whereas a deposited platinum (Pt) film and the pretreated copper substrate were set up as the counter electrode and the working electrode, respectively. A computer-controlled CHI660E electrochemical workstation was used to apply potential and record current-time and charge-time data. For both Cu and FTO substrates, electrodeposition was conducted for 15 min at a fixed cathodic potential $E_V$ of -875 mV and a solution temperature of 85 ± 2 °C with no stirring. As above-mentioned, the total charge registered during deposition was about -17.06 C, corresponding to a thickness of 5700 ± 20 nm measured using cross-sectional FESEM.

## 3.3 FESEM characterization

The investigation of the surface morphology of the ZnO films electrodeposited on copper using the FESEM imaging technique, presented in figure 3.4, reveals a fully continuous film and a much smoother surface than that obtained, under similar growth conditions, in ZnO films electrodeposited on the standard FTO substrate, shown as the inset in figure 3.4. In addition, the cross-sectional FESEM image of a cleaved Cu/ZnO sample reveals a columnar ZnO film structure, as shown in figure 3.5.

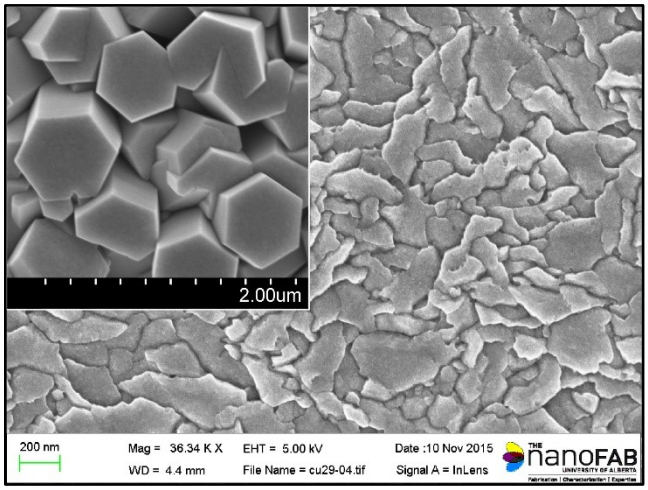


Figure 3.4 FESEM images of the surface morphology of electrodeposited ZnO films on the Cu (FTO for the inset) substrate. Reproduced/adapted with permission from Ref. [185]; Copyright 2016 The Royal Society of Chemistry.

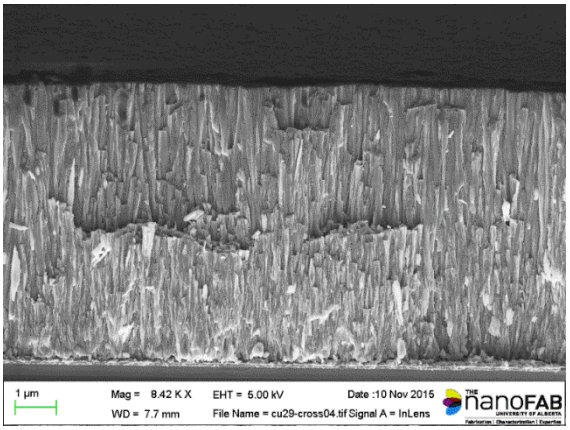


Figure 3.5 Cross-sectional FESEM image of a cleaved ZnO/Cu sample showing columnar grain shapes. Reproduced/adapted with permission from Ref. [185]; Copyright 2016 The Royal Society of Chemistry.

## 3.4 XRD characterization

These observed results were further investigated via the XRD peak profile, displayed in figure 3.6, which exhibits a single intense peak, at a diffraction angle $2\theta =$ 34.33 degrees, indexed to the (002) Miller planes of hexagonal wurtzite ZnO (PDF card 00-001-1136). This is indicative of a highly preferential crystal orientation in which the *c*-axis is normal to the substrate. The peak is very narrow with a FWHM value not exceeding the instrumental peak broadening limit. The calculation of the grain sizes is thus not applicable to the present XRD peak profile but the small FWHM value further attests nonetheless to the large grain size nature of the film surface.

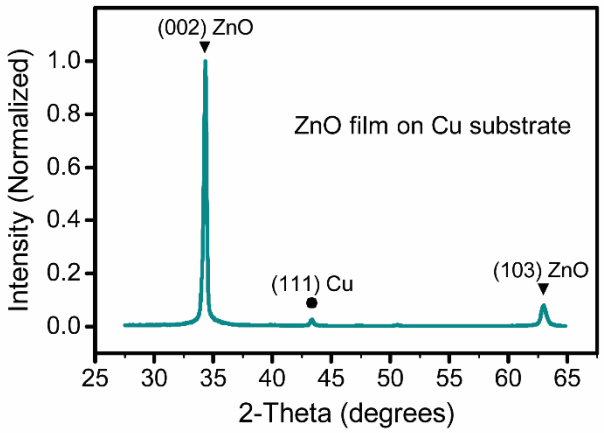


Figure 3.6 The X-ray diffractogram of the electrodeposited ZnO film on Cu substrate shown in figure 3.4. Reproduced/adapted with permission from Ref. [185]; Copyright 2016 The Royal Society of Chemistry.

## 3.5 XPS studies

The ZnO film surface was further investigated using the X-ray photoelectron spectroscopy (XPS) technique with Al Kα radiation (1486.6 eV) as an excitation source. A recorded survey and high-resolution peak region spectra were obtained for the Zn $2p_{3/2}$

and O 1s photoelectron peaks and for the Zn LMM and O KLL Auger peaks as well; they are displayed in figure 3.7. Binding energy scale calibration used the C 1s carbon peak at 285 eV as a reference. The Zn $2p_{3/2}$ and O 1s photoelectron peaks were recorded at binding energies of 1021.6 ± 0.2 eV and 530.3 ± 0.2 eV respectively. The kinetic energies of the recorded Zn LMM and O KLL Auger peaks were 988.6 ± 0.3 eV and 508.9 ± 0.3 eV respectively. These recorded photoelectron and Auger energies match well with the literature values [128] and confirm the formation of ZnO in the electrodeposited film. The modified Auger parameter α', extracted from the survey data by adding the Zn $2p_{3/2}$ peak binding energy to the Zn $L_3M_{45}M_{45}$ peak kinetic energy, is found to be 2010.2 eV which exactly matches the literature value of bulk ZnO [128]. Because the modified Auger parameter is a good indicator of stoichiometry, we conclude that the ZnO film is stoichiometric even at the surface. We note the presence of a second O 1s peak at 531.7 ± 0.2 eV, acquired from deconvolution of the asymmetric O 1s region, usually attributed to oxygen in surface hydroxyl groups [129]. The O 1s subcomponent peaks usually ascribed to carbonaceous, carboxylate-type or carbonate-type species on the film surface are not detected, probably as a result of their very low content(s).

The percentage atomic concentration of oxygen ascribed to stoichiometric ZnO relative to the whole O 1s peak at the film surface is found to be ~ 61%. It is noteworthy that no nitrogen contamination was detected.

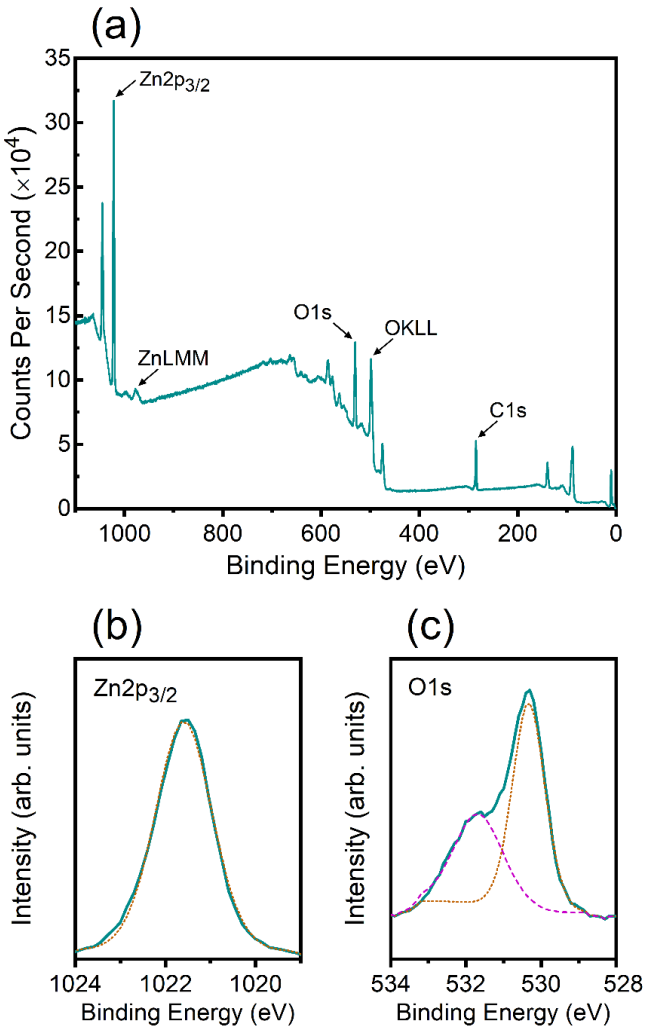


Figure 3.7 Recorded survey (a) and high-resolution peak region spectra for the Zn $2p_{3/2}$ (b) and O 1s (c) photoelectron peaks. Reproduced/adapted with permission from Ref. [185]; Copyright 2016 The Royal Society of Chemistry.

## 3.6 Optical absorption and photoluminescence spectra

The sharp peaks in the room temperature absorption and photoluminescence spectra (figures 3.8 and 3.9 respectively) indicate the high optical quality of the ZnO film. In figure 3.8, we observe a sharp absorption edge and a clear absorption peak. There is a

strong absorbance component due to the substrate. The excitonic absorption peak occurs at a wavelength of 375 nm, corresponding to an excitonic absorption peak energy of 3.31 eV. The thickness of the electrodeposited ZnO film is ~6.9 μm as measured by cross-sectional FESEM. The presence of the clearly visible interference fringes indicate that the electrodeposited ZnO film is continuous and uniform. For the room temperature PL spectra, a relatively intense near-band-edge UV emission peak, characteristic of ZnO, occurs at 385 nm. Deep-level emissions are found to be relatively weak at the excitation wavelength of 345 nm.

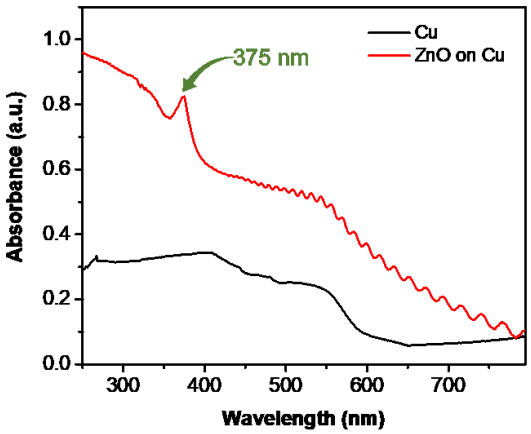


Figure 3.8 Optical spectra were measured by the spectrophotometry technique for two samples: n-Si/$SiO_2$/TiW/Cu (bottom black line) and n-Si/$SiO_2$/TiW/Cu/ZnO (top red line). The thickness of this electrodeposited ZnO film is ~6.9 μm as measured by cross-sectional FESEM. Reproduced/adapted with permission from Ref. [185]; Copyright 2016 The Royal Society of Chemistry.

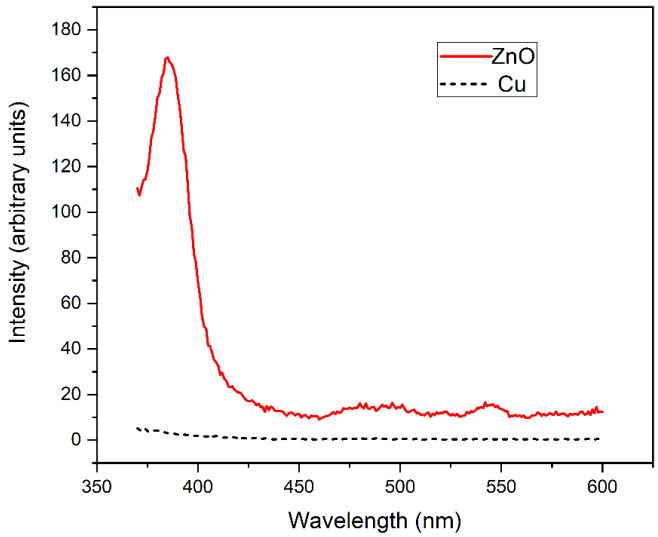


Figure 3.9 Room temperature photoluminescence spectra from two samples: n-Si/$SiO_2$/TiW/Cu (black dotted line) and n-Si/$SiO_2$/TiW/Cu/ZnO (red solid line), were measured for an excitation wavelength of 345 nm. Reproduced/adapted with permission from Ref. [185]; Copyright 2016 The Royal Society of Chemistry.

## 3.7 Electrical characterizations

The fabricated Cu/ZnO/Al diodes, illustrated in figure 3.10, were studied by current–voltage (*I–V*) and capacitance–voltage (*C–V*) measurements performed at room temperature using a Keithley 4200-SCS semiconductor parameter analyzer. The *I–V* characteristics, plotted in figure 3.11(a), show excellent rectifying behavior, with a rectification ratio close to $10^6$, indicating the formation of a good-quality Schottky barrier at the Cu/ZnO interface.

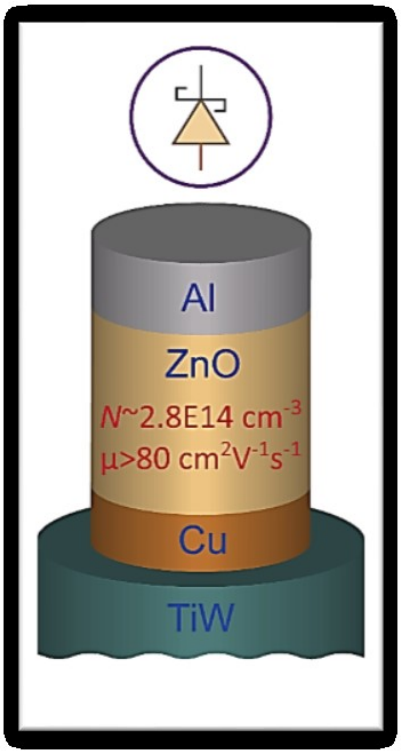


Figure 3.10 Fabricated test Schottky diode. Reproduced/adapted with permission from Ref. [185]; Copyright 2016 The Royal Society of Chemistry.

According to thermionic emission theory, the *I–V* relation is given by equations (1.9) and (1.10). The extraction of the ideality factor from the measured ln(*I*)-*V* data was conducted by adopting Cheung's method [95]. From the linear fit of the d*V*/dln(*I*) vs *I* plot, we obtain an ideality factor of 2.04, which compares very favorably with those reported for Schottky contacts made of ZnO films electrodeposited on other metals [90]. It indicates, on the other hand, that the transport mechanism across the interface is not entirely dominated by thermionic emission, thereby precluding an accurate estimation of the SBH. The measured reverse saturation current density $J_s$ is notably very low with a value of $8 \times 10^{-10}$ A cm$^{-2}$. The observed deviation from ideality is likely due to many

factors [91] and, in large part, to the formation on the copper surface of a very thin interfacial layer of copper oxides, generated by unavoidable air oxidation and soft room-temperature oxygen plasma treatment. It is noteworthy that the XRD pattern does not show any diffraction peaks related to $Cu_xO_y$ copper oxides, which supports the assumption that the copper oxide layer would only be a few monolayers thick, not exceeding the native copper oxide layer thickness of ~ 3.2 nm obtained after exposing copper to open air for much longer times [130]. Accordingly, the measured *I–V* data follow a linear dependence for voltages between 0.1 V and 0.4 V indicating that current tunneling and carrier recombination are the dominant contributions to the measured current in this bias regime. Lateral contact inhomogeneities are also expected to contribute significantly to the Schottky barrier non-ideality [91] in view of the large circular contact area (radius = 165 μm) of the diode. The series resistance $R_s$ used in equation (1.9) can be estimated from the high voltage region of the forward *I–V* characteristics through the relation $\Delta V = R_s \Delta I$ [93], where ohmic conduction is established within the bias range $\Delta V$. By taking $\Delta V$ between 1.75 V and 2.5 V, a value $R_s = 182\ \Omega$ is obtained. This value is relatively low considering the non-optimized quality of our ZnO/Al ohmic contact in terms of its resistance value. Knowing that the series resistance fraction in the semiconductor $R_{s,sc}$ has to be lower than the diode series resistance $R_s$ ($R_{s,sc} < 182\ \Omega$) and using the known device dimensions (Al contact radius = 165 μm and ZnO film thickness = 5700 nm), an upper limit of the ZnO film resistivity was estimated as $\rho < 273\ \Omega$ cm.

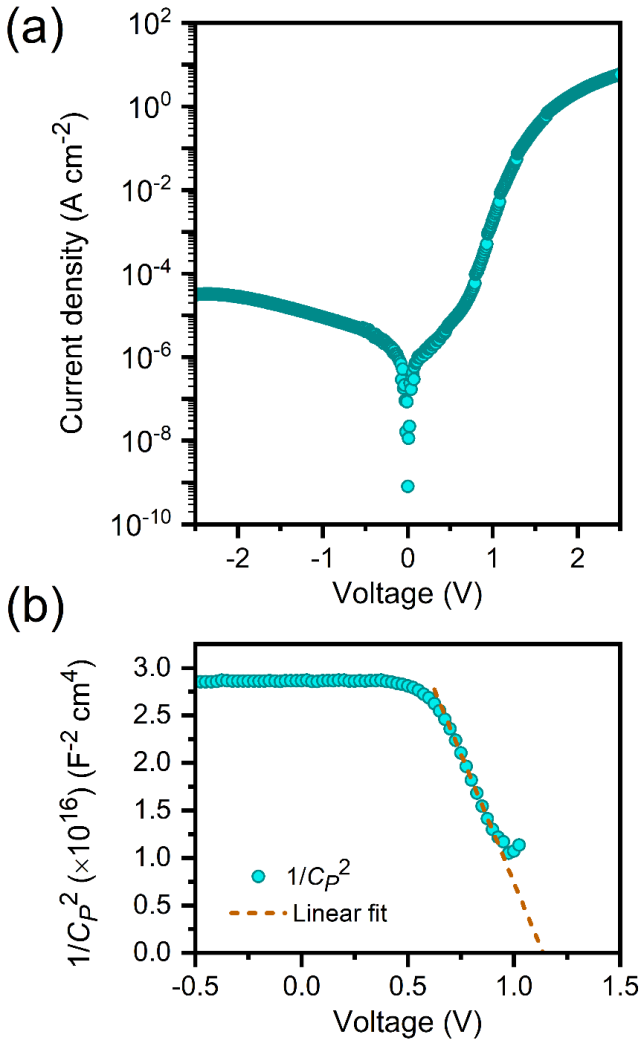


Figure 3.11 (a) Room temperature *I–V* characteristics plotted on a semi-log scale, and (b) the room temperature $1/C_P^2$–*V* plot taken at 50 kHz with respective linear fit. Both current and capacitance are given per unit area. Reproduced/adapted with permission from Ref. [185]; Copyright 2016 The Royal Society of Chemistry.

Capacitance-voltage measurements were also carried out at room temperature to determine the free carrier concentration. At a detection signal frequency of 50 kHz, diode capacitance density $C_P$ was measured vs voltage *V* and a plot of $1/C_P^2$ vs *V* data is shown in figure 3.11(b). We used the signal frequency of 50 kHz because it gave the most

consistent results. The plot reveals that the ZnO layer is fully depleted at the zero-voltage bias, an indicator of low doping levels in view of the large layer thickness (~ 5700 nm). The fitting of the linearly varying portion of this plot, according to Mott–Schottky analysis, allows the extraction of the built-in potential $V_{bi} = 1.16$ V and free carrier concentration $N = 2.8 \times 10^{14}$ cm$^{-3}$ from equation (1.11). The value of the built-in potential is clearly overestimated as it falls above the range of values reported in the literature [88]. Two commonly known reasons contribute to this discrepancy: (1) the barrier nonparabolicity, due to the interfacial oxide shallow layer, leads evidently to an overestimation of $V_{bi}$ by the Mott-Schottky analysis, and (2) in Schottky barriers with lightly doped semiconductors, the measured capacitances are usually very small (< 4 pF in our case) and become prone to errors introduced by small but non-negligible excess shunt capacitances [131], which have the effect of overestimating both $V_{bi}$ and $N$.

In light of the relatively low resistivity ($\rho < 273$ Ω cm), the low level of unintentional n-type doping, $N = 2.8 \times 10^{14}$ cm$^{-3}$, achieved in our electrodeposited ZnO is remarkable and is on par with the low carrier concentration values reported in hydrothermally grown bulk ZnO [26]. Although the origin of the unintentional n-type doping in ZnO is still under debate within the scientific community, it is commonly attributed to native defects and unintentional incorporation of impurities such as hydrogen. A low level of unintentional doping thus indicates a low defect-grown ZnO film. The low values of the estimated $\rho$ and $N$ hint at a significantly high electron mobility in the bulk semiconductor. Applying the relations $1/\rho = qN\mu$ and $\rho < 273$ Ω cm, a low limit of the mobility $\mu$ can be assessed: $\mu >$ 80 cm$^2$ V$^{-1}$ s$^{-1}$. The mobility in our ZnO films is greatly enhanced by the low densities of

scattering centers and grain boundaries owing to the good film crystalline quality and vertical carrier transport along the (002)-oriented columnar film structure.

## 3.8 Conclusion

We have combined a suitable substrate (copper) with an underutilized low-cost processing technique (electrodeposition) to synthesize ZnO films with extremely low free carrier concentrations and strong crystallographic texture. The underlying copper substrate was found to form an excellent Schottky barrier with the electrodeposited ZnO film. The resulting diodes stood out from previously reported solution-processed ZnO devices in terms of their superior electrical characteristics. Good electron transport in these films was inferred from the ohmic conduction region obtained at high forward bias. These electrodeposited ZnO films are particularly suitable for building large-scale low-cost vertical devices with high breakdown voltage and high current handling capabilities.

# Chapter 4

# 4 High performance Schottky diodes on flexible substrates using ZnO electrodeposited on Cu

## 4.1 Introduction

We have established in table 1.1 that one of the salient properties of zinc oxide is its low-temperature processability, which gives ample possibilities to achieve lower processing costs and make use of plastic, flexible, and biodegradable substrates [33]. Owing to the high theoretical maximum values of its electron mobility, piezoelectric coefficient, electron saturation velocity, breakdown field and other physical properties, ZnO is particularly attractive for use in high-power and high-frequency rectifiers, flexible ultraviolet photoconductive sensors, mechanical sensors, electron transport layers in flexible solar cells and light emitting diodes, thin film transistors for displays, and logic circuits [132-134]. However, processing problems have stymied the increased adoption of ZnO-based materials and devices for flexible optoelectronics which have historically relied mainly on organic and molecular materials [135]. As discussed in chapter 1, electrical parameters from solution-processed ZnO thin films rarely reach the performance of their gas-phase counterparts. Moreover, the high temperatures (minimum of 400 °C) required for the pyrolysis of zinc oxide precursors and sintering of the formed nanoparticles render these solution-processing growth methods incompatible with flexible polymeric substrates. While ZnO nanowires and nanomembranes grown by solution or

gas-phase methods have shown improved structural and electrical characteristics, it is still challenging to assemble and orient them across defined electrodes over large areas [136, 137].

ZnO thin films are also generally plagued by substrate and interface issues which interfere with the fabrication of consistent Schottky diodes, as discussed in the previous chapters. In addition to thermal incompatibility, existing solution-based processes have not been able to produce good rectifying metal-semiconductor junctions even on other technologically relevant substrates such as glass and silicon. Solution-processed ZnO Schottky diodes (including those made from nanowires) are, in general, leaky (on-off ratio < $10^4$) and have poor ideality factors (~ 8 to 10) mainly due to poor control of the carrier concentration (commonly above $10^{17}$ $cm^{-3}$) and the difficulty in controlling the electrical properties of the heterointerface between ZnO and the high work function metal [88].

In our work presented in chapter 3, we have employed an underutilized low-cost processing technique for the synthesis of ZnO films on rigid copper-coated substrates. By optimizing the ZnO synthesis process for electronic performance, we were able to address a number of the aforementioned problems. The cathodic electrodeposition of zinc nitrate $Zn(NO_3)_2$ precursor in aqueous electrolytes occurs nominally at temperatures below the boiling water mark, thereby largely facilitating the use of flexible substrates. The deposition mechanism of ZnO thin films from the aqueous zinc nitrate precursor solution has been given in subsection 1.4.3. It is reproduced here for convenience. It is believed to occur as follows [127]:

$$Zn(NO_3)_2 \rightarrow Zn^{2+} + 2\ NO_3^-$$

$$NO_3^- + H_2O + 2\ e^- \rightarrow NO_2^- + 2\ OH^-$$

$$Zn^{2+} + 2\ OH^- \rightarrow Zn(OH)_2$$

$$Zn(OH)_2 \rightarrow ZnO + H_2O$$

where the electrodeposition process, involving the electro-reduction of nitrate to nitrite ions and formation of ZnO via the generation of hydroxide ions, is illustrated in figure 4.1(b).

The ZnO films were electrodeposited on a copper layer which forms the top layer on a flexible substrate. The Cu/ZnO junction forms a Schottky barrier. Point-contact devices of 5 μm radius were used to isolate the effect of the ZnO film bending (mechanical deformation) on the electrical stability of the Cu/ZnO interface. The probing contacts to the ZnO film and copper substrate film are made of tungsten. With no bending, the resulting diodes showed rectification ratios as high as $10^6$ with ideality factors around 2.7.

## 4.2 Experimental procedures

The cathodic electrodeposition method was employed to grow ZnO films on 25 nm-thick sputtered copper films. Adhesion layers of 15 nm-thick titanium were sputtered prior to copper, on top of 50 μm-thick Dupont Kapton type E substrates. The coefficient of thermal expansion of Kapton type E is 16 ppm/°C. The electrolytic solution consisted of 100 mM zinc nitrate hexahydrate (99%, Sigma-Aldrich) dissolved in MilliQ quality water. The

deposited copper was stored under vacuum conditions from the time it left the sputter chamber to the time of use. Prior to deposition, the copper substrate was rinsed in acetone and methanol and blown dry with nitrogen gas. The electrodeposition process was carried out potentiostatically using a three-electrode cell configuration in a glass beaker. A standard Ag/AgCl electrode was employed whereas a deposited platinum film and the Kapton/Ti/Cu substrate were set up as counter electrode and working electrode, respectively. A computer-controlled CHI660E electrochemical workstation was used to apply potential and record current-time and charge-time data.

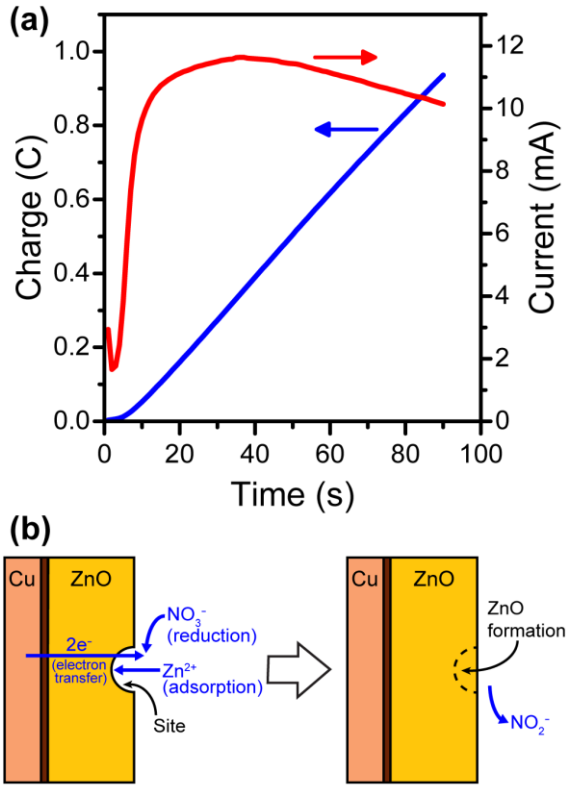


Figure 4.1 Recorded current-time and charge-time data during electrodeposition, and (b) illustration of the electrodeposition process showing electro-reduction of nitrate to nitrite ions and formation of ZnO [127]. Reproduced/adapted with permission from Ref. [33]; Copyright 2016 Electrochemical Society, Inc.

A schematic of the electrodeposition set-up is presented in figure 1.6. Electrolysis was conducted for 90 s at a fixed cathodic potential $E_V$ of -850 mV and a solution temperature of 70 ± 2 °C with moderate stirring. The chosen $E_V$ is within the suitable range of potentials deduced from the cyclic voltammogram shown in figure 4.2. The voltammogram indicates that cathodic current begins around -0.6 V. We found that the range between -0.75 V and -0.95 V is most suitable for the formation of ZnO films. The voltammogram was taken on a computer-controlled CHI660E electrochemical workstation. The initial solution pH was 5.2 ± 0.2. It should be emphasized that the final set of growth conditions were chosen based on optimization of rectification ratio and leakage current.

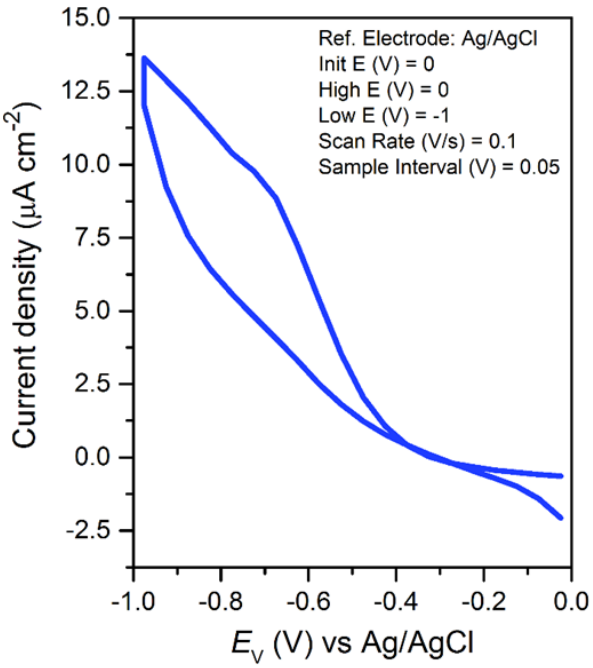


Figure 4.2 Cyclic voltammogram of a copper-coated flexible Kapton substrate cathode over the potential range 0 V to -1 V (vs Ag/AgCl) in 100 mM zinc nitrate hexahydrate solution at 70 ± 2 °C. The voltammogram was taken on a computer-controlled CHI660E electrochemical

workstation. Reproduced/adapted with permission from Ref. [33]; Copyright 2016 Electrochemical Society, Inc.

The crystalline structure of the electrodeposited ZnO films was analyzed through the XRD technique from a Bruker D8 Discover diffractometer with a 1.5406 Å Cu-Kα line. Surface images were obtained by a Hitachi S-4800 FESEM with acceleration voltage of 5.0 kV. Surface morphology was also explored with a Bruker Dimension Edge AFM. A transmission electron microscopy (TEM) image (magnification: 10k) of the Kapton/Ti/Cu/ZnO interfaces region was taken on a Hitachi H-9500 E-TEM. Electrical characterizations of the Schottky diodes were performed on a Signatone probe station using a Keithley 4200-SCS semiconductor parameter analyzer.

## 4.3 Film investigation by imaging techniques

For an electrodeposited film area of ~ 1.54 $cm^2$ and a deposition time of 90 s, figure 4.1(a) reveals a deposited charge of ~ -0.6 C $cm^{-2}$ corresponding to an average ZnO film thickness of ~ 120 nm measured by cross-sectional FESEM. The deposited films were thus kept sufficiently thin to study the influence of bending on their electrical stability. Prior to ZnO electrodeposition, the Cu film surface roughness was measured by the AFM technique and the root mean squared roughness over a 0.5 μm × 0.5 μm surface area was found to be 1.7 nm.

The FESEM image of the ZnO film, presented in figure 4.3(a), displays a relatively smooth surface morphology in spite of the small film thickness. The AFM image taken in tapping-mode, in figure 4.4, reveals a continuous film. The transmission electron microscopy (TEM) image (magnification: 10k) in figure 4.3(b) further confirms that the ZnO film is continuous in spite of its small thickness.

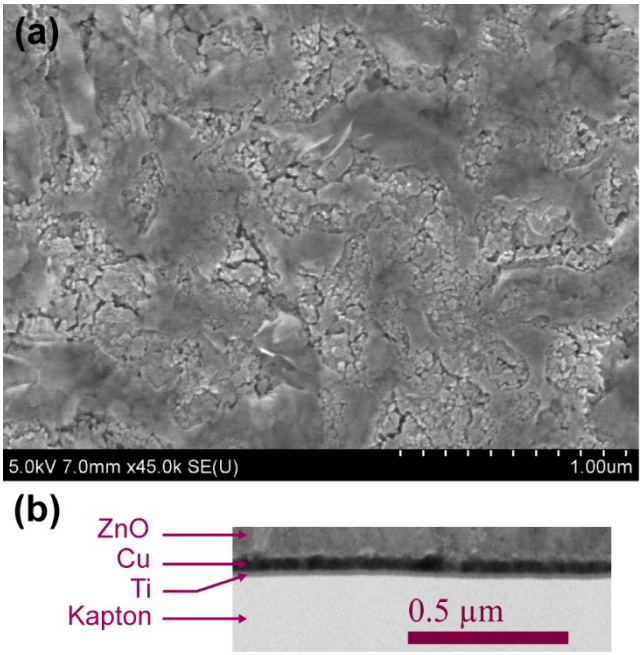


Figure 4.3 (a) FESEM image of the surface morphology of the ZnO film electrodeposited on Kapton/Ti/Cu substrate, and (b) TEM image (magnification: 10k) of the Kapton/Ti/Cu/ZnO interfaces region. Reproduced/adapted with permission from Ref. [33]; Copyright 2016 Electrochemical Society, Inc.

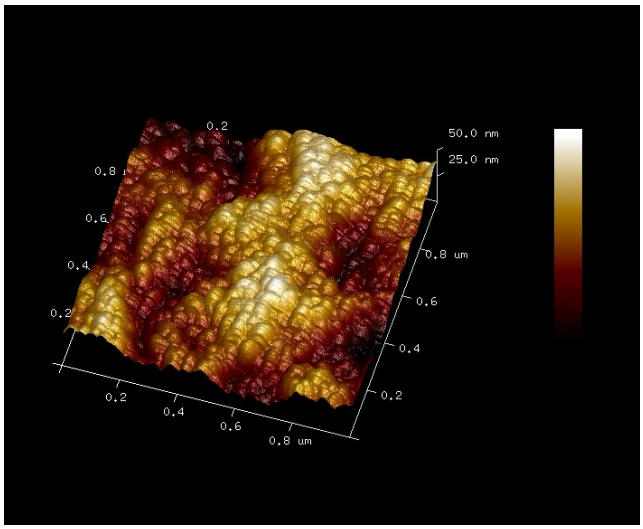


Figure 4.4 Surface morphology of a ZnO film from another similar sample, grown under the same conditions, obtained in tapping mode on a Bruker Dimension Edge AFM. Reproduced/adapted with permission from Ref. [33]; Copyright 2016 Electrochemical Society, Inc.

## 4.4 XRD characterization

The XRD profile, shown in figure 4.5, indicates the presence of diffraction peaks indexed to hexagonal wurtzite ZnO (PDF card 01-070-8070). The relative intensities of the three major peaks (100), (002), and (101) result from the fact that the electrodeposited film is relatively thin. It has been reported that, as the film grows thicker, the (002) diffraction peak becomes gradually more dominant [138]. Furthermore, the narrowness of all three major peaks indicates the formation of large crystallite sizes.

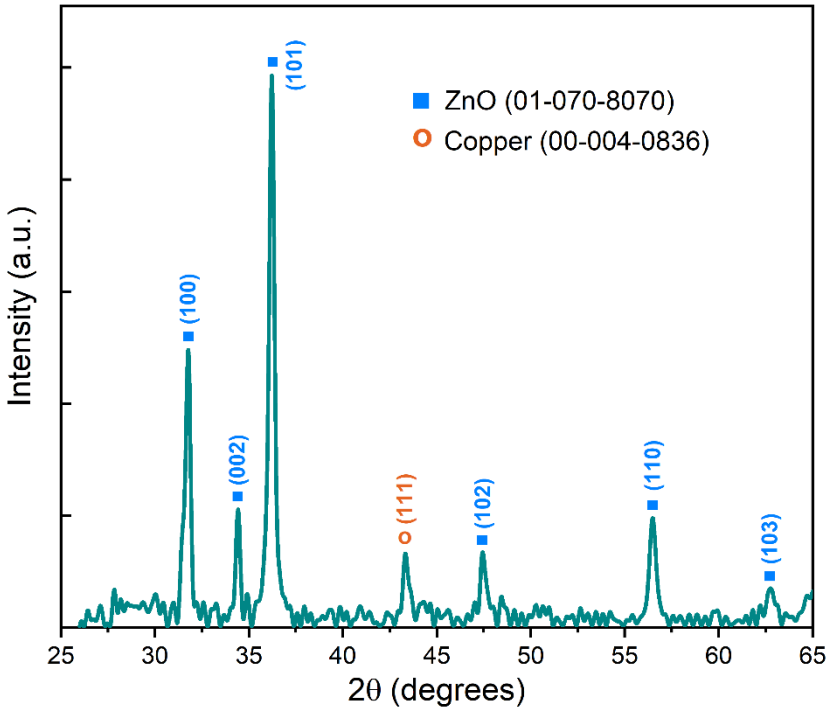


Figure 4.5 X-ray diffractogram of electrodeposited ZnO film (thickness ~ 120 nm) on Kapton/Ti/Cu flexible substrate. Reproduced/adapted with permission from Ref. [33]; Copyright 2016 Electrochemical Society, Inc.

## 4.5 Evolution of the crystallinity of columnar structures with thickness

Electrodeposited ZnO films have also been examined by the TEM selected-area electron diffraction (SAED) technique to analyze the evolution of the ZnO film crystallinity as it thickens. These ZnO films, intended for SAED purposes, have been electrodeposited under the same conditions but with a longer deposition time. The patterns have been obtained over wide areas from the bottom region of the electrodeposited film (near the bottom interface with copper) and from the top region of the same film (near the top surface). The resulting patterns are highly interesting and are shown in figures 4.6 and 4.7.

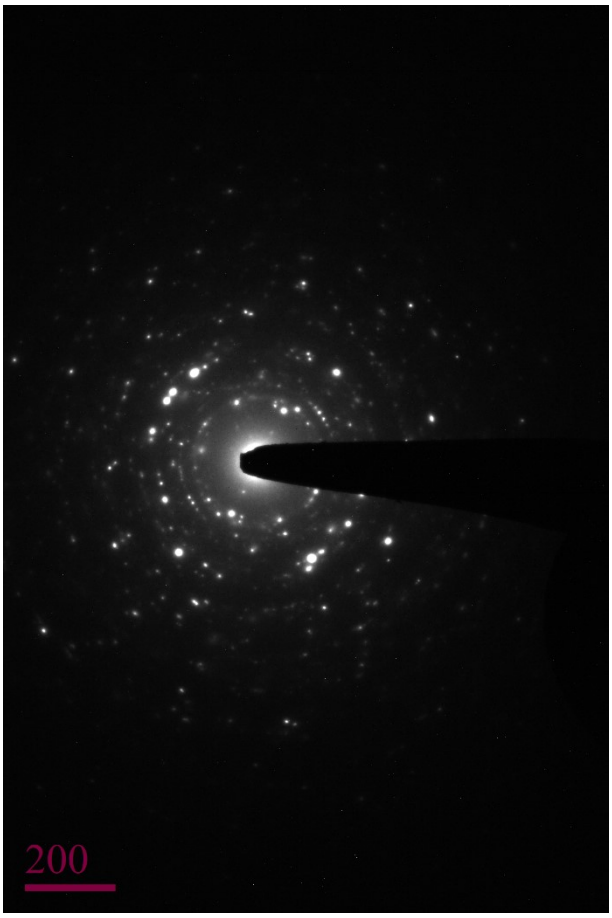


Figure 4.6 Selected-area electron diffraction pattern at the bottom region of the ZnO film (near interface). Reproduced/adapted with permission from Ref. [186]; Copyright 2019 American Chemical Society.

and,

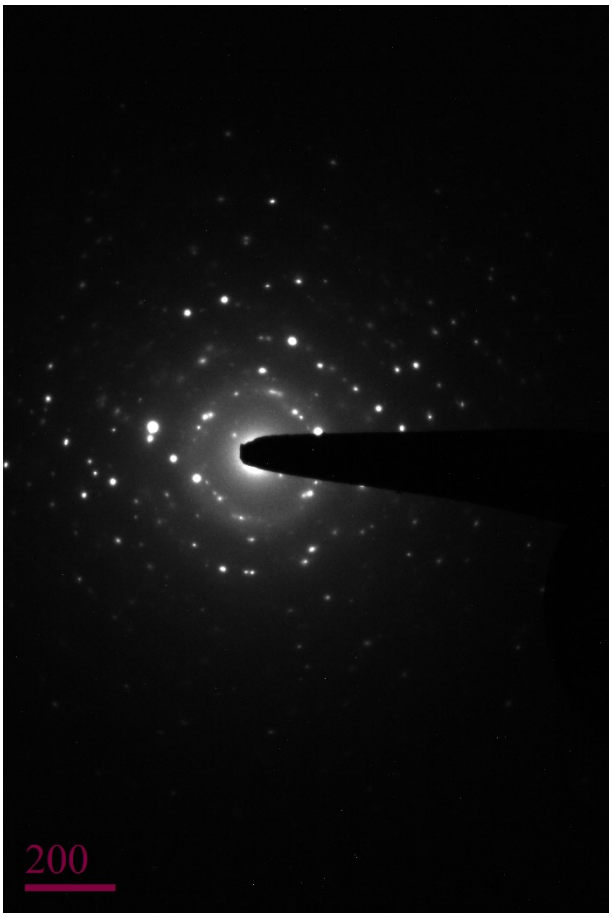


Figure 4.7 Selected-area electron diffraction pattern at the top region of the ZnO film (near surface). Reproduced/adapted with permission from Ref. [186]; Copyright 2019 American Chemical Society.

The pattern at the bottom of the film shows polycrystalline rings. The pattern then shifts from a ring pattern to a spot pattern as we move closer to the top surface. The spot pattern at the top of the film shows significantly enhanced crystallinity. This observation suggests that the crystallinity of the film is enhanced with increased thickness. Describing the development of the columnar structure, Paunovic et al. [139] state that it is composed

of relatively fine grains near the substrate, which then changes to the columnar structure with much coarser grains at greater distances from the substrate.

## 4.6 Current-voltage characteristics for different bending radii

The room temperature *I-V* characteristics were measured, for three values of bending radius $r$: $r = \infty$ (flat condition), $r =$ 4.445 cm (1.75 inch), and $r =$ 2.54 cm (1 inch). A photograph of the actual set-up during *I-V* testing of the bent sample is displayed in figure 4.8. The obtained *I-V* characteristics for the three bending configurations are plotted in figure 4.9. The extracted rectification ratios and ideality factors are summarized in table 4.1, together with the strain values derived from the relation: strain = $h_s/(2r)$, where $h_s$ is the substrate thickness [140].

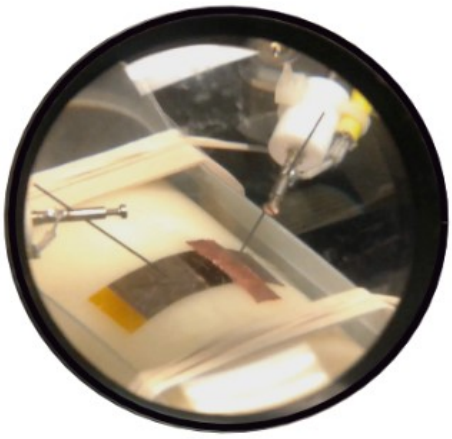

Figure 4.8 Photograph of the actual set-up during *I-V* testing of the bent sample on curved surface of known radius. Reproduced/adapted with permission from Ref. [33]; Copyright 2016 Electrochemical Society, Inc.

Under the flat condition, the extracted diode rectification ratio and ideality factor compare favorably with the current state-of-the-art for solution-processed ZnO films deposited on rigid substrates [126]. Moving from the flat condition to smaller bending radii, the *I-V* dependence changes with an ideality factor lying between 2 and 4. This change is accompanied by slight increases in reverse bias current. At high forward voltages, bending increases the diode overall series resistance and decreases the current. The combined effects of reverse bias current increase and forward bias current decrease with higher tensile bending lead necessarily to a reduction of the current rectification ratio. However, even at the smallest bending radius, the diode still exhibited rectification ratios higher than $10^3$ and ideality factors of ~ 3. Strain-induced defects due to tensile bending are possibly responsible for the Fermi level pinning, resulting in lower barrier heights and hence increased reverse bias current. The tensile bending also leads to structural material changes that affect the Richardson constant in the diode equation based on the thermionic emission model. Moreover, bending may cause Cu/ZnO contact inhomogeneities to have stronger effects on the barrier heights. Below the one-inch bending radius, rapid degradation of the *I-V* characteristics was observed. A gradual loss of mechanical stability is seen to result from the increased tensile bending of the Kapton/Ti/Cu/ZnO sample and from involuntary stretching that occurs during work on the samples.

Table 4.1 Schottky diode extracted parameters for different bending conditions.

| Bending radius *r* | Rectification ratio | Ideality factor | Strain (%) |
|---|---|---|---|
| ∞ (flat) | $1.1 \times 10^6$ | 2.72 | 0 |
| 4.445 cm (1.75 inch) | $1.1 \times 10^5$ | 2.27 | 0.056 |

| | | | |
|---|---|---|---|
| 2.54 cm (1 inch) | $2.5 \times 10^3$ | 3.15 | 0.100 |

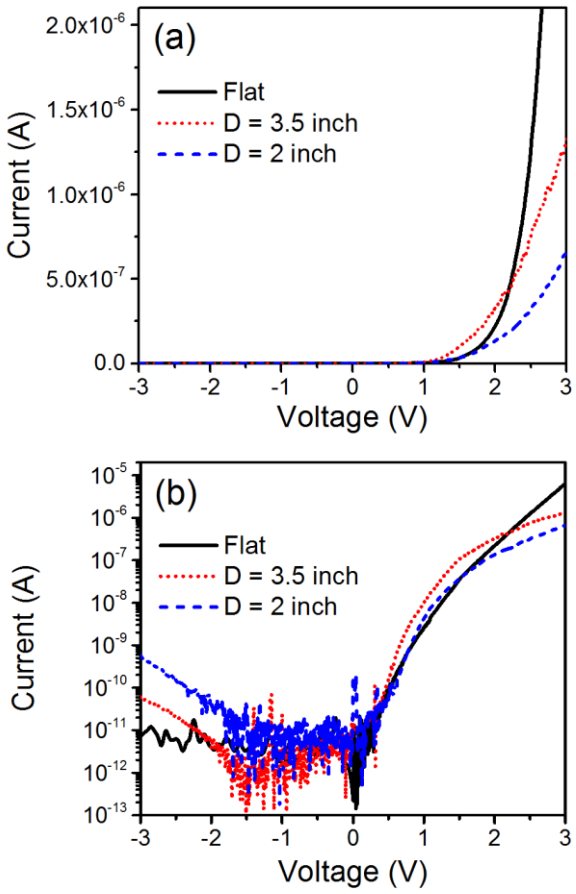


Figure 4.9 Cu/ZnO diode *I-V* characteristics measured at room temperature for three bending conditions and plotted in (a) linear and (b) semi-log scales. Reproduced/adapted with permission from Ref. [33]; Copyright 2016 Electrochemical Society, Inc.

## 4.7 Conclusion

By using a low-cost electrodeposition technique, we were able to grow a high-quality ZnO thin film optimized for electronic performance on a flexible substrate. Schottky

diodes made of the electrodeposited ZnO film and underlying copper contact on flexible Kapton substrate exhibited high rectification ratios (~ $10^6$) and low ideality factors (~ 2 to 3) that surpass the current state-of-the-art for solution-processed ZnO films. By performing bending tests, we demonstrated that the diodes have potential capabilities to retain device operationality with good performance under mechanical deformations. It is notable that the diode, which is formed by a relatively thick film (~ 120 nm) of inorganic semiconductor (ZnO), can retain operationality with good performance after substantial bending. These findings are promising and need further investigations. These systems could greatly benefit from the new implemented strategies in designing novel structures that make possible the use of inorganic materials on flexible platforms [141].

# Chapter 5

# 5 High Breakdown Strength Schottky Diodes Made from Electrodeposited ZnO for Power Electronics Applications

## 5.1 Introduction

Several researchers have studied wide band gap compound semiconductors with the aim of forming the optimal active layer for electronic devices to be used under severe electrical and environmental conditions [42, 142-144]. Semiconductor alternatives to silicon such as SiC, GaN, and diamond have been studied for decades and are in production for power electronic devices [145, 146]. ZnO is a comparable material to GaN in many aspects (band gap, saturation velocity, and thermal conductivity) and can be synthesized at much lower temperatures. In addition, ZnO is very resistant to radiation damage [35], amenable to low-temperature wet and dry chemical etching [147, 148] and offers the possibility of high-quality growth by the low-cost solution-processing techniques [149].

Preliminary insight into the suitability of a material for the fabrication of high-performance power devices could be seemingly gained by considering the Baliga's figure of merit (BFOM) [150]:

$$\text{BFOM} = \varepsilon_0 \varepsilon_s \mu_n E_c^3 \tag{5.1}$$

where $\varepsilon_0$ is the vacuum permittivity, $\varepsilon_s$ the dielectric constant, $\mu_n$ the electron mobility, and $E_c$ the critical electric field for breakdown. For ZnO, the critical electric field is a parameter that still continues to increase as material processing improves. In this work, we focus on assessing this critical field parameter for an electrodeposited zinc oxide film which features a columnar crystalline structure containing relatively defect-free crystallites. We recognize that this process has the potential to produce a low-cost, high-performance power diode for use in applications such as a full-wave rectifier in energy harvesting, a building block for extremely low-cost vertical power transistors, and power electronics on flexible substrates. To our knowledge, this is the first investigation of breakdown field strength in electrodeposited ZnO.

To achieve significantly high blocking voltage capability in ZnO-based devices, the ZnO grown layers and structures should exhibit (1) high electron mobilities, (2) sizable ZnO layer thicknesses, and (3) moderately low carrier concentrations. All of the above-mentioned material requirements can be potentially met by using the low-cost electrodeposition technique instead of the other known solution-processing methods, as we have already demonstrated in chapters 3 and 4. In the case of vertical power transistors, a collector drift region made of a thick and low-doped ZnO layer is where high electric fields occur, thereby enabling the device as a whole to withstand high voltages before breakdown.

In the present work, our objective is to optimize electrodeposited ZnO material to yield an enhanced reverse bias breakdown voltage in a Schottky diode by studying the multiple material growth conditions: precursor concentration, electrochemical potential, solution temperature, seed layer, and so on. We have opted to use vertical Pt/ZnO Schottky diodes as test vehicles to characterize the material properties. Therefore, by finding the best growth conditions to obtain the highest breakdown voltage in Pt/ZnO Schottky diodes, we can eventually apply those findings to other ZnO-based power devices such as vertical power transistors.

As will be shown afterwards, the FESEM investigation of the crystalline morphology of the electrodeposited ZnO films on Pt reveals a columnar ZnO film structure with highly crystalline grains. Vertical carrier transport along the columnar vertical crystallites benefits from mobility enhancement resulting from the low density of scattering centers and grain boundaries in the direction normal to the Pt substrate. This, in turn, should lead to a better BFOM. The deposition rates and deposited thicknesses on the Pt substrate depend on the combined growth conditions but are highly favorable when compared to vacuum-deposited films. Certainly, the possibility of achieving high thicknesses ultimately allows us to seek higher breakdown voltages.

One- and two-step deposition processes were carried out under similar growth conditions, where applicable, to investigate the effect of the metal-semiconductor interface on the expected high electric fields under large reverse bias in a Schottky diode configuration. This, in turn, directly impacts the breakdown voltages that a ZnO-based device can withstand. For these two deposition processes, the growth current-time

evolution in figure 5.1 shows different nucleation stage evolutions toward the growth stage. Comparatively, the two-step deposition process occurs more instantaneously.

## 5.2 Optimized growth of ZnO thin films by electrodeposition

### 5.2.1 Electrodeposition process

The device configuration is illustrated in figure 5.2. High work function platinum is used as the top substrate layer. The underlying wafer is a commercially supplied stack of thick thermal silicon oxide layer on n-type silicon. Formation of the Pt substrate layer was achieved in an electron-beam evaporation system by depositing a thin adhesive chromium (Cr) layer followed by a 40 nm thick Pt layer. The Pt-capped wafers were immediately saw-diced into samples whose size is compatible with our electrochemical cell dimensions. These samples were then stored under vacuum conditions to reduce platinum oxidation in open air. The low-cost cathodic electrodeposition method was employed to grow ZnO films on the evaporated Pt thin films. A simple electrolytic solution consisting of 100 mM zinc nitrate hexahydrate (99%, Sigma-Aldrich) dissolved in deionized water was prepared and stirred for 15 min. The solution pH was initially $5.3 \pm 0.2$. Prior to electrodeposition, the Pt substrate was ultrasonically rinsed in acetone and methanol and blow-dried. The electrodeposition process was carried out in potentiostatic mode using a standard three-electrode cell configuration in a glass beaker. A standard Ag/AgCl electrode (+200 mV vs SHE) was used as the reference electrode. A sputtered Pt film on glass and the pretreated Pt substrate were set up as the counter electrode and working

electrode, respectively. A computer-controlled CHI660E electrochemical workstation was used to control the applied potential and monitor the evolutions of current and charge over deposition time. One-step electrodeposition was conducted for 20 min at a fixed cathodic potential $E_V$ of -800 mV and a low solution temperature of 70 ± 2 °C with moderate stirring. The ZnO thin film obtained under these conditions is labeled F13A. The two-step electrodeposition, on the other hand, was carried out at the same temperature of 70 ± 2 °C with moderate stirring but with a sequence of two steps: fixed $E_V$ of -1120 mV for 10 s to form the seed layer, followed by a fixed $E_V$ of -800 mV for 20 min. The latter ZnO film is labeled F13B. As above-mentioned, the respective electrodeposition current-time recordings, shown in figure 5.1, reveal a more instantaneous nucleation mechanism for the two-step electrodeposition.

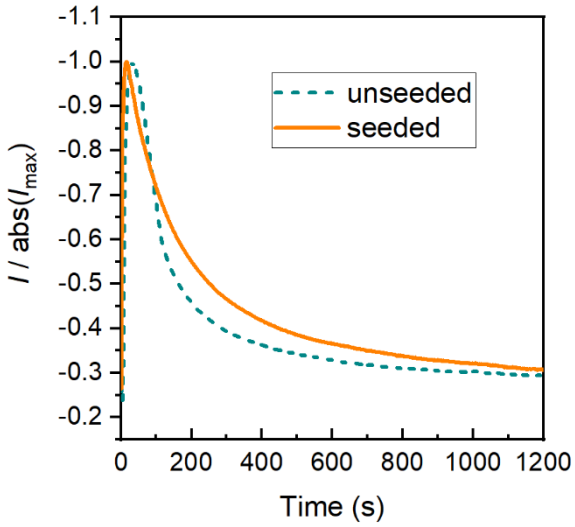


Figure 5.1 Variations of current (normalized to maximum current) versus time for the one-step (unseeded) and two-step (seeded) deposition processes of films F13A and F13B respectively.

Reproduced/adapted with permission from Ref. [186]; Copyright 2019 American Chemical Society.

### 5.2.2 Ohmic contacts formation

Through use of conventional lithography and metal lift-off processing, top circular ohmic contacts to the ZnO films were formed for the purpose of fabricating test Schottky diodes. They were made of electron-beam evaporated thin layers of aluminum capped with protective thin layers of gold. The final devices were ultimately obtained by using the Al/Au circular contacts as masks to wet-etch the open areas of ZnO down to the Pt surface with a commercially supplied Al etch. The devices present circular structures of 50 μm radii and the Pt layer acts as metal pad to the Pt/ZnO contact. A substantial advantage of such structure is that the Pt Schottky contact lies at the bottom thereby protecting Pt from exposure to air and oxidation along the current pathways. The electrical characterizations were performed by means of a Keithley 4200-SCS semiconductor parameter analyzer.

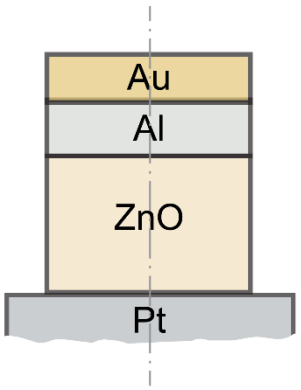


Figure 5.2 Cross-section of the top device configuration showing the lower Schottky contact (Pt) and the upper ohmic contact (Al/Au). Reproduced/adapted with permission from Ref. [186]; Copyright 2019 American Chemical Society.

### 5.2.3 Linear sweep voltammetry

The major reasons behind our choice of 100 mM zinc nitrate concentration, low deposition potential, and low deposition temperature can be summarized as follows: (1) this choice gives us the best ideality factor-breakdown voltage combination, and (2) lower deposition rates are expected to yield dense ZnO films with wider crystallite sizes [151]. The deposition potential lies at the low end of the potential range that yields ZnO synthesis, determined through linear sweep voltammetry results presented in figure 5.3. The obtained voltammogram indicates that cathodic current begins around -0.6 V. We found that the range between -0.75 V and -0.95 V is most suitable for the formation of ZnO films. The dotted line marks the cathodic potential applied for the ZnO electrodeposition presented in the main text. It has been generally observed that the total cathodic current consists of three components resulting from the reduction of nitrate, the formation of hydrogen gas, and the deposition of ZnO, respectively [152]. The detailed

optimization process that led to the choice of the unique set of growth conditions is presented in subsection 5.4.5.

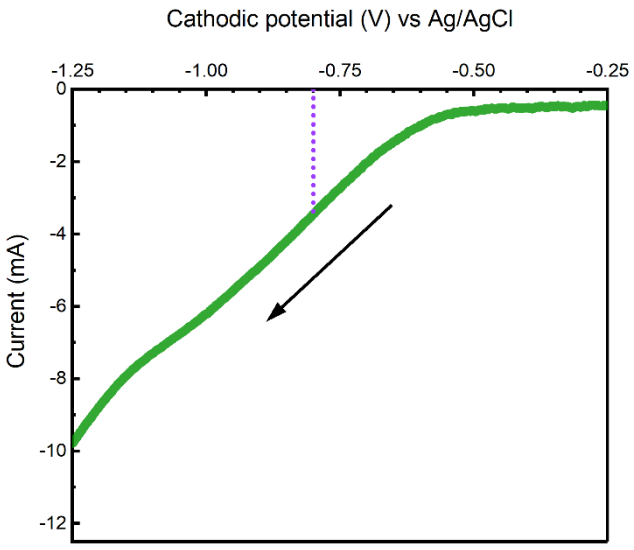


Figure 5.3 Linear sweep voltammogram of a platinum-coated cathode over the potential range -0.25 V to -1.25 V (versus Ag/AgCl) in 100 mM zinc nitrate hexahydrate solution at 70 ± 2 °C. Reproduced/adapted with permission from Ref. [186]; Copyright 2019 American Chemical Society.

## 5.3 Structural properties

### 5.3.1 XRD investigations

Both one- and two-step electrodeposited ZnO films F13A and F13B were subjected to XRD peak profiling. These films are profiled in figure 5.4. We observe that the peaks profiles of both types of films are highly similar, and hence the use of the seed layer did not markedly affect the crystalline texture under the present substrate and growth conditions. The peaks profiles reveal the presence of the three major diffraction peaks

(100), (002), and (101) of hexagonal wurtzite ZnO (PDF 01-089-1397). The narrowness of the peaks qualitatively suggests large crystallite sizes and minimal strain [102]. The (101) peak stands out as the most dominant.

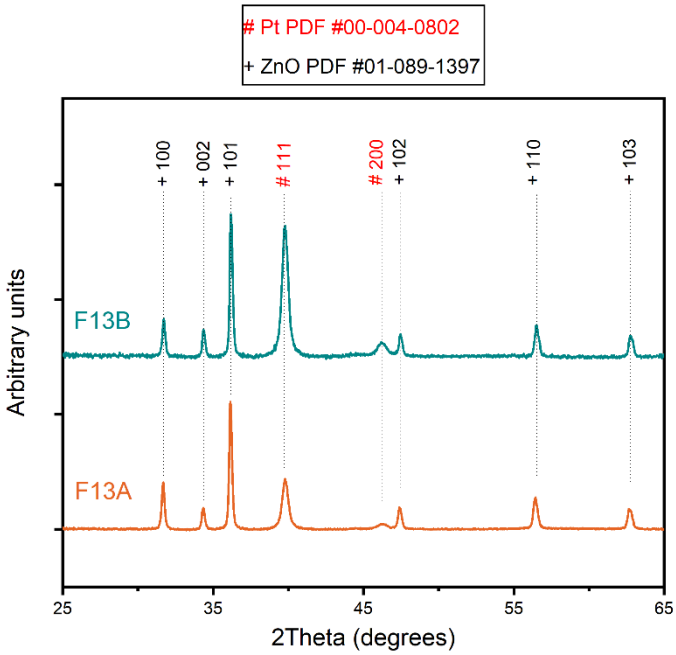


Figure 5.4 X-ray diffractogram of the electrodeposited ZnO films F13A and F13B.

We have also investigated the XRD profiles of two electrodeposited ZnO films F21A and F21B grown under different conditions than the previous films F13A and F13B.

Table 5.1 Growth conditions of ZnO films F21A and F21B.

| | **Film F21A** | **Film F21B** |
|---|---|---|
| **Electrodeposition sequence** | **One-step** | **Two-step** |
| **Zinc nitrate concentration** | 100 mM | 100 mM |

| | | |
|---|---|---|
| **Deposition temperature** | 76 °C | 76 °C |
| **Deposition potential and time** | -0.90 V for 20 min | -1.12 V for 10 s, followed by -0.90 V for 20 min |

F21B is the ZnO film which forms the semiconductor of the Schottky diode D21B. The obtained XRD profiles for these two films F21A and F21B are shown in figure 5.5.

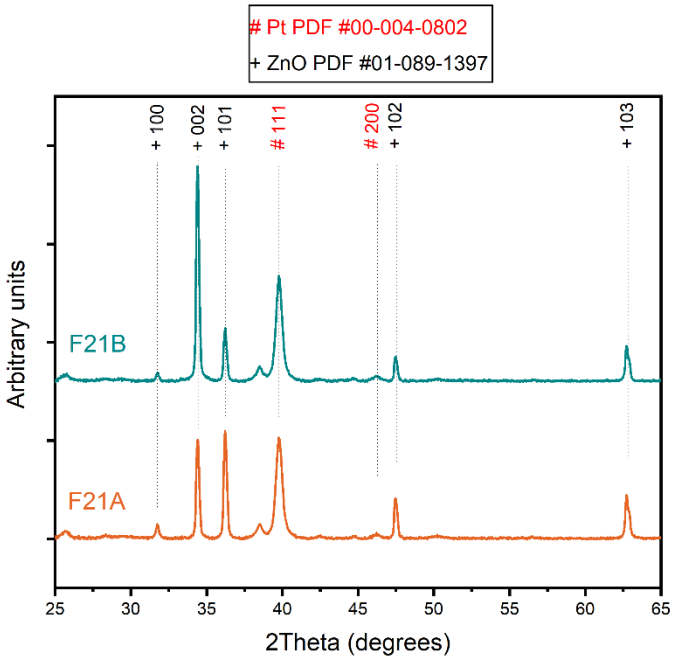


Figure 5.5 X-ray diffractogram of the electrodeposited ZnO films F21A and F21B.

Contrarily to the case of films F13A and F13B, we observe here that the presence of the seed layer resulted in the growth of a ZnO film with high preferential orientation along the (002) crystal direction. This result agrees with the work by Gao et al. [153]. We are thus led to conclude that the effect of the seed layer on crystal orientation is not systematic

but may depend on the seed layer deposition parameters and/or other growth conditions. It is also notable to observe the significant change of preferential orientation from (101) to (002) which has occurred from seeded film F13B to seeded film F21B as a result of small changes in potential and temperature.

### 5.3.2 Absorbance spectra

Absorbance spectra were measured by the spectrophotometry technique for sample n-Si/$SiO_2$/Cr/Pt/ZnO with ZnO film F13B. The wavelength range is between 250 nm and 700 nm. The electrodeposited ZnO film thickness is ~ 520 to 550 nm as measured by cross-sectional FESEM and capacitance-voltage technique. We observe a sharp absorption edge over a wavelength range characteristic of wurtzite ZnO. Beside the sharpness of the absorption edge, an excitonic absorption peak is clearly identified. The presence of the interference fringes indicate that the electrodeposited ZnO film is highly continuous and uniform. These absorbance characteristics further attest to the high crystalline quality of the electrodeposited ZnO film.

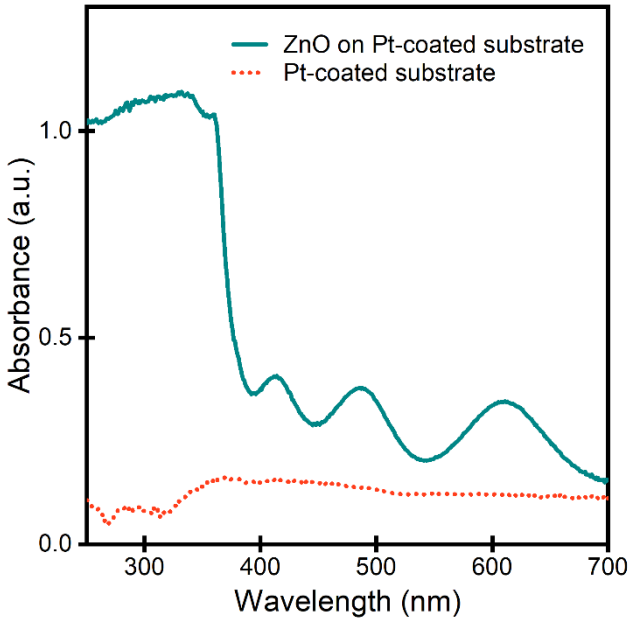


Figure 5.6 Absorbance spectra measured by the spectrophotometry technique on samples n-Si/$SiO_2$/Cr/Pt and n-Si/$SiO_2$/Cr/Pt/ZnO with ZnO film F13B. Reproduced/adapted with permission from Ref. [186]; Copyright 2019 American Chemical Society.

### 5.3.3 FESEM imaging

The cross-sectional morphology of a two-step electrodeposited ZnO film was further investigated by FESEM as depicted in figure 5.7. The film is coated with thin layers of aluminum and gold. The film thicknesses average around 550 nm roughly and thus agree, within the margins of uncertainties, with the thickness values extracted from the capacitance data in the subsequent text. The FESEM image reveals a dense film and columnar structures with crystallite widths tending toward 1 μm. Vertical carrier transport is particularly enhanced along these columnar structures because of the low scattering centers and grain boundary barriers along this direction. A deeper insight into the

evolution of the crystallinity of columnar structures with increased thickness has been presented in section 4.5.

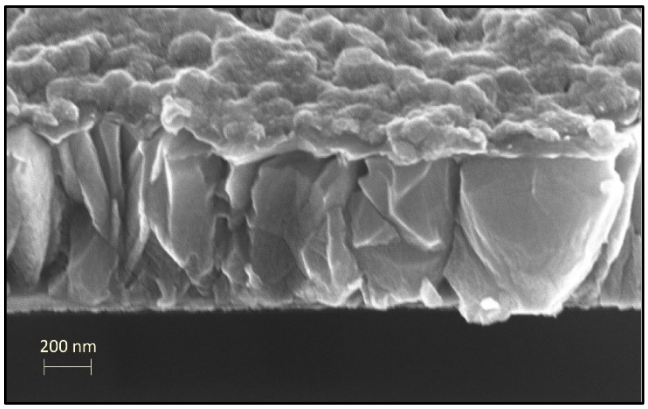


Figure 5.7 Cross-sectional FESEM image of the cleaved ZnO film F13B on Pt substrate. Reproduced/adapted with permission from Ref. [186]; Copyright 2019 American Chemical Society.

## 5.4 Electrical characterization

### 5.4.1 Current-voltage characterization and parameters extraction

Electrical conductivity and carrier concentration in ZnO films are strongly correlated to intrinsic defects and contamination impurities [4]. Their study gives insight into the films' crystalline and stoichiometric qualities. In this respect, the performance parameters of the fabricated test Schottky diodes were investigated through *I-V* and *C-V* measurements at room temperature. The charge transport through a Schottky diode can be described by a thermionic emission model featuring an ideality factor $\eta$ that incorporates all the nonideality factors [91]. As described in chapter 1, the *I-V* relation is given by equations (1.9) and (1.10). The top ohmic contact of the vertical diode has a circular

geometry with a radius of 50 μm. The *I-V* plots allow the extraction of $I_s$, $\eta$, $\Phi_B$, and $R_s$. In a semi-log scaled *I-V* plot, equation (1.9) corresponds to a linear region with linear fit $L(V) = (e/\eta k_B T)V + \ln(I_s)$ at forward bias voltages $V$ where $V > 3k_BT/e$ and $V >> R_sI$ concomitantly. The slope and intercept of the fit $L(V)$ readily allow the derivation of the ideality factor $\eta$ and reverse saturation current $I_s$, respectively: $\eta = (e/k_BT)\,(dL/dV)^{-1}$ and $I_s = \exp[L(V=0)]$.

Solution-processed ZnO exhibits, in general, much lower quality than vapor-deposited ZnO made under vacuum conditions [154, 155]. It suffers from higher densities of native defects and grain boundaries as well as higher levels of extrinsic contamination. The associated unintentional *n*-type doping is consistently reported to be higher than $10^{17}$ cm$^{-3}$ [109, 123]. As a consequence, Schottky barrier contacts formed to solution-processed ZnO have, in general, much lower quality with much higher ideality factors (~ 8-10) and leakier contacts (on-off ratio < $10^4$).

In figure 5.8, the measured room-temperature *I-V* characteristics of our fabricated Schottky diode D13B, based on the two-step electrodeposited ZnO F13B, are plotted in linear and semi-log scales. The linear-scaled plot shows the extent of the breakdown voltage. An excellent rectification ratio of ~ $3 \times 10^8$ is achieved in spite of nonoptimized Al/Au ohmic contacts. The reverse leakage current is kept relatively low with a reverse saturation current density of $1.8 \times 10^{-9}$ A cm$^{-2}$, which is favorably comparable to values obtained from Schottky contacts made of Pt on hydrothermally grown bulk ZnO [92]. The low leakage current is a first indicator that intrinsic defects in the ZnO film are either

reasonably low or electrically inactive for the most part. It also indicates that unintentional doping, due mainly to these intrinsic defects and extrinsic contamination, is relatively low.

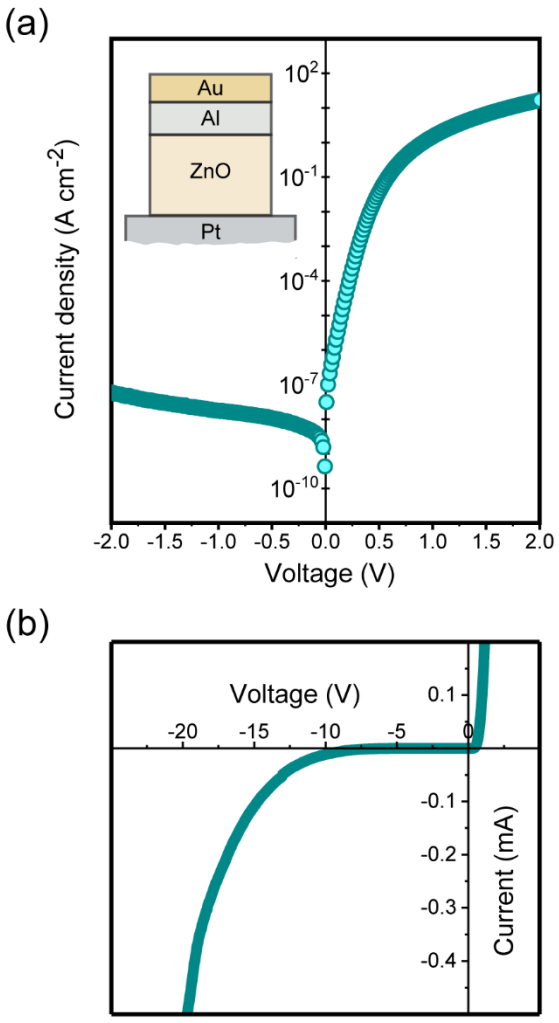


Figure 5.8 Diode current-voltage characteristics at room temperature of diode D13B with a circular contact of 50 μm radius. The inset in (a) shows the vertical Schottky diode structure. Plot (a) displays data in the semi-log scale, and plot (b) shows data in the linear scale until breakdown occurs. Reproduced/adapted with permission from Ref. [186]; Copyright 2019 American Chemical Society.

An ideality factor $\eta$ of 1.10 has been extracted. This consistently reproducible value of the ideality factor is outstanding for a solution-processed ZnO film and even for vapor-deposited ZnO films [90, 156]. It unequivocally attests to the high quality of the electrodeposited film. In addition, a turn-on voltage $V_{ON}$ of 0.91 V has been obtained at a forward current density of 1 A cm$^{-2}$ from figure 5.8(a) [157]. These extracted *I-V* parameters compare favorably with those obtained from Schottky contacts made on sputter-deposited amorphous gallium-indium-zinc oxide thin films [158].

### 5.4.2 Capacitance-voltage characterization and parameters extraction

The assumption of low doping can be verified by carrying out *C-V* measurements on the same test device to determine the free carrier concentration *N*. At a detection signal frequency of 100 kHz, the measured diode capacitance is given in figure 5.9 as a plot of $A^2/C^2$ vs $V$ which conveniently allows the determination of $N$ by applying Mott-Schottky theory. The slope of the linear fit is inversely proportional to $N$ expressed in equation (1.11). From data plotted in figure 5.9, we observe that the ZnO region reaches full depletion at a low reverse bias voltage of -0.45 V corresponding to the maximum value of $A^2/C^2$. For a circular electrode of 50 μm radius and assuming a dielectric constant $\varepsilon_s = 8.9$, we obtain a free carrier concentration $N \sim 2.5 \times 10^{15}$ cm$^{-3}$. The x-axis intercept of the linear fit gives a junction built-in potential $V_{bi}$ of 0.58 V, which is lower than $V_{ON}$ as expected. The free carrier concentration is lower even than those achieved in the highest quality ZnO crystals grown by advanced vapor-phase techniques [50, 159]. Only hydrothermally grown single crystals of bulk ZnO show lower carrier concentration

values, possibly due in part to the enhancing effect of lithium compensation [26]. Low carrier concentration and large depletion width are prerequisites to achieve high breakdown voltages. The low $N$ also results in a fully depleted ZnO region, under reverse bias voltages < -0.45 V, with a maximum depletion width $W_{max} = A\varepsilon_s\varepsilon_0/C \sim 520$ nm. The latter value is in close agreement with the average thickness of the ZnO film measured by cross-sectional FESEM.

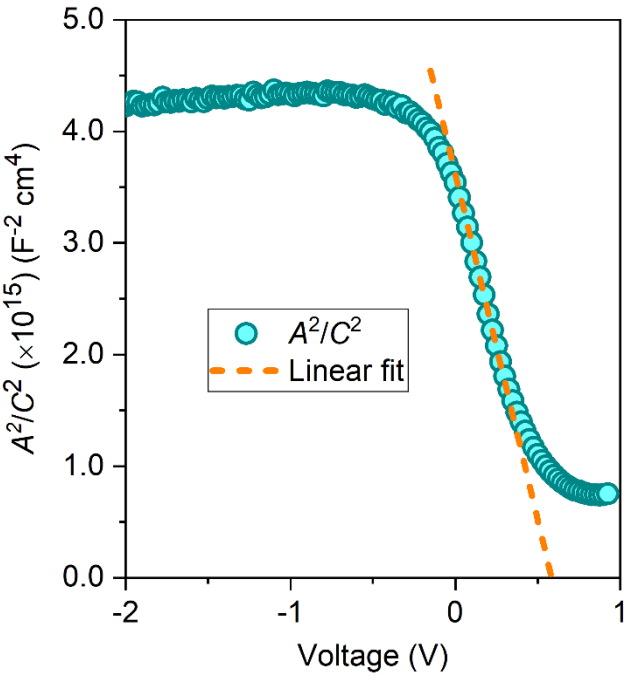


Figure 5.9 $C$-$V$ results from diode D13B plotted as $A^2/C^2$ versus $V$, where $A$ is the area of the circular top contact of the diode. Reproduced/adapted with permission from Ref. [186]; Copyright 2019 American Chemical Society.

### 5.4.3 Breakdown field strength measurements

The linear $I$-$V$ plot in figure 5.8(b) reveals a high breakdown voltage $V_{BD}$ of 20.75 V at room temperature, obtained on device D13B based on ZnO film F13B. The combined

values of the band gap, carrier concentration, and breakdown voltage suggest a breakdown mechanism resulting from the avalanche effect, but studies of the temperature effect on breakdown voltage are needed to ascertain the type(s) of breakdown mechanism. Knowing $W_{max}$, we can readily determine the critical electric field at breakdown $E_c$ by using the relation $E_c \approx 2V_{BD}/W_{max}$. The obtained $E_c$ corresponding to the present doping level is 800 kV $cm^{-1}$ and is 2–3 times higher than the value usually reported for silicon. No breakdown voltage enhancement technique such as passivation, field plate, ring guard, or other edge termination technologies was employed in these diodes. It is noteworthy that breakdown voltages as high as 33 V, for the same deposition time, have been obtained under slightly different growth conditions, as presented in the following.

### 5.4.4 Breakdown voltage dependence on electrodeposition times

We have grown ZnO films with the same growth conditions but with different electrodeposition times: 20 min and 10 min. The relevant growth conditions and extracted electrical parameters, including the respective breakdown voltages, are conveniently listed in table 5.2.

Table 5.2 Comparison between two devices of same growth conditions and different deposition times. Both ZnO films have been submitted to the same first electrodeposition step with a potential of -1.12 V for 10 s.

| | **Device 1 (= D21B)** | **Device 2** |
|---|---|---|
| Zinc nitrate concentration | 100 mM | 100 mM |
| Deposition temperature | 76 °C | 76 °C |
| Second step deposition potential | -0.90 V | -0.90 V |
| Second step deposition time | **20 min** | **10 min** |
| Thickness (by cross-sectional FESEM) | 1010 nm | 650 nm |
| Ideality factor | 1.17 | 1.24 |
| Free carrier concentration (by capacitance-voltage method) | $6.0 \times 10^{14}$ $cm^{-3}$ | $8.0 \times 10^{14}$ $cm^{-3}$ |
| Breakdown voltage | 33 V | 18.4 V |

The current-voltage plots showing the breakdown voltages for the above two Schottky diodes (Device 1 (D21B) and Device 2) are presented in figure 5.10.

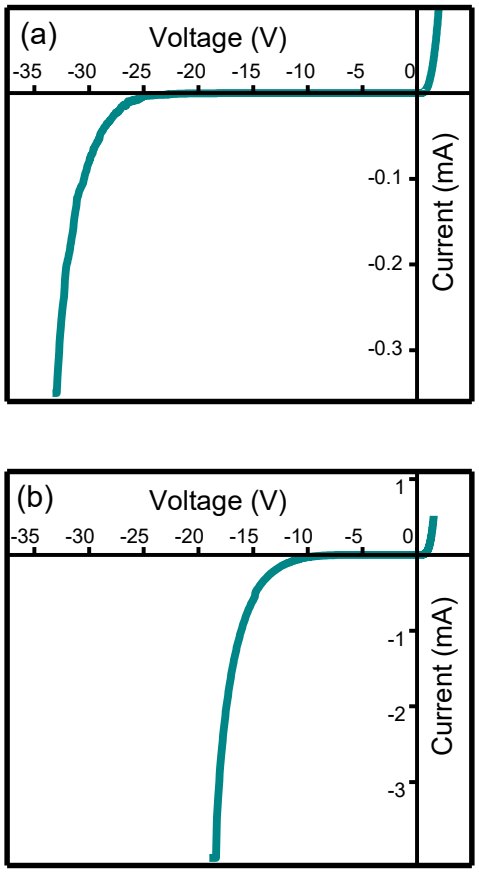


Figure 5.10 Plot (a) shows the breakdown voltage of Device 1 (D21B) while plot (b) shows the breakdown voltage of Device 2. Reproduced/adapted with permission from Ref. [186]; Copyright 2019 American Chemical Society.

We observe that the Schottky diode with the thicker ZnO film exhibits improved electrical parameters. Further studies are needed to investigate fully the relation between the electrodeposited ZnO film breakdown strength and its thickness.

### 5.4.5 Optimization of the growth process

In order to give further information about the optimization of the growth process in correlation with the breakdown field, we present in table 5.3 the results obtained from processing devices from six different samples grown at specifically selected growth conditions. A combination of two different temperatures $T$ and three different electrochemical potentials $E_V$ (derived from linear sweep voltammetry) has been applied for the two-step electrodeposition process. All samples have been submitted to the same first electrodeposition step with $E_V$ = -1.12 V for 10 s. The results include the breakdown voltages and the corresponding diode ideality factors $\eta$ and free carrier concentrations $N$. The data for $\eta$ and $N$ has been collected from four different devices on each of the six samples.

Table 5.3 Breakdown voltages and corresponding diode ideality factors and free carrier concentrations for six Schottky diodes made of ZnO films grown by two-step electrodeposition at different ($E_V$, $T$) combinations. The ideality factors $\eta$ and free carrier concentrations $N$ have been collected from four different devices on each sample and are reported with sets of three values in the form x (y, z) where x is the best value, y the arithmetic mean, and z the standard deviation. The zinc nitrate concentration is 100 mM and the second step deposition time is 1200 s for all ZnO films. The Dij labeling identifies devices with i the row number and j the column number. The electrical measurements were all carried out at room temperature.

| | **$E_V$ = -0.90 V** | **$E_V$ = -0.85 V** | **$E_V$ = -0.80 V** |
|---|---|---|---|
| **T = 70 °C** | D11B | D12B | **D13B** |
| | $\eta$ = 1.15 (1.33, 0.13) | 1.25 (1.42, 015) | **1.05 (1.09, 0.02)** |
| | $N$ ($cm^{-3}$) = $1.1\times10^{15}$ ($1.22\times10^{15}$, $0.10\times10^{15}$) | $3.70\times10^{15}$ ($5.38\times10^{15}$, $1.90\times10^{15}$) | **$2.60\times10^{15}$ ($4.16\times10^{15}$, $2.57\times10^{15}$)** |
| | $BV$ (V) = 27 | 22 | **20.75** |

| | D21B | D22B | D23B |
|---|---|---|---|
| **T = 76 °C** | $\eta$ = 1.18 (1.25, 0.07) | 1.20 (2.05, 0.57) | 1.19 (1.28, 0.15) |
| | $N$ ($cm^{-3}$) = $2.00\times10^{14}$ ($7.50\times10^{14}$, $4.43\times10^{14}$) | $1.20\times10^{16}$ ($3.05\times10^{16}$, $1.95\times10^{16}$) | $1.60\times10^{16}$ ($2.60\times10^{16}$, $0.96\times10^{16}$) |
| | $BV$ (V) = 33 | 22.5 | 16 |

We have also attempted the growth at $T$ = 82°C as well but the resulting films were of poor quality with inconsistent results in spite of extensive processing.

Devices D13B are the devices that have been focused on in this chapter because they exhibit the lower ideality factor and accurately follow the overall data trend. If we omit device D21B, we observe that the breakdown voltages are higher for lower temperature and more negative cathodic potential. This data trend is in very good agreement with the results reported by T. Shinagawa et al. [160] who have carried out Hall effect measurements on an electrodeposited ZnO film by transferring it from a conductive FTO substrate to insulative epoxy resin. They found that the free carrier concentration decreases with increasing deposition current density and decreasing deposition temperature. Therefore, the increase of our voltage breakdown trends in the same way as the decrease of their free carrier concentration. This correlation suggests that the voltage breakdown is highly dependent on the free carrier concentration, as we have expected.

## 5.5 Conclusion

We have demonstrated that electrodeposited ZnO can be a good candidate for low-cost electronic power device technologies. In addition to being simple and environment-friendly, ZnO electrodeposition presents distinct advantages to attain appealing breakdown performance. It has the capability to generate high film thicknesses at reasonably short deposition times and the possibility to achieve high electron mobilities along the structural columns which feature good crystalline order and low grain boundaries density. Test device processing involved the simple fabrication of a Schottky diode with no passivation, no edge effect reduction, no dry etch, and with only one standard lithography step. The device exhibited high electrical performance with an ideality factor of 1.10, a carrier concentration of $2.5 \times 10^{15}$ $cm^{-3}$, and a critical electric field of 800 kV $cm^{-1}$ which attest to the suitable quality of the ZnO film. The critical electric field has potential for future improvements with more optimized material and device processing techniques. Our results show that electrodeposited ZnO is an inexpensive and environment-friendly option for power electronic devices and energy-harvesting systems including full-wave bridge rectifiers and vertical power transistors.

# Chapter 6

# 6 Planar microwave resonator sensor with electrodeposited ZnO thin film for ultraviolet detection and carrier lifetime studies

## 6.1 Introduction

ZnO thin films and nanostructures exhibit a large dispersion in their electronic parameters depending on factors such as film morphology, stoichiometry, crystallinity, surface-bound species, and quality of hetero-interfaces in devices containing heterojunctions. Therefore, improved methods to characterize the optoelectronic properties of ZnO and other metal oxide semiconductors remain an enduring area of research and development.

Microwave resonators and sensors are well-studied and used in communication systems [161-166]. However, the microwave resonators with the planar configuration have recently gained a lot of interest for sensing applications due to their simplicity, low cost, low profile, long lifetime, non-contact sensing capability, and their compatibility with CMOS technology which facilitates mass production. These sensors can be used for material characterization [167-171], gas and liquid detection [172-174], and also for

biomedical diagnostic applications [175-177]. In addition, microwave sensors, in general, do not require special sample preparation.

In this regard, our group recently reported on the use of planar microwave resonators to measure the time-resolved microwave conductivity (TRMC) in bare and surface functionalized $TiO_2$ nanotube arrays [170, 178, 179]. For TRMC measurements, planar microwave resonators possess distinct advantages over cavity waveguide resonators such as CMOS integrability, compactness, clearly defined regions of maximum microwave amplitude, and high sensitivity to both photodielectric and photoconductive effects [178]. TRMC measurement in ring-type planar microwave resonators involves placing a free-standing membrane or film grown on a non-conductive substrate, of the material to be measured, in the coupling gap of the resonator where the microwave field is strongest. For thin films that cannot be delaminated from their underlying substrate, and also when the films can only be grown on conductive substrates as in electrodeposited films, an alternative measurement configuration is needed to capture the characterization benefits of planar microwave resonators. Keeping this in mind, we report on planar microwave resonators where the ZnO film to be characterized is directly electrodeposited on the conducting copper strip lines forming the resonator on a printed circuit board (PCB). Indeed, during electrodeposition, the ZnO film is deposited exclusively on the conducting copper strip lines and not on the nonconducting areas on the circuit board. The great advantage of this direct and selective electrodeposition on the conducting strip line is that no photolithography processing or other resource-intensive patterning method are needed, beyond the basic PCB circuit layout, to form the deposition pattern, thereby simplifying

greatly the overall fabrication process. This process optimization explains our choice of PCB-mounted planar microwave resonators for photoresponse characterization through TRMC measurement. More traditional methods of photodetection are based on employing devices such as the metal-semiconductor-metal photodetectors and measuring the photocurrent between the metal contacts with fixed bias voltage. By using the contactless TRMC method, a further process simplification is gained by eliminating the metal contacts deposition step. The TRMC method is based on the measurement of changes in microwave power with time when the sample is subjected to a short illumination [180]. Photogenerated charges in the semiconductor film can modify both the real and the imaginary parts of its permittivity depending on their mobility and degree of confinement [181]. The film complex conductivity σ relates to its complex permittivity $\varepsilon = \varepsilon' - i\varepsilon''$ as:

$$\sigma = i\omega\varepsilon = \varepsilon_0\omega\,(i\varepsilon' + \varepsilon'') \tag{6.1}$$

where $\omega$ is the angular frequency of a microwave electric field, $\varepsilon_0$ is the vacuum permittivity, and $\varepsilon'$ and $\varepsilon''$ are the real and imaginary parts of the permittivity respectively. Therefore, the imaginary part of the permittivity identifies microwave absorption whereas the real part is associated with polarization and is also responsible for a shift in the resonance frequency of the electric field. Both the real and imaginary parts of the electrical permittivity (and hence the complex conductivity) of the deposited film can be extracted by measuring two of the following characteristics of the microwave signal: amplitude, frequency, and quality factor [178]. These characteristics are readily extractable from the

S-parameters of the microwave resonator. For photoresponse measurements, we monitor the variations in resonance frequency $f_r$, resonance amplitude $A_r$, and quality factor $Q$ in response to UV illumination as a function of time.

TRMC offers other advantages over other techniques as well. In the case of direct current (DC) photoconductivity, the measurements suffer from charge transfer distortions at the metal-semiconductor interfaces through recombination, trapping, and back-injection. Another advantage is the capability of the TRMC method to explore the carrier dynamics and determine the carrier lifetimes and their decay mechanisms. In general, different optoelectronic properties can be exploited to realize carrier lifetime measurements, the most common being photoluminescence, photoconductance, and photovoltaic response. Many measurement techniques based on these concepts have been developed. TRMC has been used to characterize semiconductors such as silicon [182] and titanium oxide ($TiO_2$) [178] but no substantial TRMC studies have been reported on ZnO. The lifetime results in ZnO, available in the literature, pertain to photodetector structures with electrodes and show remarkable discrepancies ranging from few microseconds [183] to hours, thereby exhibiting the persistent photoconductivity (PPC) behavior [184].

As reported in chapters 3, 4 and 5, we have achieved the synthesis of electrodeposited ZnO films of high stoichiometric and crystalline quality on copper and platinum, which resulted in Schottky diodes that demonstrated superior transport and ideality factors [33, 185, 186], as compared to films prepared by conventional ZnO solution processing techniques [121], reported in chapter 2.

ZnO shows a tendency to exhibit strong PPC when illuminated by both supra-bandgap and sub-bandgap photons. There is strong fundamental interest in understanding the photoconductivity and PPC phenomena in ZnO due to 1) a range of interesting effects such as adsorption of $O_2$ and emission of $CO_2$ akin to the lungs of living creatures [187], the need for methods to control the PPC and resulting charge storage, and 2) the highly contested mechanism responsible for the PPC [184]. The PPC phenomenon enables ZnO-based thin films and nanostructures to be considered for charge storage applications but is undesirable in photodetectors due to the lengthening of response and relaxation times [188, 189].

In this work, a novel technique using planar microwave ring resonators coated with electrodeposited ZnO thin films is implemented to fabricate microwave sensors with detection capabilities to UV light irradiation. The UV detection sensitivity of the ZnO thin film is assessed through analysis of the S-parameters of the resonator sensor in the microwave frequency region. The effect of ambient humidity change on these photoresponse measurements is also experimentally examined.

## 6.2 Experimental procedures

### 6.2.1 Methodology

A planar microwave ring resonator is designed and simulated in HFSS (High Frequency Structure Simulator) software. The transmission parameter $S_{21}$ is studied for

various dielectric conditions (permittivity and conductivity) of a thin semiconducting layer of electrodeposited ZnO that conformally coats the top microstrip lines. The intimate contact of the ZnO layer with microstrip copper lines forms a Schottky contact with a space charge region at equilibrium, the width of which depends on the carrier concentration in ZnO, the relative permittivity, and the built-in potential. The ring microstrip resonator structure is presented in figure 6.1(a). The resonator is capacitively coupled to input and output microstrip lines. The microwave signal is injected from port 1, while port 2 is terminated to ground with a 50 Ω load during the simulation of the transmission parameter $S_{21}$.

The simulation results of the $S_{21}$ resonance profile of the bare (no ZnO film) microstrip resonator are presented in figure 6.1(b). They demonstrate a resonance frequency of 6.2 GHz and a quality factor of 170 with a resonance amplitude of -8 dB. Electric field analysis at the resonance frequency demonstrates the intensive electric field on the resonator's microstrip gap, while the magnetic current simulation distribution presents the intensity of the magnetic current in specific regions of the resonator's microstrip line (figures 6.1(c) and 6.1(d)).

The introduction of the semiconducting ZnO layer in the immediate vicinity of the microwave resonator alters the electromagnetic fields in that region and therefore results in the variation of the effective permittivity representing the combined permittivity values associated with all the materials forming the resonator sensor multi-media system. Moreover, as discussed previously, the TRMC method is based on the temporal variations of the resonator's complex permittivity (and therefore complex conductivity). Indeed, the

microwave resonator's photoresponse is a measure of the variation of the complex permittivity as a function of time when subjected to a short UV illumination. As will be discussed later, the variations of the complex permittivity are physically caused by multiple photogenerated carrier processes. Thus, to represent the permittivity variations due to UV illumination for simulation purposes, we assign hypothetical values and changes to the permittivity $\varepsilon = \varepsilon' - i\varepsilon''$ through the traditionally employed input parameters: dielectric constant $\varepsilon_r = \varepsilon'/\varepsilon_0$ and loss tangent (tan δ).

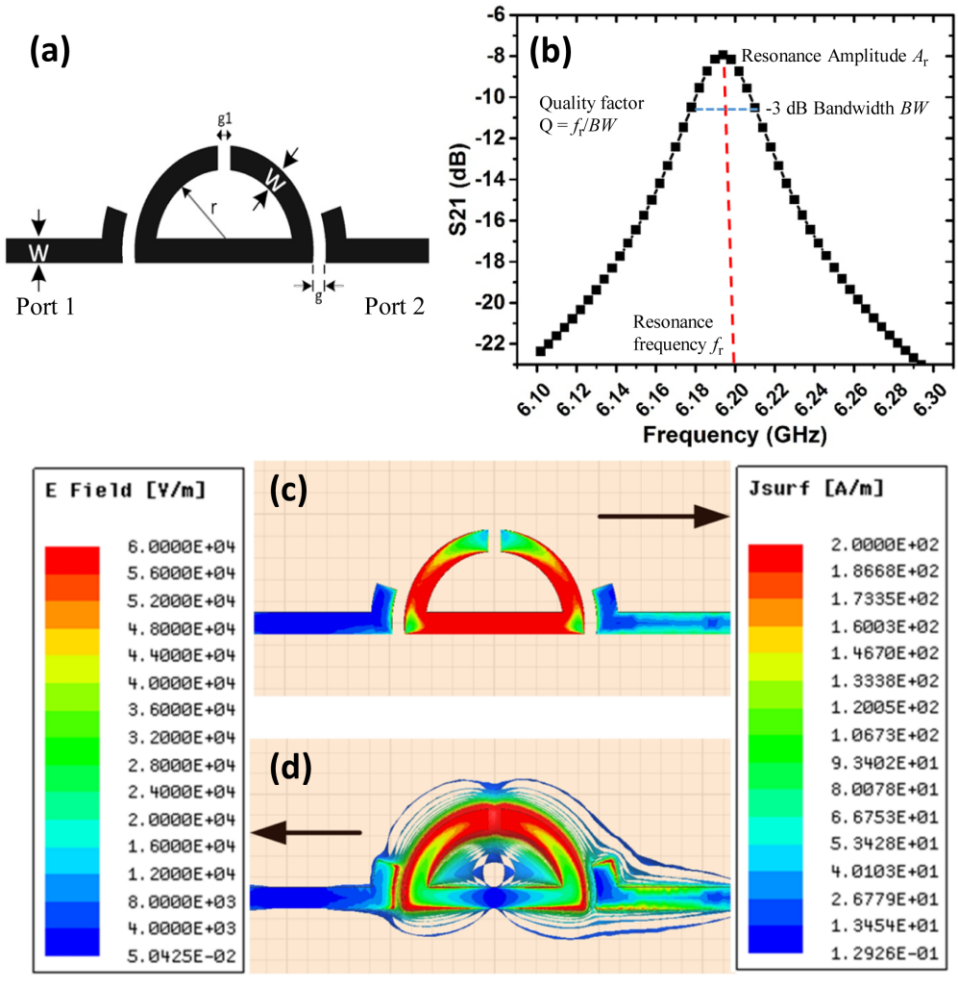


Figure 6.1 (a) Curved ring resonator implemented in HFSS software, W = 1 mm, g = 0.6 mm, $g_1$ = 0.6 mm, r = 2.8 mm, (b) simulated $S_{21}$ resonance profile with resonance frequency and quality

factor of 6.2 GHz and 170, respectively, (c) magnetic current distribution on the resonator's microstrip lines, and (d) electric field simulation on the resonator's substrate.

To study the effect of the ZnO thin film electrodeposition on the electrical parameters of the resonator, a model was implemented in HFSS software and simulated using the finite element method. Figure 6.2 presents the implemented structure and the simulation results for the $S_{21}$ resonance profile for varying electrical parameters (dielectric constant, loss tangent) of the ZnO thin layer. The dielectric constant of the ZnO thin film was assumed to be 8.9 [190]. Firstly, figure 6.2(a) demonstrates that both the resonance frequency and the resonance amplitude are significantly affected by the presence of the electrodeposited ZnO film. The ZnO film creates excess regions of higher dielectric constants and finite conductivities in the immediate vicinity of the resonator, which result in these changes of the transmitted microwave energy. It should be noted that the ZnO electrodeposition effect on the microstrip's gap capacitance should be relatively weak. Secondly, the simulation in figure 6.2(b) shows the $S_{21}$ results for varying input values of the dielectric constant and tangent loss of a ZnO layer of 4.7 μm thickness. The corresponding resonance frequencies $f_r$ and resonance amplitudes $A_r$ are given in table 6.1.

Table 6.1 Resonance frequencies $f_r$ and resonance amplitudes $A_r$ which correspond to the $S_{21}$ simulation plots of figure 6.2(b).

| $\varepsilon_r$ | tan δ | $f_r$ (GHz) | $A_r$ (dB) |
|---|---|---|---|
| 8.9 | 0.01 | 6.169400 | -7.517 |
| 11 | 0.01 | 6.168790 | -7.525 |
| 11 | 0.5 | 6.168670 | -9.674 |

It is observed that an increase of $\varepsilon_r$ from 8.9 to 11 with a constant tan δ of 0.01 leads mainly to a frequency downshift. On the other hand, an increase of tan δ from 0.01 to 0.5 with a constant $\varepsilon_r$ of 11 leads mainly to an amplitude decrease with relatively minor frequency variation. The space charge region at the copper/ZnO interface has not been considered in this simulation. The observed resonance frequency downshift can therefore be mostly attributed to the variations of the resonator's effective dielectric constant. The capability of this experimental method to selectively detect the variations to the probing microwave signal caused by changes in the resonator's dielectric environment leads us therefore to conclude that such method could be effectively used to characterize the electrical properties of the ZnO thin film.

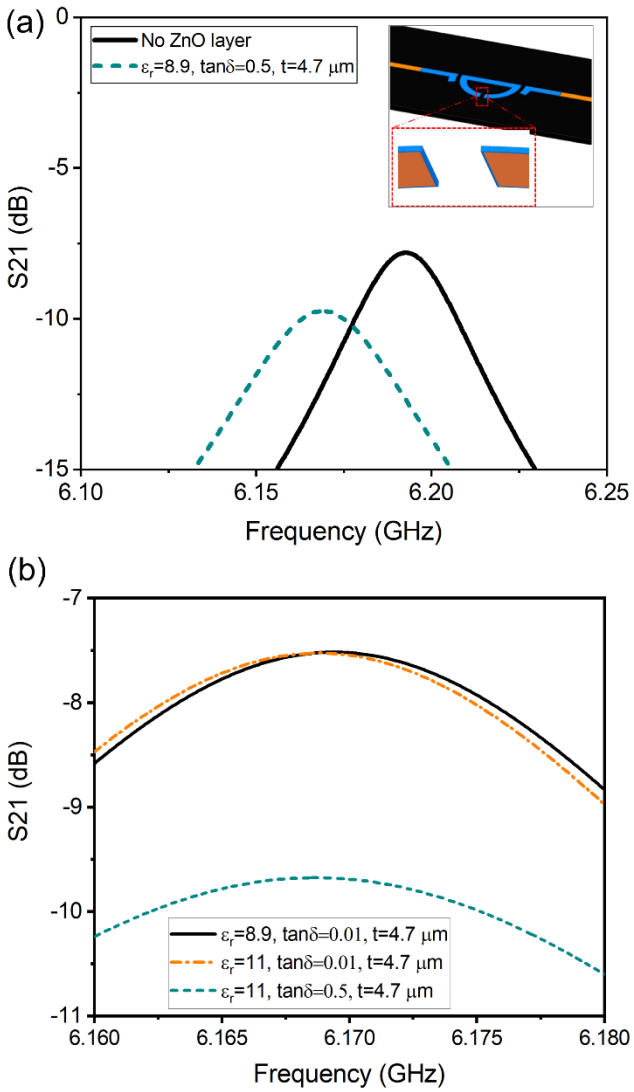


Figure 6.2. (a) Simulation results show the frequency downshift after ZnO film electrodeposition. The inset illustrates the simulated structure in HFSS software with a layer representing ZnO (blue color) on the copper microstrips (orange color). (b) the simulation results for varying values of the dielectric constant and tangent loss of a ZnO layer of 4.7 μm thickness.

### 6.2.2 Fabrication

The growth of the ZnO thin film by electrodeposition presents significant advantages. Firstly, electrodeposition is a low-cost and simple solution technique with potential to

grow high quality ZnO films at low temperatures. Secondly, the fabricated resonator copper structure readily forms a selective conductive pattern for ZnO electrodeposition. No complex photolithographical pattern alignment steps are therefore needed between the copper understructure and the ZnO film coating it. This seamless and simple fabrication process is achievable with minimal time and costs.

The planar microwave resonator sensor, shown in figure 6.3(a), was implemented on a microwave substrate, from Rogers Corporation, with the following specifications: dielectric constant = 2.2, loss factor = 0.00009, thickness of the dielectric material = 0.79 mm, and thickness of copper layer (covering both sides of the substrate) = 35 μm. A PCB processing technique using wet chemical etching was applied to implement the microwave resonator, illustrated in figure 6.1(a).

Cathodic electrodeposition was employed to grow thick ZnO films on the fabricated resonator copper structures. The electrolytic solution consisted of 100 mM zinc nitrate hexahydrate (99%, Sigma-Aldrich) dissolved in deionized water. The initial solution pH was $5.2 \pm 0.2$. The deposition mechanism of ZnO film from the zinc nitrate $Zn(NO_3)_2$ precursor in aqueous solution has been described in detail in a previous work [185]. Prior to ZnO electrodeposition, the rough surface of the fabricated resonator copper structure was rinsed in acetone and methanol and subjected to a soft oxygen plasma treatment of 10 s duration. The purpose of this treatment is to achieve good adhesion at the copper/ZnO interface through contamination removal and surface activation. The electrodeposition process was carried out potentiostatically using a standard three-electrode cell configuration in a glass beaker. The reference electrode was a standard Ag/AgCl electrode

(+200 mV versus SHE, the standard hydrogen electrode). A sputtered platinum film and the pretreated resonator copper structure were set up as counter electrode and working electrode respectively. Electrodeposition cannot be performed on the as-fabricated resonator copper structure because the two feed lines and ring are spatially separated by the two coupling gaps which do not allow current flow to all parts of the copper structure. To this effect, two connecting thin wires were placed by soldering between each feed line and the ring respectively. A computer-controlled CHI660E electrochemical workstation was employed to apply potential and record current-time and charge-time data. The electrodeposition was performed for 17.5 min at a fixed cathodic potential $E_V$ of -875 mV and a solution temperature of 80 ± 2 °C with moderate stirring.

### 6.2.3 Film characterization

FESEM was performed on a Hitachi S-4800 instrument to image the surface and cross-sectional morphologies of the electrodeposited ZnO films. The FESEM image, shown in figure 6.3(b), reveals a fully continuous ZnO film with large grain sizes and columnar crystalline structure. The ZnO film thickness is estimated to be 4700 ± 50 nm. XRD peak patterns were also collected with a Bruker D8 Discover diffractometer at a Cu-Kα line of 1.54059 Å. The XRD peak pattern displayed in figure 6.4 can be indexed to the Miller planes of hexagonal wurtzite ZnO (PDF card 01-089-1397). The narrowness of the diffraction peaks further attests to the large grain sizes nature in the ZnO thin film.

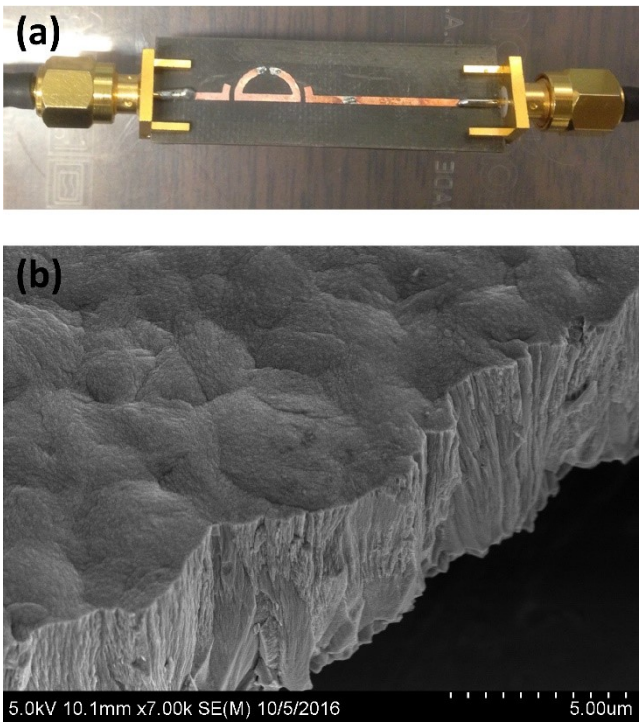


Figure 6.3. (a) The fabricated microwave resonator sensor, (b) FESEM images of the surface and cross-sectional morphologies of electrodeposited ZnO films on copper understructure.

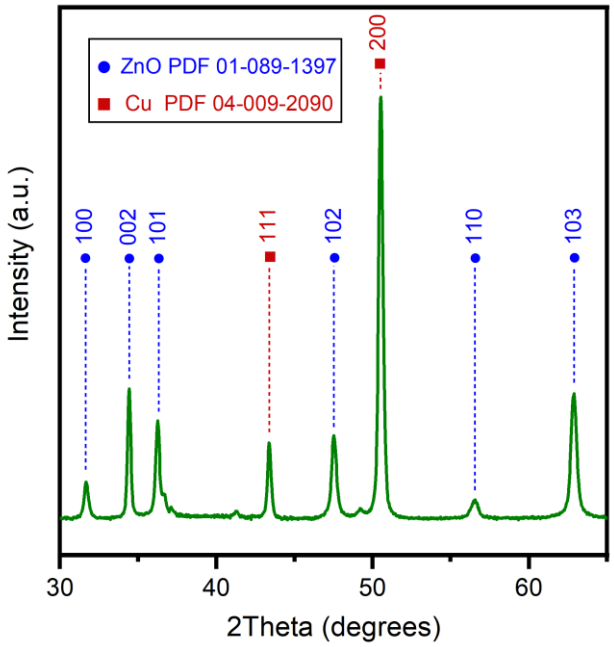


Figure 6.4. XRD peaks profile of the same electrodeposited ZnO film on copper understructure. The square symbol refers to the Cu material.

A thickness of $4700 \pm 50$ nm of ZnO thin film, as measured by cross-sectional FESEM, has been electrodeposited on the copper lines of the ring resonator. The backside copper metallization, forming the ground plane, was protected during the ZnO electrodeposition process. A UV curing lamp with 254 nm center-wavelength was utilized to illuminate the ZnO film during the experiment. A PXI vector network analyzer equipped with LabView software was used to automatically measure and record the S-parameters of the microwave structure. The data sampling was performed every 10 s over the frequency span of 6.15 to 6.35 GHz, with intermediate frequency bandwidth of 1 kHz and 2001 frequency sampling points. Figure 6.5 shows the measurement setup for this test. The resonator with ZnO thin film was placed inside a dark-box to isolate and suppress

the effect of the ambient light at the room temperature (23 °C) with the relative humidity of 25%.

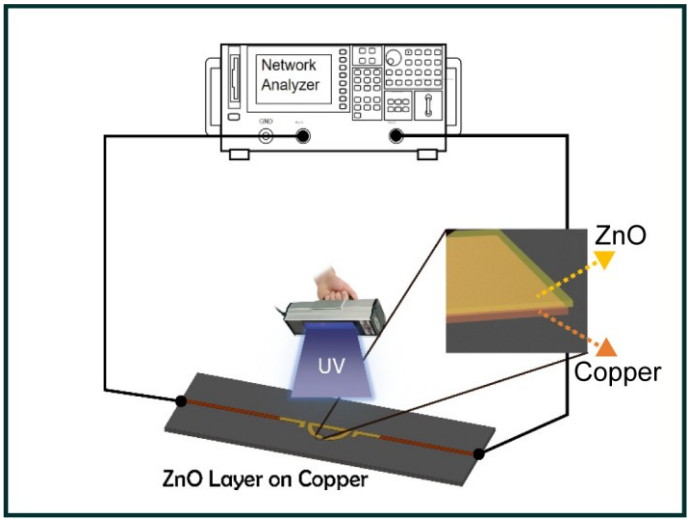


Figure 6.5. Schematic of the experimental setup. A UV lamp with wavelength of 254 nm was placed at a distance of 20 cm from the resonator.

Further studies were carried out to examine the effects of changing humidity levels on the photosensing reliability of the resonator sensor. To this effect, an experimental setup was prepared using dry air as the reference carrier gas, a bubbler as the source of humidity and two mass flow controllers (MFC) to dilute the humid air with dry air to create different humidity levels inside a sealed chamber. Figure 6.6 displays the experimental setup. A temperature/humidity sensor was placed inside the chamber along with the microwave sensor to monitor the relative humidity and the temperature as an independent reference.

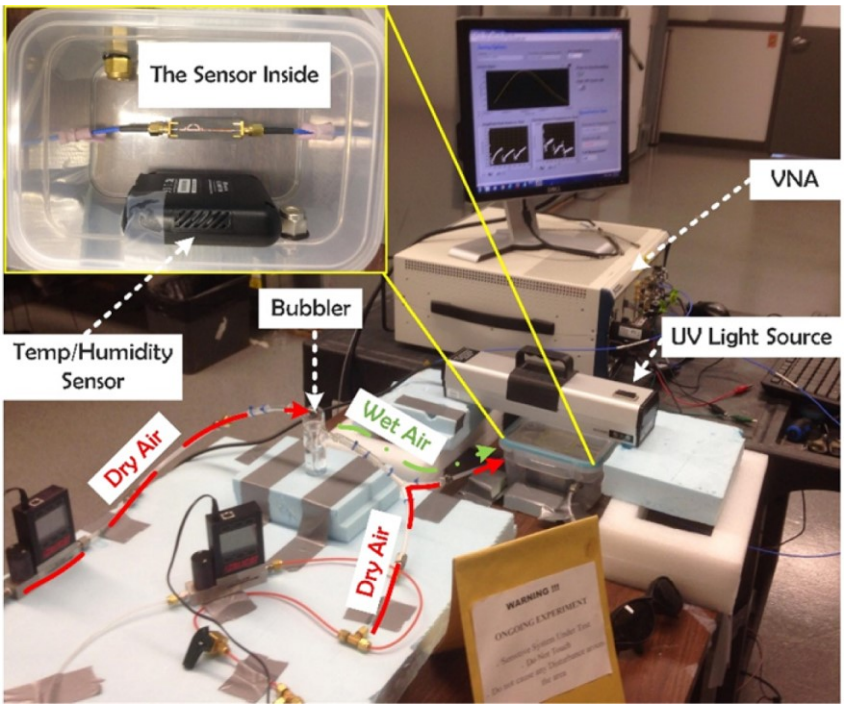


Figure 6.6 Experimental setup to study the effect of relative humidity on the response of the ZnO coating during the illumination and relaxation periods.

## 6.3 Results and Discussion

### 6.3.1 Photoresponse measurement studies

The experimental $S_{21}$ parameters of the resonator, before and after the ZnO film electrodeposition, are presented in figure 6.7. It is observed that the resulting alteration of the effective permittivity of the microwave resonator causes downshift of the resonance frequency and decrease of the resonance amplitude. The respective quality factors computed from the data in figure 6.7 are 119 and 118 for the bare and ZnO-coated resonators.

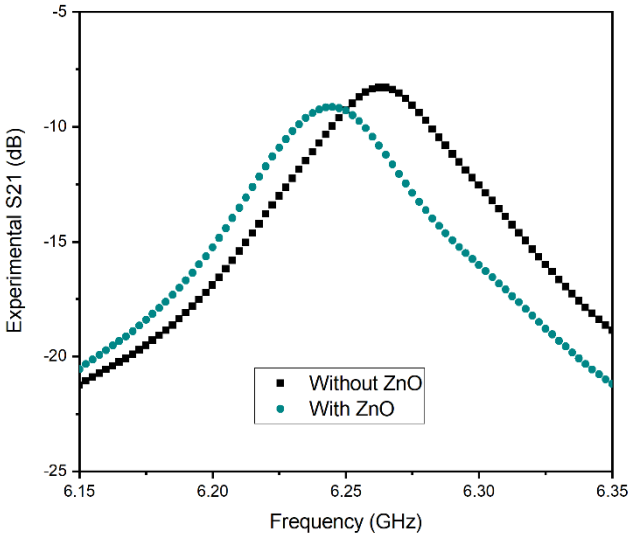


Figure 6.7 The experimental $S_{21}$ parameters of the resonator, before and after the ZnO film electrodeposition, respectively.

The transient responses of the resonance frequency of the resonator sensor were extracted from the measured $S_{21}$ resonance profile. Upon exposure to the UV illumination, the resonance frequency shifted downward and exhibited a significant downshift of ~ 6 MHz after an illumination time of 200 s. After the UV illumination is switched off, the profiles return back to their initial states after a time period of 900 s, as demonstrated by the transient responses in figure 6.8. The resonator sensor thus exhibits good sensitivity to UV light within a short exposure time of less than 3 min. While the transient photoresponses are fundamentally manifestations of band-to-band electron-hole pair generation-recombination upon UV light absorption, they are still strongly dependent on multiple other processes that could include: 1) trapping, detrapping, and recombination of photogenerated carriers by defect centers, 2) photoionization of oxygen vacancies [184], 3) adsorption and photodesorption of ambient oxygen and water on the surface and grain

boundaries exposed to UV light, and 4) other processes. These processes contribute with varying weights to the observed relaxation to the initial state. It should be noted that the UV penetration depth in ZnO is less than 100 nm, whereas the thickness of our ZnO film is close to 5 μm. Therefore, only thin surface layers contribute to the UV photoresponse. The thickness of the ZnO film is still relevant because the grain boundaries density and the bulk defects density within the UV-penetrated regions of the ZnO film depend on it, as demonstrated in chapter 4 [186].

We know that the electrical conductivity of the ZnO film rises when exposed to UV light. However, based on the hypothetical input values used, our microwave simulations have revealed that changes in tangent loss do not shift the resonance frequency of the microwave resonator in any consequential way. On the other hand, the simulations show that the resonance frequency downshifts when the dielectric constant $\varepsilon_r = \varepsilon'/\varepsilon_0$ of the coating film increases. An increase in the dielectric constant of the coating film would lead to an increase of the effective dielectric constant of the resonator system which, in turn, results in the observed downshift of the resonance frequency. Therefore, based on the simulation results, we conclude that the resonance frequency downshift, which has been measured experimentally, could result in a large part from the changes of the dielectric constant of the ZnO film in response to UV illumination. Admittedly, photoexcitation and relaxation processes, some of which were listed earlier, are responsible for the changes of the dielectric constant. Indeed, they involve the creation of bound charges which alter the polarizability of the ZnO material and hence its dielectric constant in accordance with the principle of the photodielectric effect [178]. In this

respect, it should be emphasized again that the photoconductive effect has been predicted by simulations to not have a consequent influence on the resonance frequency shift of the transmitted microwave signal.

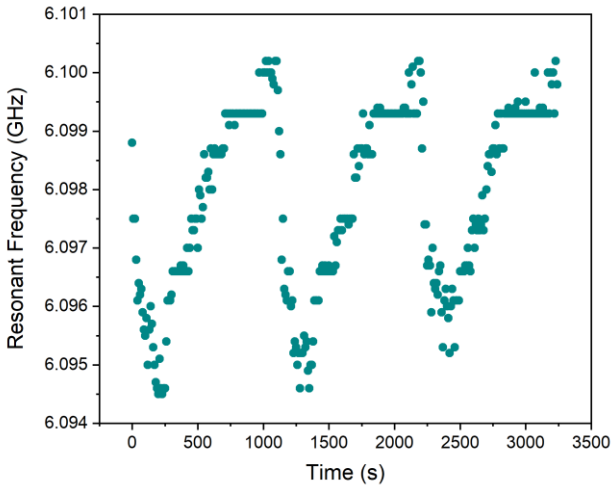


Figure 6.8 Resonance frequency variation with time for an illumination time of 200 s and a relaxation time of 900 s for three consecutive cycles. Starting data point at the onset of the first cycle is not shown.

### 6.3.2 Impact of humidity on sensor performance

It is of interest to study the excitation and relaxation curves of the transient photoresponse with their time constants at different humidity levels. Note that the relaxation time corresponds to the lifetime of photogenerated carriers. ZnO is widely recognized for its humidity sensing properties [191] and, therefore, our ZnO-based UV sensor performance is expected to depend on the ambient relative humidity (RH) levels.

The experimental setup for humidity study has been described in the experimental section 6.2. The transient photoresponse of the resonance amplitude of the transmitted

microwave signal was studied at different humidity levels. Figure 6.9(a) shows the measured results at 20% RH whereas figure 6.9(b) presents the same experiment with identical parameters at 70% RH. The UV-light was illuminated for 2 min ($T_i$) and the sample was relaxed for 6 min ($T_r$) for three consecutive cycles of UV light exposure/switch off.

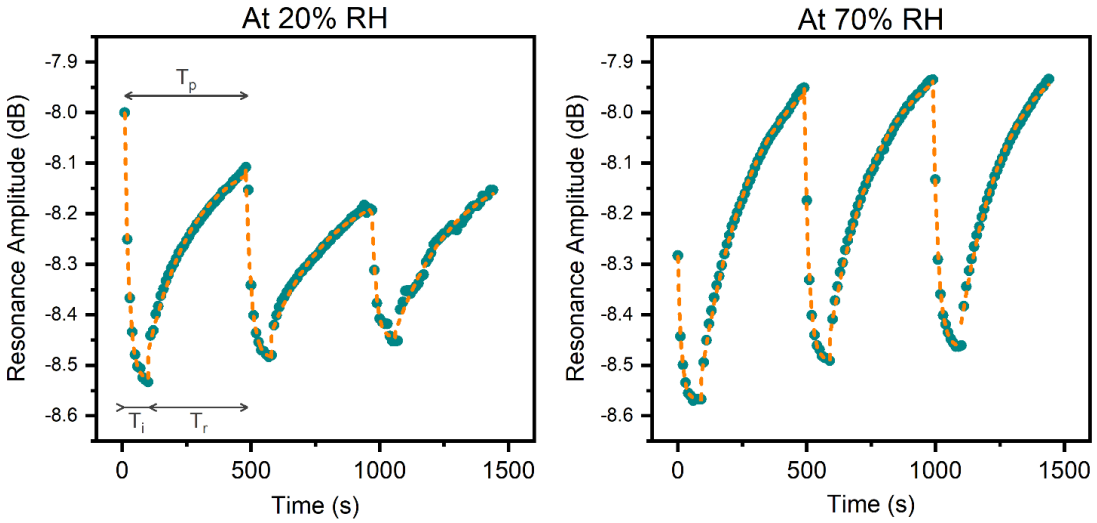


Figure 6.9 Resonance amplitude study during UV illumination and relaxation for three consecutive cycles at two RH levels: (a) RH = 20%, (b) RH = 70%. The curves could be fitted by a one-phase exponential decay function (dashed line).

During the 6 min relaxation times, the signal amplitude recoveries are much faster at 70% RH. As discussed earlier, the photoresponse processes at low RH include band-to-band electron-hole generation-recombination, defect-related traps and recombination centers, oxygen vacancies photoionization, and oxygen molecules adsorption/desorption on the surface and grain boundaries. Additionally, under the high RH condition, the role played by water vapor becomes important. The transient relaxation curves representing

the total contributions from all these processes, displayed in figure 9, could be fitted by a one-phase exponential decay function with an average time constant $\tau_1$ in the form of

$$A_r(t) = A_0 + A_1 e^{-(t-t_0)/\tau_1} \tag{6.2}$$

where $t_0$ is the time offset, $A_0$ the amplitude offset, and $A_1$ a fitting coefficient. The resonance amplitude fitting function parameters are summarized in table 6.2.

Table 6.2 First-order exponential function fitting parameters at different RH levels. For each RH level, a distinct time constant is given for each of the 3 cycles shown in figures 9(a) and 9(b). $T_i$ and $T_r$ refer to the illumination and relaxation time periods respectively. R-Square gives a statistical measure of the goodness of fit.

| | **Parameter(s)** | **RH = 20 %** | | | **RH = 70 %** | | |
|---|---|---|---|---|---|---|---|
| | | **1st cycle** | **2nd cycle** | **3rd cycle** | **1st cycle** | **2nd cycle** | **3rd cycle** |
| **$T_r$** | Time Constant ($\tau_1$) | 177.0 | 231.8 | 232.9 | 199.2 | 186.2 | 171.2 |
| | R-Square | 0.9852 | 0.9813 | 0.9806 | 0.9960 | 0.9945 | 0.9944 |
| **$T_i$** | Time Constant ($\tau_1$) | 16.2 | 20.3 | 16.4 | 13.2 | 17.1 | 18.9 |
| | R-Square | 0.9995 | 0.9995 | 0.9909 | 0.9978 | 0.9988 | 0.9979 |

From table 6.2, we derive that the average relaxation time constants are 213 s and 185 s at 20% RH and 70% RH respectively. The relaxation after exposure to UV light is thus faster at high RH. A major factor for this result is that oxygen molecules and water molecules adsorbed on the ZnO surface and grain boundaries interact differently with the photogenerated electrons and holes. At low RH, the predominance of adsorbed and ionized oxygen causes a large separation of the photogenerated holes from the photogenerated electrons. Such separation does not occur so extensively at high RH when

the water molecules are predominant. Therefore, electrons and holes recombine much more quickly upon switching off the UV light, leading to a faster relaxation of the resonance amplitude [192].

The transient response of the resonance frequency and the quality factor of the measured profiles are presented in figure 10. According to the measured results, high RH leads to significant variations of the electrical parameters, extracted from the $S_{21}$ resonance profile, of the ZnO-coated resonator sensor. The resonance frequency downshift during a short illumination time of 2 min reaches 3 MHz at 20% RH, whereas it is about 5 MHz at 70% RH. This increase of the resonance frequency downshift with RH could indicate that, due to the reactivity of water with both photogenerated electrons and holes [192], the effect of RH on the density of created bound charges is not negligible with respect to the effect of UV illumination [179]. To improve the sensor selectivity, it is thus preferable to implement a blocking action against the adsorption of water molecules on the surface and grain boundaries of the electrodeposited ZnO thin film.

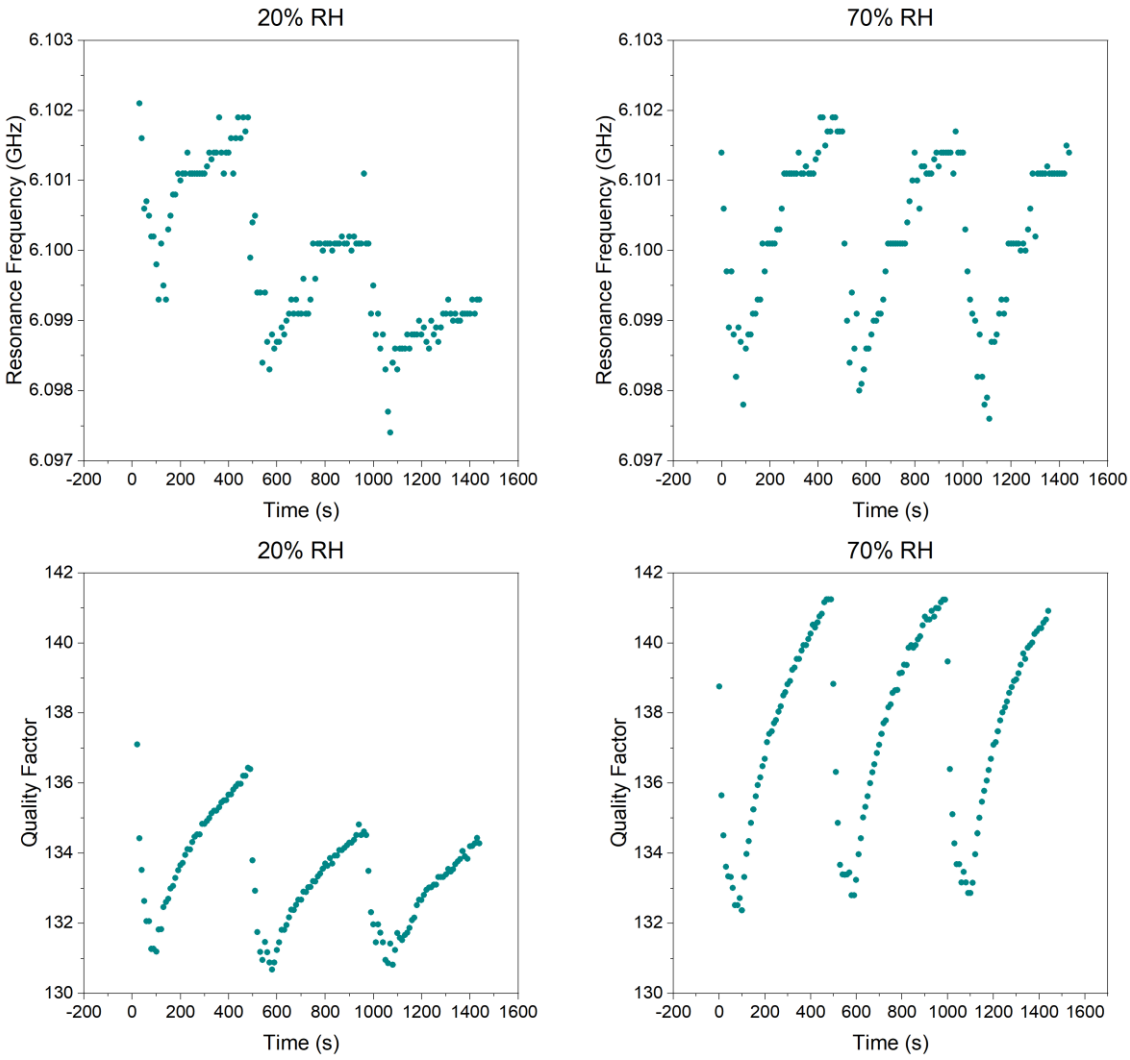


Figure 6.10 (a) Transient response of the resonance frequency at RH = 20%, (b) transient response of the resonance frequency at RH = 70%, (c) quality factor variation at RH = 20%, and (d) quality factor variation at RH = 70%. For all experiments, the illumination time is 2 min and the relaxation time is 6 min.

## 6.4 Conclusion

We report the design, fabrication and characterization of a novel UV irradiation sensor. The device utilizes the simple and compact planar microwave resonator design

that can be easily integrated on printed circuit boards. The insertion of the sensing ZnO thin film is achieved from an aqueous zinc nitrate solution by direct electrodeposition on the readily printed resonator circuit. A major attribute of this method is therefore the facile and low-cost fabrication as it does not involve any resource-intensive techniques such as photolithography or material deposition/removal in vacuum or environment-controlled systems. Time-resolved microwave measurements clearly demonstrated the sensitivity of the sensor at room temperature through downshifts of the resonance frequency and variations of the resonant signal amplitude and quality factor. The undesirable long-lived and persistent post-illumination effects, usually reported for ZnO thin films and nanostructures, were not observed in our sensor. The resonance frequency downshift could be mostly associated with the change in the ZnO film dielectric constant, and hence the effective dielectric constant of the multi-media resonator system. Such change would be brought about by additional bound charges, created by photogenerated carriers, that are ultimately responsible for material polarizability alteration. In addition to this work, the impact of humidity on the microwave photoresponse has been studied experimentally. Induced carrier lifetimes were extracted at both low and high humidity levels and were found to be shorter with increased humidity. At high humidity levels, the sensor exhibits larger resonance frequency downshift and faster relaxation. These effects derive from the different interaction mechanisms of the increased number density of adsorbed water molecules with the photogenerated carriers. These humidity effects are undesirable for the proper operation of the UV irradiation sensor and should therefore be suppressed through the appropriate water blocking technique. Ultimately, the many advantages offered by the use of planar microwave electronics could be leveraged in the service of affordable and

efficient microwave photosensing and sensing in general. In addition, such simplified time-resolved photoresponse methods offer considerable possibilities to conduct fundamental studies on charge carrier dynamics and material properties.

# 7 Conclusion and Outlook

## 7.1 Conclusion

Safety and affordability are the two main incentives that drove me to work on pristine zinc oxide. Nowadays, there are growing concerns worldwide about health and environment, as well as access to basic consumer goods and services such as food and medical care. So, I consider it a small step in the right direction to strive to produce hazardless and inexpensive optoelectronic devices that would meet the high performance demands of the established optoelectronics industry. No doping, alloying, or annealing was performed throughout the extensive work on electrodeposited ZnO.

Of course, there is always a trade-off between cost and performance but we believe that, with sustained research work, we would come closer and closer to optimizing both cost and performance concomitantly. The possibility to produce inexpensive semiconducting ZnO is due primarily to the fact that it can be grown at low temperatures directly from precursor solutions made of inexpensive zinc salts such as zinc acetate or zinc nitrate. I have selected to experiment two solution techniques to grow the ZnO thin films: sol-gel and electrodeposition.

Our first goal was to grow performant ZnO thin films, with improved electron mobility, on LPCVD $Si_3N_4$ by the sol-gel growth technique so that we could integrate ZnO-based devices with devices and systems utilizing $Si_3N_4$ coatings such as solar cells and MEMS. Films of $Si_3N_4$ are technologically very important and are widely used in

semiconductor device and MEMS technologies. Notably, they are applied as gate dielectrics for a-Si TFTs used in backbone display technologies. The material system comprised of sol-gel ZnO grown on $Si_3N_4$ has not been apparently considered for electronic device applications such as thin film transistors. Therefore, no pertinent data in the literature was found concerning the electronic properties of this system. The use of silicon nitride as growth substrate resulted in a significant electron mobility enhancement with respect to its silicon oxide counterpart. A high effective electron mobility of 33 $cm^2 V^{-1} s^{-1}$ was achieved. This value compares very favorably with current state-of-the-art electron mobilities reported in solution-processed ZnO thin films. The enhanced electron mobility correlates to the superior structural and crystalline qualities of the ZnO film coating the $Si_3N_4$ substrate such as the lower density of grain boundaries, lower strain, better (002) crystal orientation, and lower interface traps density. These results indicate that the crystalline quality and defect chemistry of the sol-gel grown film, and ultimately its electrical properties, are significantly affected through nucleation and growth, by the specific properties of the growth substrate.

Despite these significant improvements in the electron mobility of the sol-gel based ZnO films, the carrier concentration and interface trap density have still proven difficult to control reproducibly, resulting in low breakdown fields, high sub-threshold slope and inconsistent threshold voltages. Major conductivity issues in ZnO are generally encountered in the form of high n-type background doping and lack of reproducible p-type doping. Furthermore, the majority of growth techniques produce ZnO that exhibits high n-type doping ($> 10^{17}$ $cm^{-3}$) and low electron mobilities. To tackle some of these issues,

we have used a distinctly simple, low-cost, low-temperature electrodeposition process, carried out in an ambient atmosphere, to synthesize highly-textured ZnO films optimized for electronic performance. Thanks to an extensive optimization process, we were able to electrodeposit ZnO films on copper substrates which exhibit remarkably low carrier concentrations $\sim 2.8 \times 10^{14}$ cm$^{-3}$ and minimum electron mobilities as high as 80 cm$^2$ V$^{-1}$ s$^{-1}$. These combined results of carrier concentration and charge transport are close to those obtained in hydrothermally grown single crystals of bulk ZnO. We believe that the superior columnar structure and composition in electrodeposited films is at least partly due to the fact that electrodeposition is performed at or near the Nernst potential and is therefore closer to equilibrium than the highly non-equilibrium, kinetically limited sol-gel process (involving spin-coating and pyrolysis steps).

The test Schottky diodes, fabricated from these electrodeposited ZnO films, exhibited high rectification ratios of ~ $10^6$, low resistance in the on-state, reverse saturation current densities as low as $8 \times 10^{-10}$ A cm$^{-2}$, and ideality factors as low as 2, in spite of non-optimized ohmic contacts. These diodes stand out from previously reported solution-processed ZnO diodes in terms of their superior electrical characteristics. Good electron transport in these films was inferred from the ohmic conduction region obtained at forward bias. These electrodeposited ZnO films are particularly suitable for building large-scale low-cost vertical devices with high breakdown voltage and high current handling capabilities.

Because of the nominally low processing temperature of the successful electrodeposition technique utilized on rigid copper-coated substrate, we attempted the electrodeposition of a ZnO thin film optimized for electronic performance on a flexible substrate. The design of the layers stack was modified to allow for thinner layers. Test Schottky diodes, with no top ohmic contacts, combining the electrodeposited ZnO film as the semiconductor layer and the underlying copper as the metal contact were successfully fabricated on flexible Kapton substrate with an intermediate, thin Ti adhesion layer between the Kapton and the copper. The final test devices exhibited high rectification ratios (~ $10^6$), low ideality factors (~ 2 to 3), and breakdown voltages largely exceeding 3 V, that surpass the current state-of-the-art for solution-processed ZnO films. The bending tests demonstrated that the diodes possess potential capabilities to retain device operationality with good performance under mechanical deformations. TEM-SAED examinations of the electrodeposited ZnO film on the flexible substrate were performed over wide areas from the bottom region of the electrodeposited film (near the bottom interface with copper) and from the top region of the same film (near the top surface). A spectacular transformation from a ring pattern to a spot pattern occurs as we scan upward. Such observation suggests that the crystallinity of the film is enhanced with increased thickness. These overall findings are promising and command further investigations that may implement some of the new strategies that use inorganic materials on flexible platforms.

The combination of high electron mobilities, moderately low carrier concentrations, sizable ZnO layer thicknesses, and high deposition rates makes the low-cost ZnO film

electrodeposition technique very attractive for the realization of high blocking voltage devices. Good charge transport is achieved along the structural columns which feature good crystalline order and low grain boundaries density. In the case of vertical power transistors, a collector drift region made of a thick and low-doped ZnO layer is where high electric fields occur, thereby enabling the device as a whole to withstand high voltages before breakdown. In this case, we electrodeposited ZnO on Pt-coated rigid substrates because of the higher Pt work function and to reduce the oxidation of the Pt/ZnO interface. The test vertical Schottky diode exhibited an ideality factor of 1.10, a carrier concentration of $2.5 \times 10^{15}$ $cm^{-3}$, and a critical electric field of 800 kV $cm^{-1}$. Such results are rarely attained with solution-processed ZnO. The critical electric field of 800 kV $cm^{-1}$ is extremely high when compared to literature [193]. To our knowledge, this is the first investigation of breakdown voltage in electrodeposited ZnO material. The critical electric field has ample room for future improvements with more optimized material and device processing techniques. Our results show that electrodeposited ZnO is an inexpensive and environment-friendly option for power electronics, bioengineering, and energy-harvesting systems, including full-wave bridge rectifiers and vertical power transistors.

The simplicity and low-cost of the ZnO electrodeposition method can be leveraged in the service of many other applications. In this respect, we have realized the facile and seamless fabrication of a novel ultra-violet irradiation sensor based on the photosensing properties of a ZnO film directly electrodeposited on the conductive copper strips of a planar microwave resonator laid out on a PCB. Time-resolved microwave measurements of the transient photoresponse to ultraviolet illumination demonstrated the sensitivity of

the sensor at room temperature through variations of the $S_{21}$-parameter resonance profile in general and downshifts of the resonance frequency in particular. The undesirable long-lived and persistent post-illumination effects, usually reported in ZnO thin films and nanostructures, were not observed in our sensor. The effect of ambient humidity change on the reliability of these photoresponse measurements has been experimentally assessed and potential solutions were discussed to tackle this issue.

## 7.2 Outlook

The success achieved in the electrochemical deposition of highly textured ZnO films, with very good electrical properties, opens out the prospects to work on the fabrication of devices susceptible to exhibit high levels of performance. In this context, I propose the following three different routes: power thin film transistors, power Schottky diodes and discrete two-terminal devices on flexible substrates

### A. Power thin film transistors

The combination of these results and the maturity of our research in this subject matter leads us to consider the project of building a power transistor (unipolar and possibly bipolar as in heterojunction bipolar transistors (HBT's)) with high blocking voltage capability. This transistor consists of a collector drift region made of thick and low-doped electrodeposited ZnO layer which takes over the high electric fields. The specific on-state resistance resulting from the thick collector drift region is expected to be relatively small, as it should be, because of the high electron mobilities achieved in our ZnO films. The gate modulation is carried out through either an MOS structure (as in thin film transistors)

or through direct metal-semiconductor junction (as in MESFET's). The device architecture features vertical charge transport along the collector region with high cross-sectional area, which increases the device power handling capability.

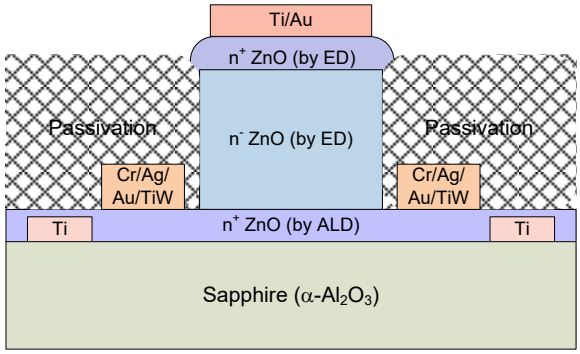


Figure 7.1 Proposed power transistor for future work.

The simplicity, low fabrication cost, and state-of-the-art performance of this device could be of value for consumer and industrial power electronics applications and high-efficiency energy conversion systems for solar energy harvesting. The marketability potential of this product is great as a low-cost alternative to the leading commercialized power transistors, namely power MOSFET's and IGBT's. This work could further pave the way to new and unsuspected ZnO applications in the thin film and nanotechnology industries down the road.

## B. Power Schottky diodes

There is a lot of potential for improvement in the material growth and device fabrication of power Schottky diodes as stand-alone and test structures. High breakdown voltage and low on-state resistance can be achieved with proper material quality and

orientation and more precise device processing such as optimization of the ohmic contact resistance which greatly impacts device performance. Other metallic substrates, such as silver, platinum, and titanium tungsten can readily be investigated as well.

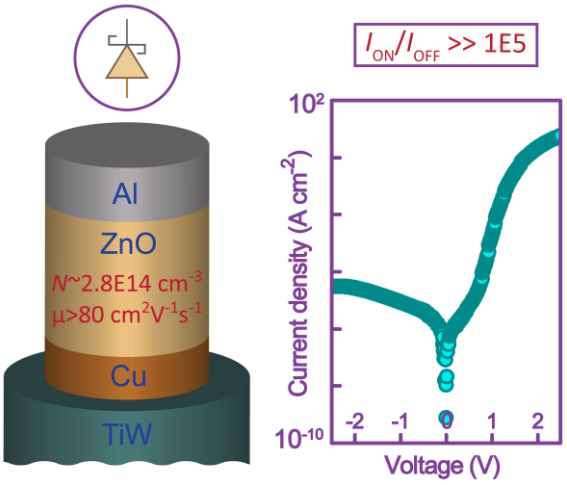


Figure 7.2 Our fabricated Cu/ZnO/Al Schottky diode. Reproduced/adapted with permission from Ref. [185]; Copyright 2016 The Royal Society of Chemistry.

It is noteworthy that a test Schottky diode fabricated afterwards with electrodeposited ZnO on rigid copper substrate (at $E_V$ = -0.9 V and T = 70 °C) has exhibited a breakdown voltage of ~ 170 V for a ZnO film thickness of ~ 6 μm (measured by profilometry).

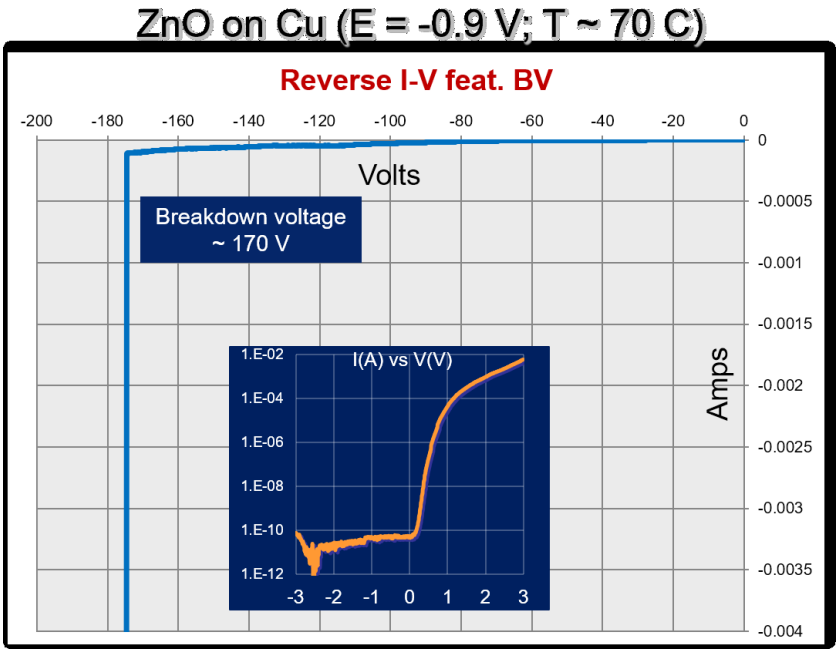


Figure 7.3 Example of a high breakdown voltage (~170 V) achieved with a device made of electrodeposited ZnO on Cu.

## C. Discrete two-terminal devices on flexible substrates

Our recent work on flexible polyimide substrates is very promising and propels us to refine our objectives to develop patterned devices with possibility of characterizing both the electrical and mechanical properties of the stacked layers materials.

## D. Higher crystalline order of electrodeposited ZnO

The growth of ZnO films of higher crystalline order on closely matched substrate lattices such as GaN or the formation of n-p heterojunctions such as <002> ZnO on <111> Si could be considered. Achieving controllable isotropic and anisotropic growth is also another goal that could be pursued. A tentative ZnO electrodeposition on HF-treated <111> p-Si substrate produced the following ZnO crystals or grains:

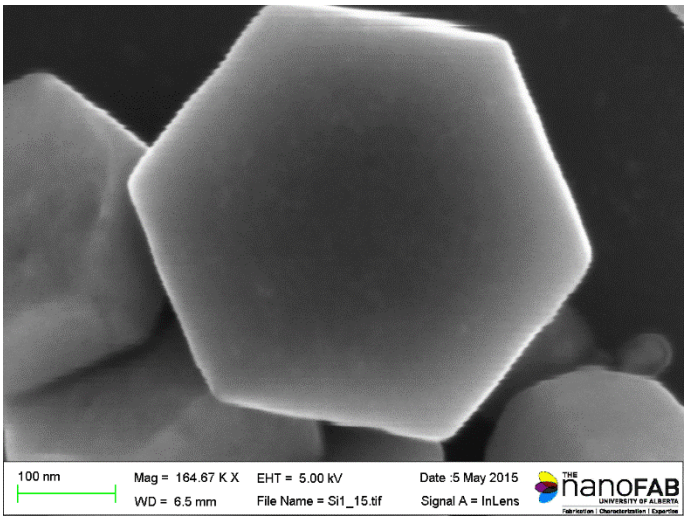


Figure 7.4 ZnO crystals produced by electrodeposition.

# Bibliography


[1] Craddock, P. T., 2008, "Mining and Metallurgy, chapter 4," The Oxford Handbook of Engineering and Technology in the Classical World, J. P. Oleson, ed., Oxford University Press, New York.

[2] Ibn Sina (aka Avicenna), 1999, "The Canon of Medicine, Volume 2: Natural Pharmaceuticals," L. Bakhtiar, ed., Great Books of the Islamic World, Inc., distributed by KAZI Publications in Chicago, USA.

[3] Heiland, G., Mollwo, E., and Stockmann, F., 1959, "Electronic Processes in Zinc Oxide," Solid State Physics-Advances in Research and Applications, 8, pp. 191-323.

[4] Litton, C. W., Reynolds, D. C., and Collins, T. C., 2011, "Zinc Oxide Materials for Electronic and Optoelectronic Device Applications," Wiley, Chichester, UK.

[5] Fuller, M. L., 1929, "A method of determining the axial ratio of a crystal from x-ray diffraction data the axial ratio and lattice constants of zinc oxide," Science, 70, pp. 196-198.

[6] Bunn, C. W., 1935, "The lattice-dimensions of zinc oxide," Proceedings of the Physical Society, 47, pp. 835-842.

[7] Brown, H. E., 1976, "Zinc Oxide. Properties and Applications," International Lead Zinc Research Organization, Inc., New York.

[8] Feng, Z. C., 2013, "Handbook of Zinc Oxide and Related Materials," CRC Press, Boca Raton, FL.

[9] Brown, H. E., 1957, "Zinc Oxide Rediscovered," New Jersey Zinc Company, New York.

[10] Jagadish, C., and Pearton, S., 2006, "Zinc Oxide Bulk, Thin Films and Nanostructures: Processing, Properties and Applications," Elsevier, Amsterdam, the Netherlands.

[11] Ellmer, K., Klein, A., and Rech, B., 2008, "Transparent Conductive Zinc Oxide: Basics and Applications in Thin Film Solar Cells," Springer Berlin Heidelberg.

[12] Damen, T. C., Porto, S. P. S., and Tell, B., 1966, "Raman effect in zinc oxide," Physical Review, 142(2), p. 570.

[13] Thomas, D. G., 1960, "The exciton spectrum of zinc oxide," Journal of Physics and Chemistry of Solids, 15(1-2), pp. 86-96.

[14] Mead, C. A., 1965, "Surface barriers on ZnSe and ZnO," Physics Letters, 18(3), p. 218.

[15] Drapak, I. T., 1968, "Visible luminescence of a ZnO-Cu2O heterojunction," Soviet Physics Semiconductors-USSR, 2(4), p. 513.

[16] Thomas, B. W., and Walsh, D., 1973, "Metal-insulator-semiconductor electroluminescent diodes in single-crystal zinc oxide," Electronics Letters, 9(16), pp. 362-363.

[17] Tsurkan, A. E., Fedotova, N. D., Kicherman, L. V., and Pasko, P. G., 1975, "Injection electroluminescence emitted by n-ZnO-p-ZnTe heterojunctions," Soviet Physics Semiconductors-USSR, 9(6), pp. 786-787.

[18] Brillson, L. J., 1978, "Chemical-reaction and charge redistribution at metal-semiconductor interfaces," Journal of Vacuum Science and Technology, 15(4), pp. 1378-1383.

[19] Mimura, T., Hiyamizu, S., Fujii, T., and Nanbu, K., 1980, "A new field-effect transistor with selectively doped GaAs-n-AlxGa1-xAs heterojunctions," Japanese Journal of Applied Physics, 19(5), pp. L225-L227.

[20] Rosenberg, J. J., Benlamri, M., Kirchner, P. D., Woodall, J. M., and Pettit, G. D., 1985, "An In0.15Ga0.85As/GaAs pseudomorphic single quantum well HEMT," IEEE Electron Device Letters, 6(10), pp. 491-493.

[21] Benlamri, M., 1985, "A pseudomorphic heterojunction field effect transistor," M.S. Thesis, Brown University, Providence, RI.

[22] Klingshirn, C., Hauschild, R., Priller, H., Decker, M., Zeller, J., and Kalt, H., 2005, "ZnO rediscovered - once again!?," Superlattices and Microstructures, 38(4-6), pp. 209-222.

[23] NanoMarkets, LC, 2009, "Markets for Zinc Oxide in Electronics."

[24] Gordon, R. G., 2000, "Criteria for choosing transparent conductors," Mrs Bulletin, 25(8), pp. 52-57.

[25] Levinson, L. M., and Philipp, H. R., 1986, "Zinc-oxide varistors - a review," American Ceramic Society Bulletin, 65(4), pp. 639-646.

[26] Maeda, K., Sato, M., Niikura, I., and Fukuda, T., 2005, "Growth of 2 inch ZnO bulk single crystal by the hydrothermal method," Semiconductor Science and Technology, 20(4), pp. S49-S54.

[27] Hofstetter, D., Bonetti, Y., Giorgetta, F. R., El-Shaer, A.-H., Bakin, A., Waag, A., Schmidt-Grund, R., Schubert, M., and Grundmann, M., 2007, "Demonstration of an ultraviolet ZnO-based optically pumped third order distributed feedback laser," Applied Physics Letters, 91(11).

[28] Abbel, R., Galagan, Y., and Groen, P., 2018, "Roll-to-roll fabrication of solution processed electronics," Advanced Engineering Materials, 20(8).

[29] Bhattacharya, R., 2009, "Chemical bath deposition, electrodeposition, and electroless deposition of semiconductors, superconductors, and oxide materials," Solution processing of inorganic materials, D. B. Mitzi, ed., John Wiley and Sons, Inc., Hoboken, NJ

[30] Janotti, A., and Van de Walle, C. G., 2009, "Fundamentals of zinc oxide as a semiconductor," Rep Prog Phys, 72(12).

[31] Park, S. H. K., Hwang, C. S., Ryu, M., Yang, S., Byun, C., Shin, J., Lee, J. I., Lee, K., Oh, M. S., and Im, S., 2009, "Transparent and photo-stable ZnO thin-film transistors to drive an

active matrix organic-light-emitting-diode display panel," Advanced Materials, 21(6), p. 678.

[32] DisplayBank, 2011, "Transparent Display Technology and Market Forecast".

[33] Benlamri, M., Farsinezhad, S., Barlage, D. W., and Shankar, K., 2016, "Communication-High Performance Schottky Diodes on Flexible Substrates Using ZnO Electrodeposited on Cu," ECS Journal of Solid State Science and Technology, 5(6), pp. P324-P326.

[34] Zhang, H., Wu, J., Zhai, C., Du, N., Ma, X., and Yang, D., 2007, "From ZnO nanorods to 3D hollow microhemispheres: solvothermal synthesis, photoluminescence and gas sensor properties," Nanotechnology, 18(45).

[35] Tuomisto, F., Saarinen, K., Look, D. C., and Farlow, G. C., 2005, "Introduction and recovery of point defects in electron-irradiated ZnO," Physical Review B, 72(8).

[36] Dalcorso, A., Posternak, M., Resta, R., and Baldereschi, A., 1994, "Ab-initio study of piezoelectricity and spontaneous polarization in ZnO," Physical Review B, 50(15), pp. 10715-10721.

[37] Quaranta, F., Valentini, A., Rizzi, F. R., and Casamassima, G., 1993, "Dual-ion-beam sputter-deposition of ZnO films," Journal of Applied Physics, 74(1), pp. 244-248.

[38] Hallwig, D., and Mollwo, E., 1975, Verhandl. DPG, (VI) 10, HL37.

[39] Lide, D. R., 1992, "CRC Handbook of Chemistry and Physics," CRC Press, New York.

[40] Rossler, U., 1999, New Series, Group III, Landolt-Bornstein, ed., Springer, Berlin.

[41] Look, D. C., 2001, "Recent advances in ZnO materials and devices," Materials Science and Engineering B-Solid State Materials for Advanced Technology, 80(1-3), pp. 383-387.

[42] Chow, T. P., and Tyagi, R., 1994, "Wide bandgap compound semiconductors for superior high-voltage unipolar power devices," IEEE Transactions on Electron Devices, 41(8), pp. 1481-1483.

[43] Cordaro, J. F., Shipway, C. E., and Schott, J. T., 1987, "Radiation hardness of zinc-oxide varistors," Journal of Applied Physics, 61(1), pp. 429-431.

[44] Ozgur, U., Alivov, Y. I., Liu, C., Teke, A., Reshchikov, M. A., Dogan, S., Avrutin, V., Cho, S. J., and Morkoc, H., 2005, "A comprehensive review of ZnO materials and devices," Journal of Applied Physics, 98(4).

[45] Nickel, N. H., and Terukov, E., 2005, "Zinc Oxide_A Material for Micro- and Optoelectronic Applications," Springer, The Netherlands.

[46] Harrison, S. E., 1954, "Conductivity and Hall effect of ZnO at low temperatures," Physical Review, 93(1), pp. 52-62.

[47] Neumann, G., 1981, "Current Topics in Materials Science," Current Topics in Materials Science, K. E., ed., North Holland, Amsterdam, p. 152.

[48] Janotti, A., and Van de Walle, C. G., 2005, "Oxygen vacancies in ZnO," Applied Physics Letters, 87(12).

[49] Janotti, A., and Van de Walle, C. G., 2006, "New insights into the role of native point defects in ZnO," Journal of Crystal Growth, 287(1), pp. 58-65.

[50] Morkoc, H., and Ozgur, U., 2009, "Zinc Oxide_Fundamentals, Materials and Device Technology," Wiley.

[51] Wager, J. F., 2005, "ZnO transparent thin-film transistor device physics," Nato Sci Ser Ii Math, 194, pp. 217-224.

[52] Bandyopadhyay, S., 2012, "Physics of Nanostructured Solid State Devices," Springer.

[53] Albrecht, J. D., Ruden, P. P., Limpijumnong, S., Lambrecht, W. R. L., and Brennan, K. F., 1999, "High field electron transport properties of bulk ZnO," Journal of Applied Physics, 86(12), pp. 6864-6867.

[54] Hutson, A. R., 1957, "Hall effect studies of doped zinc oxide single crystals," Physical Review, 108(2), pp. 222-230.

[55] Baer, W. S., 1967, "Faraday rotation in ZnO - determination of electron effective mass," Physical Review, 154(3), p. 785.

[56] Hagemark, K. I., and Chacka, L. C., 1975, "Electrical transport properties of Zn doped ZnO," Journal of Solid State Chemistry, 15(3), pp. 261-270.

[57] Utsch, B., and Hausmann, A., 1975, "Hall-effect and conductivity measurements of zinc-oxide single-crystals with oxygen vacancies as donors," Zeitschrift Fur Physik B-Condensed Matter, 21(1), pp. 27-31.

[58] Masetti, G., Severi, M., and Solmi, S., 1983, "Empirical relationships between carrier mobility and carrier concentration in arsenic-doped, phosphorus-doped, and boron-doped silicon," Journal of the Electrochemical Society, 130(3), p. C100.

[59] Seto, J. Y. W., 1975, "Electrical properties of polycrystalline silicon films," Journal of Applied Physics, 46(12), pp. 5247-5254.

[60] Baccarani, G., Ricco, B., and Spadini, G., 1978, "Transport properties of polycrystalline silicon films," Journal of Applied Physics, 49(11), pp. 5565-5570.

[61] Ellmer, K., 2001, "Resistivity of polycrystalline zinc oxide films: current status and physical limit," Journal of Physics D-Applied Physics, 34(21), pp. 3097-3108.

[62] Fortunato, E., Barquinha, P., and Martins, R., 2012, "Oxide Semiconductor Thin-Film Transistors: A Review of Recent Advances," Advanced Materials, 24(22), pp. 2945-2986.

[63] Adamopoulos, G., Thomas, S., Wobkenberg, P. H., Bradley, D. D. C., McLachlan, M. A., and Anthopoulos, T. D., 2011, "High-Mobility Low-Voltage ZnO and Li-Doped ZnO

Transistors Based on ZrO2 High-k Dielectric Grown by Spray Pyrolysis in Ambient Air," Advanced Materials, 23(16), p. 1894.

[64] OBrien, P., Saeed, T., and Knowles, J., 1996, "Speciation and the nature of ZnO thin films from chemical bath deposition," Journal of Materials Chemistry, 6(7), pp. 1135-1139.

[65] Ohyama, M., Kozuka, H., and Yoko, T., 1997, "Sol-gel preparation of ZnO films with extremely preferred orientation along (002) plane from zinc acetate solution," Thin Solid Films, 306(1), pp. 78-85.

[66] Thomas, S. R., Pattanasattayavong, P., and Anthopoulos, T. D., 2013, "Solution-processable metal oxide semiconductors for thin-film transistor applications," Chemical Society Reviews, 42(16), pp. 6910-6923.

[67] Cheng, H. C., Chen, C. F., and Tsay, C. Y., 2007, "Transparent ZnO thin film transistor fabricated by sol-gel and chemical bath deposition combination method," Applied Physics Letters, 90(1).

[68] Wolff, K., and Hilleringmann, U., 2011, "Solution processed inverter based on zinc oxide nanoparticle thin-film transistors with poly(4-vinylphenol) gate dielectric," Solid-State Electronics, 62(1), pp. 110-114.

[69] Dai, W., Pan, X., Chen, S., Chen, C., Wen, Z., Zhang, H., and Ye, Z., 2014, "Honeycomb-like NiO/ZnO heterostructured nanorods: photochemical synthesis, characterization, and enhanced UV detection performance," Journal of Materials Chemistry C, 2(23), pp. 4606-4614.

[70] Wang, X., Tian, W., Liao, M., Bando, Y., and Golberg, D., 2014, "Recent advances in solution-processed inorganic nanofilm photodetectors," Chemical Society Reviews, 43(5), pp. 1400-1422.

[71] Liu, X., Gu, L., Zhang, Q., Wu, J., Long, Y., and Fan, Z., 2014, "All-printable band-edge modulated ZnO nanowire photodetectors with ultra-high detectivity," Nature Communications, 5.

[72] Ryu, Y. R., Lee, T. S., Lubguban, J. A., White, H. W., Kim, B. J., Park, Y. S., and Youn, C. J., 2006, "Next generation of oxide photonic devices: ZnO-based ultraviolet light emitting diodes," Applied Physics Letters, 88(24).

[73] Feng, Q.-J., Liang, H.-W., Mei, Y.-Y., Liu, J.-Y., Ling, C. C., Tao, P.-C., Pan, D.-Z., and Yang, Y.-Q., 2015, "ZnO single microwire homojunction light emitting diode grown by electric field assisted chemical vapor deposition," Journal of Materials Chemistry C, 3(18), pp. 4678-4682.

[74] Lee, B. R., Jung, E. D., Park, J. S., Nam, Y. S., Min, S. H., Kim, B.-S., Lee, K.-M., Jeong, J.-R., Friend, R. H., Kim, J. S., Kim, S. O., and Song, M. H., 2014, "Highly efficient inverted polymer light-emitting diodes using surface modifications of ZnO layer," Nature Communications, 5.

[75] Zhang, J., Li, Y., Zhang, B., Wang, H., Xin, Q., and Song, A., 2015, "Flexible indium-gallium-zinc-oxide Schottky diode operating beyond 2.45GHz," Nature communications, 6, p. 7561.

[76] Xin, Q., Yan, L. L., Luo, Y., and Song, A. M., 2015, "Study of breakdown voltage of indium-gallium-zinc-oxide-based Schottky diode," Applied Physics Letters, 106(11).

[77] Sun, B., and Sirringhaus, H., 2005, "Solution-processed zinc oxide field-effect transistors based on self-assembly of colloidal nanorods," Nano Letters, 5(12), pp. 2408-2413.

[78] Mourey, D. A., Park, S. K., Zhao, D. L. A., Sun, J., Li, Y. Y. V., Subramanian, S., Nelson, S. F., Levy, D. H., Anthony, J. E., and Jackson, T. N., 2009, "Fast, simple ZnO/organic CMOS integrated circuits," Org Electron, 10(8), pp. 1632-1635.

[79] Ayouchi, R., Leinen, D., Martin, F., Gabas, M., Dalchiele, E., and Ramos-Barrado, J. R., 2003, "Preparation and characterization of transparent ZnO thin films obtained by spray pyrolysis," Thin Solid Films, 426(1-2), pp. 68-77.

[80] Okamura, T., Seki, Y., Nagakari, S., and Okushi, H., 1992, "Preparation of n-ZnO/p-Si heterojunction by sol-gel process," Japanese Journal of Applied Physics Part 2-Letters, 31(6B), pp. L762-L764.

[81] Ohya, Y., Saiki, H., and Takahashi, Y., 1994, "Preparation of transparent, electrically conducting ZnO film from zinc acetate and alkoxide," Journal of Materials Science, 29(15), pp. 4099-4103.

[82] Izaki, M., and Omi, T., 1996, "Transparent zinc oxide films prepared by electrochemical reaction," Applied Physics Letters, 68(17), pp. 2439-2440.

[83] Peulon, S., and Lincot, D., 1996, "Cathodic electrodeposition from aqueous solution of dense or open-structured zinc oxide films," Advanced Materials, 8(2), p. 166.

[84] Znaidi, L., 2010, "Sol-gel-deposited ZnO thin films: A review," Materials Science and Engineering B-Advanced Functional Solid-State Materials, 174(1-3), pp. 18-30.

[85] Hu, M. Z. C., Payzant, E. A., and Byers, C. H., 2000, "Sol-gel and ultrafine particle formation via dielectric tuning of inorganic salt-alcohol-water solutions," Journal of Colloid and Interface Science, 222(1), pp. 20-36.

[86] Switzer, J. A., 1987, "Electrochemical synthesis of ceramic films and powders," American Ceramic Society Bulletin, 66(10), pp. 1521-1525.

[87] Musselman, K. P., Gershon, T., Schmidt-Mende, L., and MacManus-Driscoll, J. L., 2011, "Macroscopically uniform electrodeposited ZnO films on conducting glass by surface tension modification and consequent demonstration of significantly improved p-n heterojunctions," Electrochimica Acta, 56(11).

[88] Brillson, L. J., and Lu, Y., 2011, "ZnO Schottky barriers and Ohmic contacts," Journal of Applied Physics, 109(12).

[89] Bardeen, J., 1947, "Surface states and rectification at a metal semi-conductor contact," Physical Review, 71(10), pp. 717-727.

[90] Chatman, S., Ryan, B. J., and Poduska, K. M., 2008, "Selective formation of Ohmic junctions and Schottky barriers with electrodeposited ZnO," Applied Physics Letters, 92(1), p. 012103.

[91] Tung, R. T., 2014, "The physics and chemistry of the Schottky barrier height," Applied Physics Reviews, 1(1), p. 011304.

[92] Allen, M. W., and Durbin, S. M., 2008, "Influence of oxygen vacancies on Schottky contacts to ZnO," Applied Physics Letters, 92(12).

[93] Schroder, D. K., 2006, "Semiconductor Material and Device Characterization," John Wiley and Sons, Hoboken, NJ.

[94] Sze, S. M., and Ng, K. K., 2006, "Physics of semiconductor devices," John Wiley and Sons, Hoboken, NJ.

[95] Cheung, S. K., and 85-87, N. W. C., 1986, "Extraction of Schottky diode parameters from forward current-voltage characteristics," Applied Physics Letters, 49(2), pp. 85-87.

[96] Fujihara, S., Sasaki, C., and Kimura, T., 2001, "Crystallization behavior and origin of c-axis orientation in sol-gel-derived ZnO: Li thin films on glass substrates," Applied Surface Science, 180(3-4), pp. 341-350.

[97] Natsume, Y., and Sakata, H., 2000, "Zinc oxide films prepared by sol-gel spin-coating," Thin Solid Films, 372(1-2), pp. 30-36.

[98] Bao, D. H., Gu, H. S., and Kuang, A. X., 1998, "Sol-gel-derived c-axis oriented ZnO thin films," Thin Solid Films, 312(1-2), pp. 37-39.

[99] Lin, L.-Y., and Kim, D.-E., 2009, "Effect of annealing temperature on the tribological behavior of ZnO films prepared by sol-gel method," Thin Solid Films, 517(5), pp. 1690-1700.

[100] Zhai, J. W., Zhang, L. Y., and Yao, X., 2000, "The dielectric properties and optical propagation loss of c-axis oriented ZnO thin films deposited by sol-gel process," Ceramics International, 26(8), pp. 883-885.

[101] Basak, D., Amin, G., Mallik, B., Paul, G. K., and Sen, S. K., 2003, "Photoconductive UV detectors on sol-gel-synthesized ZnO films," Journal of Crystal Growth, 256(1-2), pp. 73-77.

[102] Ghosh, R., Basak, D., and Fujihara, S., 2004, "Effect of substrate-induced strain on the structural, electrical, and optical properties of polycrystalline ZnO thin films," Journal of Applied Physics, 96(5), pp. 2689-2692.

[103] Bothe, K. M., von Hauff, P. A., Afshar, A., Foroughi-Abari, A., Cadien, K. C., and Barlage, D. W., 2012, "Capacitance Modeling and Characterization of Planar MOSCAP Devices for

Wideband-Gap Semiconductors With High-kappa Dielectrics," IEEE Transactions on Electron Devices, 59(10), pp. 2662-2666.

[104] Ngwashi, D. K., Cross, R. B. M., Paul, S., Milanov, A. P., and Devi, A., 2011, "High mobility ZnO thin film transistors using the novel deposition of high-k dielectrics," Transparent Conducting Oxides and Applications, J. J. Berry, E. Fortunato, J. E. Medvedeva, and Y. Shigesato, eds., pp. 71-76.

[105] Na, K. D., Kim, J. H., Park, T. J., Song, J., Hwang, C. S., and Choi, J. H., 2010, "Improved properties of Pt-HfO2 gate insulator-ZnO semiconductor thin film structure by annealing of ZnO layer," Thin Solid Films, 518(18), pp. 5326-5330.

[106] Carcia, P. F., McLean, R. S., and Reilly, M. H., 2006, "High-performance ZnO thin-film transistors on gate dielectrics grown by atomic layer deposition," Applied Physics Letters, 88(12).

[107] Li, C., Li, Y., Wu, Y., Ong, B., and Loutfy, R., 2009, "Fabrication conditions for solution-processed high-mobility ZnO thin-film transistors," Journal of Materials Chemistry, 19(11), pp. 1626-1634.

[108] Fortunato, E., Barquinha, P., Pimentel, A., Goncalves, A., Marques, A., Pereira, L., and Martins, R., 2005, "Recent advances in ZnO transparent thin film transistors," Thin Solid Films, 487(1-2), pp. 205-211.

[109] Adl, A. H., Ma, A., Gupta, M., Benlamri, M., Tsui, Y. Y., Barlage, D. W., and Shankar, K., 2012, "Schottky Barrier Thin Film Transistors Using Solution-Processed n-ZnO," ACS Applied Materials and Interfaces, 4(3).

[110] Lee, J. H., Ko, K. H., and Park, B. O., 2003, "Electrical and optical properties of ZnO transparent conducting films by the sol-gel method," Journal of Crystal Growth, 247(1-2), pp. 119-125.

[111] Mridha, S., and Basak, D., 2007, "Effect of thickness on the structural, electrical and optical properties of ZnO films," Materials Research Bulletin, 42(5), pp. 875-882.

[112] Huang, Y. Q., Liu, M. D., Li, Z., Zeng, Y. K., and Liu, S. B., 2003, "Raman spectroscopy study of ZnO-based ceramic films fabricated by novel sol-gel process," Materials Science and Engineering B-Solid State Materials for Advanced Technology, 97(2), pp. 111-116.

[113] Li, C., Li, X. C., Yan, P. X., Chong, E. M., Liu, Y., Yue, G. H., and Fan, X. Y., 2007, "Research on the properties of ZnO thin films deposited by using filtered cathodic arc plasma technique on glass substrate under different flow rate of O-2," Applied Surface Science, 253(8), pp. 4000-4005.

[114] Sagar, P., Shishodia, P. K., Mehra, R. M., Okada, H., Wakahara, A., and Yoshida, A., 2007, "Photoluminescence and absorption in sol-gel-derived ZnO films," Journal of Luminescence, 126(2), pp. 800-806.

[115] Kim, M. S., Kim, S., and Leem, J. Y., 2012, "Laser-assisted sol-gel growth and characteristics of ZnO thin films," Applied Physics Letters, 100(25).

[116] Pozar, D. M., 2005, "Microwave Engineering, 3ed.," John Wiley & Sons, Hoboken, NJ.

[117] Kim, Y. G., Avis, C., and Jang, J., 2012, "Low Voltage Driven, Stable Solution-Processed Zinc-Tin-Oxide TFT with HfOy and AlOx Stack Gate Dielectric," ECS Solid State Letters, 1(2), pp. Q23-Q25.

[118] Park, J. H., Yoo, Y. B., Lee, K. H., Jang, W. S., Oh, J. Y., Chae, S. S., and Baik, H. K., 2013, "Low-Temperature, High-Performance Solution-Processed Thin-Film Transistors with Peroxo-Zirconium Oxide Dielectric," ACS Applied Materials and Interfaces, 5(2), pp. 410-417.

[119] Gierałtowska, S., Wachnicki, Ł., Witkowski, B. S., Godlewski, M., and Guziewicz, E., 2013, "Properties of thin films of high-k oxides grown by atomic layer deposition at low temperature for electronic applications," Optica Applicata, 43(1), pp. 17-25.

[120] Nicollia, Eh., and Goetzber, A., 1967, "Si-SiO2 interface - electrical properties as determined by metal-insulator-silicon conductance technique," Bell System Technical Journal, 46(6), p. 1055.

[121] Benlamri, M., Bothe, K. M., Ma, A. M., Shoute, G., Afshar, A., Sharma, H., Mohammadpour, A., Gupta, M., Cadien, K. C., Tsui, Y. Y., Shankar, K., and Barlage, D. W., 2014, "High-mobility solution-processed zinc oxide thin films on silicon nitride," Physica Status Solidi-Rapid Research Letters, 8(10), pp. 871-875.

[122] Pauporté, T., and Lincot, D., 1999, "Heteroepitaxial electrodeposition of zinc oxide films on gallium nitride," Applied Physics Letters, 75(24), pp. 3817-3819.

[123] Adl, A. H., Kar, P., Farsinezhad, S., Sharma, H., and Shankar, K., 2015, "Effect of sol stabilizer on the structure and electronic properties of solution-processed ZnO thin films," RSC Advances, 5(106), pp. 87007-87018.

[124] Ghosh, R., Paul, G. K., and Basak, D., 2005, "Effect of thermal annealing treatment on structural, electrical and optical properties of transparent sol-gel ZnO thin films," Materials Research Bulletin, 40(11), pp. 1905-1914.

[125] Ong, B. S., Li, C. S., Li, Y. N., Wu, Y. L., and Loutfy, R., 2007, "Stable, solution-processed, high-mobility ZnO thin-film transistors," Journal of the American Chemical Society, 129(10), p. 2750.

[126] Yilmaz, M., Caldiran, Z., Deniz, A. R., Aydogan, S., Gunturkun, R., and Turut, A., 2015, "Preparation and characterization of sol-gel-derived n-ZnO thin film for Schottky diode application," Applied Physics A-Materials Science and Processing, 119(2), pp. 547-552.

[127] Yoshida, T., Komatsu, D., Shimokawa, N., and Minoura, H., 2004, "Mechanism of cathodic electrodeposition of zinc oxide thin films from aqueous zinc nitrate baths," Thin Solid Films, 451, pp. 166-169.

[128] Moulder, J. F., Stickle, W. F., Sobol, P. E., and Bomben, K. D., 1995, "Handbook of X-ray Photoelectron Spectroscopy," Physical Electronics, Eden Prairie, MN.

[129] Ballerini, G., Ogle, K., and Barthes-Labrousse, M. G.-. 2007, "The acid-base properties of the surface of native zinc oxide layers: An XPS study of adsorption of 1,2-diaminoethane," Applied Surface Science, 253(16), pp. 6860–6867.

[130] Keil, P., Frahm, R., and Luetzenkirchen-Hecht, D., 2010, "Native oxidation of sputter deposited polycrystalline copper thin films during short and long exposure times: Comparative investigation by specular and non-specular grazing incidence X-ray absorption spectroscopy," Corrosion Science, 52(4), pp. 1305–1316.

[131] Vasudev, P. K., Mattes, B. L., Pietras, E., and Bube, R. H., 1976, "Excess capacitance and non-ideal Schottky barriers on GaAs," Solid-State Electronics, 19(7), pp. 557-559.

[132] Yang, D., Kim, D., Ko, S. H., Pisano, A. P., Li, Z., and Park, I., 2015, "Focused Energy Field Method for the Localized Synthesis and Direct Integration of 1D Nanomaterials on Microelectronic Devices," Advanced Materials, 27(7), pp. 1207-1215.

[133] Ko, S. H., Lee, D., Kang, H. W., Nam, K. H., Yeo, J. Y., Hong, S. J., Grigoropoulos, C. P., and Sung, H. J., 2011, "Nanoforest of Hydrothermally Grown Hierarchical ZnO Nanowires for a High Efficiency Dye-Sensitized Solar Cell," Nano Letters, 11(2), pp. 666-671.

[134] Pan, H., Misra, N., Ko, S. H., Grigoropoulos, C. P., Miller, N., Haller, E. E., and Dubon, O., 2009, "Melt-mediated coalescence of solution-deposited ZnO nanoparticles by excimer laser annealing for thin-film transistor fabrication," Applied Physics A-Materials Science and Processing, 94(1), pp. 111-115.

[135] Park, S., Wang, G., Cho, B., Kim, Y., Song, S., Ji, Y., Yoon, M.-H., and Lee, T., 2012, "Flexible molecular-scale electronic devices," Nature Nanotechnology, 7(7), pp. 438-442.

[136] Wang, F., Seo, J.-H., Luo, G., Starr, M. B., Li, Z., Geng, D., Yin, X., Wang, S., Fraser, D. G., Morgan, D., Ma, Z., and Wang, X., 2016, "Nanometre-thick single-crystalline nanosheets grown at the water-air interface," Nature Communications, 7.

[137] Wang, F., Seo, J.-H., Ma, Z., and Wang, X., 2012, "Substrate-Free Self-Assembly Approach toward Large-Area Nanomembranes," ACS Nano, 6(3), pp. 2602-2609.

[138] Marotti, R. E., Guerra, D. N., Bello, C., Machado, G., and Dalchiele, E. A., 2004, "Bandgap energy tuning of electrochemically grown ZnO thin films by thickness and electrodeposition potential," Solar Energy Materials and Solar Cells, 82(1-2), pp. 85-103.

[139] Paunovic, M., and Schlesinger, M., 2006, Fundamentals of Electrochemical Deposition, John Wiley & Sons.

[140] Park, S.-I., Ahn, J.-H., Feng, X., Wang, S., Huang, Y., and Rogers, J. A., 2008, "Theoretical and Experimental Studies of Bending of Inorganic Electronic Materials on Plastic Substrates," Advanced Functional Materials, 18(18), pp. 2673-2684.

[141] Li, Z., Wang, Y., and Xiao, J., 2015, "Mechanics of curvilinear electronics and optoelectronics," Current Opinion in Solid State & Materials Science, 19(3), pp. 171-189.

[142] Ramirez, J. I., Li, Y. Y. V., Basantani, H., Leedy, K., Bayraktaroglu, B., Jessen, G. H., and Jackson, T. N., 2015, "Radiation-Hard ZnO Thin Film Transistors," IEEE Transactions on Nuclear Science, 62(3), pp. 1399-1404.

[143] Kim, M., Seo, J. H., Singisetti, U., and Ma, Z. Q., 2017, "Recent advances in free-standing single crystalline wide band-gap semiconductors and their applications: GaN, SiC, ZnO, beta-Ga2O3, and diamond," Journal of Materials Chemistry C, 5(33), pp. 8338-8354.

[144] Kim, J., Mastro, M. A., Tadjer, M. J., and Kim, J., 2018, "Heterostructure WSe2-Ga2O3 Junction Field-Effect Transistor for Low-Dimensional High-Power Electronics," ACS Applied Materials and Interfaces, 10(35), pp. 29724-29729.

[145] Kizilyalli, I. C., Xua, Y., Carlson, E., Manser, J., Cunningham, D. W., 2017, "Current and Future Directions in Power Electronic Devices and Circuits based on Wide Band-Gap Semiconductors," IEEE 5th Workshop on Wide Bandgap Power Devices and Applications (WiPDA).

[146] Eckardt, B., Wild, M., Joffe, C., Zeltner, S., Endres, S., and Maerz, M., 2018, "In Advanced Vehicle Charging Solutions Using SiC and GaN Power Devices," PCIM Europe 2018; International Exhibition and Conference for Power Electronics, Intelligent Motion, Renewable Energy and Energy Management, 5-7 June 2018, pp. 1-6.

[147] Lee, K. K., Luo, Y., Lu, X. F., Bao, P., and Song, A. M., 2011, "Development of Reactive-Ion Etching for ZnO-Based Nanodevices," IEEE Transactions on Nanotechnology, 10(4), pp. 839-843.

[148] Donigan, T., Langley, D., Schuette, M., Crespo, A., Walker, D., Tetlak, S., Leedy, K., Jessen, G., 2015, "Subtractive Plasma-Etch Process for Patterning High Performance ZnO TFTs," 73rd Annual Device Research Conference, Columbus, OH.

[149] Lorenz, M., Rao, M. S. R., Venkatesan, T., Fortunato, E., Barquinha, P., Branquinho, R., Salgueiro, D., Martins, R., Carlos, E., Liu, A., Shan, F. K., Grundmann, M., Boschker, H., Mukherjee, J., Priyadarshini, M., DasGupta, N., Rogers, D. J., Teherani, F. H., Sandana, E. V., Bove, P., Rietwyk, K., Zaban, A., Veziridis, A., Weidenkaff, A., Muralidhar, M., Murakami, M., Abel, S., Fompeyrine, J., Zuniga-Perez, J., Ramesh, R., Spaldin, N. A., Ostanin, S., Borisov, V., Mertig, I., Lazenka, V., Srinivasan, G., Prellier, W., Uchida, M., Kawasaki, M., Pentcheva, R., Gegenwart, P., Granozio, F. M., Fontcuberta, J., and Pryds, N., 2016, "The 2016 oxide electronic materials and oxide interfaces roadmap," Journal of Physics D-Applied Physics, 49(43).

[150] Baliga, B. J., 1989, "Power semiconductor-device figure of merit for high-frequency applications," IEEE Electron Device Letters, 10(10), pp. 455-457.

[151] Robin, Y., Moret, M., Ruffenach, S., Aulombard, R. L., and Briot, O., 2014, "Influence of the growth rate on the morphology of electrodeposited zinc oxide," Superlattices and Microstructures, 73, pp. 281-289.

[152] Mahalingam, T., John, V. S., Raja, M., Su, Y. K., and Sebastian, P. J., 2005, "Electrodeposition and characterization of transparent ZnO thin films," Solar Energy Materials and Solar Cells, 88(2), pp. 227-235.

[153] Gao, X.-D., Peng, F., Li, X.-M., Yu, W.-D., and Qiu, J.-J., 2007, "Growth of highly oriented ZnO films by the two-step electrodeposition technique," Journal of Materials Science, 42(23), pp. 9638-9644.

[154] Ghosh, T., and Basak, D., 2010, "Highly efficient ultraviolet photodetection in nanocolumnar RF sputtered ZnO films: a comparison between sputtered, sol-gel and aqueous chemically grown nanostructures," Nanotechnology, 21(37).

[155] Fortunato, E., Goncalves, A., Pimentel, A., Barquinha, P., Goncalves, G., Pereira, L., Ferreira, I., and Martins, R., 2009, "Zinc oxide, a multifunctional material: from material to device applications," Applied Physics A-Materials Science and Processing, 96(1), pp. 197-205.

[156] Singh, S., and Chakrabarti, P., 2013, "Comparison of the structural and optical properties of ZnO thin films deposited by three different methods for optoelectronic applications," Superlattices and Microstructures, 64, pp. 283-293.

[157] Hsueh, K. P., Chang, Y. S., Li, B. H., Wang, H. C., Chiu, H. C., Hu, C. W., and Xuan, R., 2019, "Effect of the AlGaN/GaN Schottky barrier diodes combined with a dual anode metal and a p-GaN layer on reverse breakdown and turn-on voltage," Materials Science in Semiconductor Processing, 90, pp. 107-111.

[158] Lorenz, M., Lajn, A., Frenzel, H., Wenckstern, H. V., Grundmann, M., Barquinha, P., Martins, R., and Fortunato, E., 2010, "Low-temperature processed Schottky-gated field-effect transistors based on amorphous gallium-indium-zinc-oxide thin films," Applied Physics Letters, 97(24).

[159] Ma, A. M., Gupta, M., Chowdhury, F. R., Shen, M., Bothe, K., Shankar, K., Tsui, Y., and Barlage, D. W., 2012, "Zinc oxide thin film transistors with Schottky source barriers," Solid-State Electronics, 76, pp. 104-108.

[160] Shinagawa, T., Chigane, M., Murase, K., and Izaki, M., 2012, "Drastic Change in Electrical Properties of Electrodeposited ZnO: Systematic Study by Hall Effect Measurements," Journal of Physical Chemistry C, 116(30), pp. 15925-15931.

[161] Moghadas, H., Daneshmand, M., and Mousavi, P., 2011, "A Dual-Band High-Gain Resonant Cavity Antenna With Orthogonal Polarizations," IEEE Antennas and Wireless Propagation Letters, 10, pp. 1220-1223.

[162] Moghadas, H., Daneshmand, M., and Mousavi, P., 2013, "Single-layer partially reflective surface for an orthogonally-polarised dual-band high-gain resonant cavity antenna," IET Microwaves Antennas and Propagation, 7(8), pp. 656-662.

[163] Verma, A., and Dube, D. C., 2005, "Measurement of dielectric parameters of small samples at X-band frequencies by cavity perturbation technique," IEEE Transactions on Instrumentation and Measurement, 54(5), pp. 2120-2123.

[164] Meriakri, V. V., Chigrai, E. E., Nikitin, I. P., and Parkhomenko, M. P., 2007, "Dielectric properties of water solutions with small content of glucose in the millimeter-wave band and the determination of glucose in blood," 2007 International Kharkov Symposium Physics and Engrg. of Millimeter and Sub-Millimeter Waves (MSMW), Kharkov, Ukraine.

[165] Baker-Jarvis, J., Geyer, R. G., Grosvenor, J. H., Janezic, M. D., Jones, C. A., Riddle, B., Weil, C. M., and Krupka, J., 1998, "Dielectric characterization of low-loss materials - A comparison of techniques," IEEE Transactions on Dielectrics and Electrical Insulation, 5(4), pp. 571-577.

[166] Milovanovic, B., Ivkovic, S., Tasic, V., 1998, "A simple method for permittivity measuring using microwave resonant cavity," 12th International Conference on Microwaves and Radar (MIKON 98), Krakow, Poland, vols 1-4, pp. 705-709.

[167] Boybay, M. S., and Ramahi, O. M., 2012, "Material Characterization Using Complementary Split-Ring Resonators," IEEE Transactions on Instrumentation and Measurement, 61(11), pp. 3039-3046.

[168] Zarifi, M. H., Shariaty, P., Abdolrazzaghi, M., Hashisho, Z., and Daneshmand, M., 2016, "Particle size characterization using a high resolution planar resonator sensor in a lossy medium," Sensors and Actuators B-Chemical, 234, pp. 332-337.

[169] Alahnomi, R. A., Zakaria, Z., Ruslan, E., and Bahar, A. A. M., 2016, "A Novel Symmetrical Split Ring Resonator Based on Microstrip for Microwave Sensors," Measurement Science Review, 16(1), pp. 21-27.

[170] Zarifi, M. H., Farsinezhad, S., Abdolrazzaghi, M., Daneshmand, M., and Shankar, K., 2016, "Selective microwave sensors exploiting the interaction of analytes with trap states in TiO2 nanotube arrays," Nanoscale, 8, pp. 7466-7473.

[171] Zarifi, M. H., Rahimi, M., Daneshmand, M., and Thundat, T., 2016, "Microwave ring resonator-based non-contact interface sensor for oil sands applications," Sensors and Actuators B-Chemical, 224, pp. 632-639.

[172] Zarifi, M. H., Sohrabi, A., Shaibani, P. M., Daneshmand, M., and Thundat, T., 2015, "Detection of Volatile Organic Compounds Using Microwave Sensors," IEEE Sensors Journal, 15(1), pp. 248-254.

[173] Khalifeh, R., Lescop, B., Gallee, F., and Rioual, S., 2016, "Development of a radio frequency resonator for monitoring water diffusion in organic coatings," Sensors and Actuators A-Physical, 247, pp. 30-36.

[174] Bailly, G., Harrabi, A., Rossignol, J., Stuerga, D., and Pribetich, P., 2016, "Microwave gas sensing with a microstrip interDigital capacitor: Detection of NH3 with TiO2 nanoparticles," Sensors and Actuators B-Chemical, 236, pp. 554-564.

[175] Mason, A., Korostynska, O., Ortoneda-Pedrola, M., Shaw, A., and Al-Shamma'a, A., 2013, "A resonant co-planar sensor at microwave frequencies for biomedical applications," Sensors and Actuators A-Physical, 202, pp. 170-175.

[176] Korostynska, O., Mason, A., and Al-Shamma'a, A., 2014, "Microwave sensors for the non-invasive monitoring of industrial and medical applications," Sensor Review, 34(2), pp. 182-191.

[177] Fok, M., Bashir, M., Fraser, H., Strouther, N., and Mason, A., 2015, "A Novel Microwave Sensor to Detect Specific Biomarkers in Human Cerebrospinal Fluid and Their Relationship to Cellular Ischemia During Thoracoabdominal Aortic Aneurysm Repair," Journal of Medical Systems, 39(4).

[178] Zarifi, M. H., Mohammadpour, A., Farsinezhad, S., Wiltshire, B. D., Nosrati, M., Askar, A. M., Daneshmand, M., and Shankar, K., 2015, "Time-Resolved Microwave Photoconductivity (TRMC) Using Planar Microwave Resonators: Application to the Study of Long-Lived Charge Pairs in Photoexcited Titania Nanotube Arrays," The Journal of Physical Chemistry C, 119(25), pp. 14358-14365.

[179] Zarifi, M. H., Farsinezhad, S., Wiltshire, B. D., Abdorrazaghi, M., Mahdi, N., Kar, P., Daneshmand, M., and Shankar, K., 2016, "Effect of phosphonate monolayer adsorbate on the microwave photoresponse of TiO2 nanotube membranes mounted on a planar double ring resonator," Nanotechnology, 27(37).

[180] Kunst, M., and Beck, G., 1986, "The study of charge carrier kinetics in semiconductors by microwave conductivity measurements," Journal of Applied Physics, 60(10), pp. 3558-3566.

[181] Park, J., Reid, O. G., Blackburn, J. L., and Rumbles, G., 2015, "Photoinduced spontaneous free-carrier generation in semiconducting single-walled carbon nanotubes," Nature Communications, 6.

[182] Kunst, M., Abdallah, O., and Wunsch, F., 2002, "Passivation of silicon by silicon nitride films," Solar Energy Materials and Solar Cells, 72(1-4), pp. 335-341.

[183] Liu, K. W., Ma, J. G., Zhang, J. Y., Lu, Y. M., Jiang, D. Y., Li, B. H., Zhao, D. X., Zhang, Z. Z., Yao, B., and Shen, D. Z., 2007, "Ultraviolet photoconductive detector with high visible rejection and fast photoresponse based on ZnO thin film," Solid-State Electronics, 51(5), pp. 757-761.

[184] Zhu, Q., Xie, C., Li, H., and Zeng, D., 2016, "A method for modeling and deciphering the persistent photoconductance and long-term charge storage of ZnO nanorod arrays," Nano Research, pp. 1-31.

[185] Benlamri, M., Farsinezhad, S., Barlage, D. W., and Shankar, K., 2016, "Low residual donor concentration and enhanced charge transport in low-cost electrodeposited ZnO," Journal of Materials Chemistry C, 4(12), pp. 2279-2283.

[186] Benlamri, M., Wiltshire, B. D., Zhang, Y., Mahdi, N., Shankar, K., and Barlage, D. W., 2019, "High breakdown strength Schottky diodes made from electrodeposited ZnO for power electronics applications," ACS Applied Electronic Materials, 1(1), pp. 13-17.

[187] Gurwitz, R., Cohen, R., and Shalish, I., 2014, "Interaction of light with the ZnO surface: Photon induced oxygen “breathing,” oxygen vacancies, persistent photoconductivity, and persistent photovoltage," Journal of Applied Physics, 115(3), p. 033701.

[188] Jeon, S., Ahn, S.-E., Song, I., Kim, C. J., Chung, U. I., Lee, E., Yoo, I., Nathan, A., Lee, S., Ghaffarzadeh, K., Robertson, J., and Kim, K., 2012, "Gated three-terminal device architecture to eliminate persistent photoconductivity in oxide semiconductor photosensor arrays," Nat Mater, 11(4), pp. 301-305.

[189] Ivanoff Reyes, P., Ku, C.-J., Duan, Z., Xu, Y., Garfunkel, E., and Lu, Y., 2012, "Reduction of persistent photoconductivity in ZnO thin film transistor-based UV photodetector," Applied Physics Letters, 101(3), p. 031118.

[190] Ashkenov, N., Mbenkum, B. N., Bundesmann, C., Riede, V., Lorenz, M., Spemann, D., Kaidashev, E. M., Kasic, A., Schubert, M., Grundmann, M., Wagner, G., Neumann, H., Darakchieva, V., Arwin, H., and Monemar, B., 2003, "Infrared dielectric functions and phonon modes of high-quality ZnO films," Journal of Applied Physics, 93(1), pp. 126-133.

[191] Kannan, P. K., Saraswathi, R., and Rayappan, J. B. B., 2010, "A highly sensitive humidity sensor based on DC reactive magnetron sputtered zinc oxide thin film," Sensors and Actuators A-Physical, 164(1-2), pp. 8-14.

[192] Li, Y. B., Della Valle, F., Simonnet, M., Yamada, I., and Delaunay, J. J., 2009, "Competitive surface effects of oxygen and water on UV photoresponse of ZnO nanowires," Applied Physics Letters, 94(2).

[193] Liu, S., Liu, S., Zhou, Y., Piao, Y., Li, G., and Wang, Q., 2018, "Transparent ZnO:Al2O3 films with high breakdown voltage and resistivity," Applied Physics Letters, 113(3).